LATVIAN JOURNAL of PHYSICS and TECHNICAL SCIENCES

ISSN 0868 - 8257

3

(Vol. 62)

2025

CONTENTS

K. Krizmane, M. Dile, E. Einbergs, V. Vitola,
A. Knoks, B. Hamawandi, A. Zolotarjovs
Optimising Photothermal Silver Nanoparticles for Efficient Light-Activated Shape Memory Response in AgNP-Polymer Composites 3

J. V. Sanchaniya, A. K. Prasad, T. Soni, I. Lasenko
Development and Characterisation of Biaxial PAN Nanofiber Mats 14

J. Kallunki
Investigation of Radiative Interference in Variable-Frequency Drives (VFD) 22

D. Kostrichkin, S. Rudenko, M. Lapkis, A. Atvars
Redesign of the AD820 Single-Channel Circuit for the Development of the aRD820 Low-Noise Rail-To-Rail Operational Amplifier 31

A. Mutule, I. Antoskova, P. Caroll, D. Biswas
Shared Understanding of Local Energy Community Terminology: A Catalyst for Interdisciplinary Collaboration and Stakeholder Engagement 47

M. Auders, I. Geipele, S. Lapuke
Multi-Apartment Building Electricity Consumers in the Framework of Energy Communities 58

F. I. Abbas, M. Sugiyama
ZnO-Thin Film Growth Processes: Correlation Between the Structural Properties of Hydrochloric Acid (HCl) and Water (H_2O) Solution Effect using Innovative Electrostatic Spray Deposition (ESD) Technology 68

S. Ali, B. Djaouida
Investigating the Feasibility of Integrating Vegetation into Solar Chimney Power Plants in the Tamanrasset Region 77

LATVIAN JOURNAL of PHYSICS and TECHNICAL SCIENCES

LATVIJAS FIZIKAS un TEHNISKO ZINĀTŅU ŽURNĀLS

Published six times a year since February 1964
Iznāk sešas reizes gadā kopš 1964. gada februāra

3 (Vol. 62) • 2025

RĪGA

Language Editor: O. Ivanova
Computer Designer: I. Begicevs

INDEXED (PUBLISHED) IN

www.scopus.com
www.sciendo.com
EBSCO (Academic Search Complete, www.epnet.com), INSPEC (www.iee.org.com).
VINITI (www.viniti.ru), Begell House Inc/ (EDC, www.edata-center.com).

Issuers: Institute of Physical Energetics,
Institute of Solid State Physics, University of Latvia
Registration Certificate Number: 000700221

Editorial Contacts:
14 Dzerbenes Street, Riga, LV-1006
LATVIA
tel: +371 26245896
M: +371 29363105
leo@lza.lv

sciendo

LATVIAN JOURNAL OF PHYSICS
AND TECHNICAL SCIENCES
2025, N 3

DOI: 10.2478/lpts-2025-0017

OPTIMISING PHOTOTHERMAL SILVER NANOPARTICLES FOR EFFICIENT LIGHT-ACTIVATED SHAPE MEMORY RESPONSE IN AgNP-POLYMER COMPOSITES

K. Krizmane, M. Dile, E. Einbergs, V. Vitola*, A. Knoks,
B. Hamawandi, A. Zolotarjovs

Institute of Solid State Physics, University of Latvia,
8 Ķengaraga Str., Riga, LV-1063, LATVIA
*e-mail: virginija.vitola@cfi.lu.lv

The study presents the synthesis and integration of silver nanoparticles (AgNPs) into a polyurethane (PU) matrix to create a light-activated shape memory polymer (SMP). AgNPs were synthesized using a microwave-assisted solvothermal method with polyvinylpyrrolidone (PVP) as a stabilizer, where varying the molecular weight of PVP and the $AgNO_3$/PVP ratio influenced nanoparticle size and distribution. Characterisation via scanning electron microscopy (SEM) and dynamic light scattering (DLS) confirmed the irregular morphology and size consistency of AgNPs, with smaller particles exhibiting narrow size distributions and enhanced photothermal response. Among the samples, PVP with an average molecular weight (M_n) of 10,000 and an $AgNO_3$/PVP mole ratio of 14.7 demonstrated optimal UV-blue light absorption, which facilitated efficient local heating under irradiation. The AgNP-PU composite exhibited a reliable shape memory effect when exposed to UV-blue light.

Keywords: *Microwave-assisted synthesis, photothermal effect, polymer composite, shape memory, silver nanoparticles.*

1. INTRODUCTION

In recent years, SMPs have increasingly become pivotal in the field of actuating applications, ranging from everyday products to biomedical [1]–[3] and aeronautical devices [4], [5]. An important turning point in the usability of these materials has been the possibility to 3D-print the desired final shape. Four-dimensional (4D) printing, an advanced evolution of 3D printing, has acquired substantial interest across various research domains, including smart materials and biomedical research. This technique enables a 3D printed structure to transform its shape over time in response to specific stimuli such as light, heat, electrical current, magnetic fields, or osmotic pressure [6]–[9]. SMPs are types of polymers that can maintain a temporary shape due to their network points and flexible chains. The shape memory effect in thermal SMPs is induced by subjecting the material to a thermal stimulus that triggers a transition between its temporary and initial shape states. When heated to a specific temperature, above the polymer's glass transition temperature (T_g), the polymer chains gain sufficient mobility, allowing the material to revert to its initial shape (Fig. *1*). This thermally activated process is governed by the polymer's molecular structure, which can be engineered to exhibit reversible phase transitions. Upon cooling below the glass transition temperature, the polymer retains the recovered shape, effectively "locking" in the morphology due to restricted chain mobility [10].

By optimising the thermal and mechanical properties of the polymer, it is possible to achieve controlled and repeatable shape memory behaviour suitable for applications in biomedical devices [1], [11], [12], actuators [13], [14], and smart materials [15], [16]. There are different thermal SMPs, i.e., PU, which is valued for its versatility, biocompatibility, and potential biodegradability when modified with eco-friendly components. PU's biocompatibility makes it particularly suitable for medical applications, including flexible foams and durable elastomers that come into direct contact with biological tissues [17]–[19]. Polylactic acid (PLA), recognized for its robust mechanical strength, biodegradability, biocompatibility, and non-toxicity, has been increasingly used in biomedical applications in recent years [20], [21]. Poly-ε-caprolactone (PCL), an affordable semi-crystalline aliphatic polyester, is utilised in bone tissue engineering for its drug delivery and wound healing properties [22]–[24].

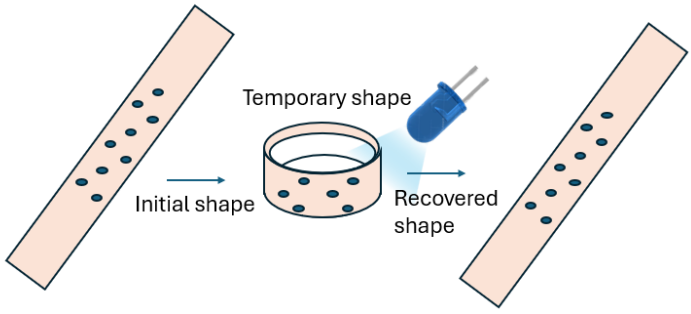

Fig. 1. A schematic drawing of shape memory composite in action.

Beyond traditional thermal activation, the shape memory effect in thermal SMPs can be achieved through the photothermal effect, where embedded photothermal nanoparticles enable light-activated heating (Fig. *1*). Specifically, by incorporating photothermal particles such as AgNPs into the polymer matrix, shape recovery can be triggered via light exposure [25]. This process leverages the nanoparticles' capacity to absorb light, particularly in the UV or visible spectrum, converting it into localised heat through surface plasmon resonance (SPR) [26], [27]. The heat generated by these nanoparticles can raise the polymer's temperature above its glass transition or melting temperature, initiating the shape memory effect without direct bulk heating [28]. In this study, we synthesized AgNPs using PVP as a stabilizing agent, exploring the influence of PVP molecular weight and the $AgNO_3$/PVP ratio on nanoparticle properties. The length of the PVP polymer chains, which correlates with its molecular weight, plays a crucial role in nanoparticle stabilization and size, directly impacting light absorption efficiency. Our findings demonstrated that AgNPs synthesized with PVP (M_n = 10,000 g/mol) at an $AgNO_3$/PVP ratio of 14.7 exhibited the highest photothermal activity, achieving optimal UV-blue light absorption and efficient heat transfer to the PU matrix. This method allows for precise, spatially resolved activation of the shape memory effect via light, presenting promising applications in remote-controlled actuation suitable for biomedical applications.

2. EXPERIMENTAL

2.1. Materials

Silver nitrate ($AgNO_3$, purity ≥ 99 %, Lach-Ner) was used as an Ag precursor. Polyvinylpyrrolidone (PVP) with three different molecular weights (M_n= 10,000, 29,000 and 90,000 g/mol, Sigma-Aldrich) was used as surface stabilizer for AgNPs. Ethylene glycol (EG, $C_2H_6O_2$, purity ≥ 99 %, Sigma Aldrich) was used as both a solvent and a reducing agent. Deionized water (DIW, ρ = 18.2 MΩ cm at 25 °C, total organic carbon up to 20 ppb, microorganisms < 10 CFU mL^{-1}, heavy metals < 0.01 ppm, silicates < 0.01 ppm, and total dissolved solids < 0.03 ppm) and acetone (purity ≥ 99.5%, Sigma-Aldrich) were used to precipitate the synthesized AgNPs, and ethanol (C_2H_5OH, purity 96%; Supelco) was used to redisperse the nanoparticles for later incorporation into the polymer matrix. To prepare the polymer matrix for AgNP embedding, PU-22 universal polyurethane polymer resin and HU-22 universal hardener (Uzlex, WMT Baltic) were utilised. All chemicals were of analytical grade and used as received, without further purification.

2.2. Synthesis of AgNPs

Ag nanoparticles stabilized by PVP were synthesized via a microwave-assisted polyol process, following the method developed by Lalegani et.al. [19]. To ensure efficient transfer of microwave radiation for rapid and uniform heating, each sample was prepared individually, with only one vial placed in the microwave synthesis system at a time.

First, a specified amount of PVP poly-

mer was dissolved in EG under constant stirring. For higher molecular weight PVP, heating was applied to promote dissolution. After cooling the solution to room temperature, a measured quantity of $AgNO_3$ was dissolved, and the mixture was transferred to a 70 mL PTFE container in a microwave synthesis system. The specific quantities of reagents used in this synthesis are listed in Table 1.

AgNP synthesis was performed in a Milestone synthWAVE microwave reactor. The system operates at 2.45 GHz frequency with variable power from 0 to 100 % (1.5 kW). The reaction was carried out at 160 °C for 10 min under constant stirring speed (60 % of maximum stirring speed) in an inert atmosphere (N_2 gas) and 40 bar preload pressure. The target temperature was reached within 2.5 minutes. After microwave processing, the reaction mixture was naturally cooled down to room temperature, and transparent colloidal solutions with colours ranging from yellow to brownish red was obtained. As the reducing ability of ethylene glycol (EG) becomes negligible at room temperature, effectively slowing down nanoparticle growth, the synthesized AgNPs were stored in EG for further characterisation. For subsequent dispersion of AgNPs in ethanol for embedding in polymer matrix, the samples were alternately washed several times with DIW and acetone.

Table 1. Amount of Reagents Used in AgNP Synthesis with the Ratio and Obtained Sample Colour

Sample name	M_n of PVP (g/mol)	PVP (g)	$AgNO_3$ (g)	EG (mL)	Mole ratio $AgNO_3$/PVP	Sample colour
Ag_1	10,000	0.10	0.1	40	58.8	brownish red
Ag_2	10,000	0.40	0.1	40	14.7	red
Ag_29	29,000	0.29	0.1	40	58.8	brownish yellow
Ag_90	90,000	0.90	0.1	40	58.8	yellow

2.3. Fabrication of Polymer/Nanoparticle Composite

AgNP sample labelled Ag_2 was used to fabricate the PU/AgNP composite. 0.9 mL of 0.03 M AgNP solution in ethanol was added to a mixture of 1 g PU-22 and 1 g HU-22. The mixture was stirred with a magnetic stirrer for 5 min to ensure even distribution of nanoparticles throughout the polymer. The polymer mixture was then cast onto a polystyrene plate and left to dry at room temperature for 2 days. AgNP/PU composite containing 0.15 % AgNP was obtained. We tested the glass transition temperature of the employed polymer, and it was found to be 38 °C.

2.4. Methods of Characterisation

The morphology of the Ag NPs samples was characterised by scanning electron microscopy (SEM) (Tescan Lyra, Brno-Kohoutovice, Czech Republic), operated at 12 kV. A drop of the AgNP solution in ethylene glycol was placed onto a silicon wafer and air-dried before SEM analysis. Additional measurements were performed

on the AgNPs in ethylene glycol solution. Particle size distribution was characterised by dynamic light scattering (DLS) using Litesizer 500 (Anton Paar). Optical density was measured with Cary 7000 Universal Measurement Spectrophotometer (Agilent, USA). The nanoparticle samples, at a concentration of 0.015 M, were diluted in EG in a 1:1 ratio. OD measurements were conducted using a quartz cuvette (spectral range 200–2,500 nm, pathlength 10 mm). Temperature changes under UV-blue light exposure were recorded using a Unisense x-5 UniAmp with TP-200 glass thermocouple, coupled with 420 nm LED.

3. RESULTS AND DISCUSSION

The M_n of PVP polymer is directly connected to its chain length, where higher molecular weight compounds have longer polymer chains. In the synthesis process of silver nanoparticles, PVP is used to coat and stabilise nanoparticles. The chain length of PVP affects the radius of the resulting nanoparticles and can lead to variations in absorption. In this research, we experimented with different molecular weight PVP polymers to determine how the length of the attached polymer chain influenced the absorption of UV-blue light by silver nanoparticles. Additionally, the PVP to $AgNO_3$ ratio was varied to obtain the best conditions for synthesis (Table 1). Our goal was to achieve effective UV-blue light absorption due to the SPR of silver nanoparticles.

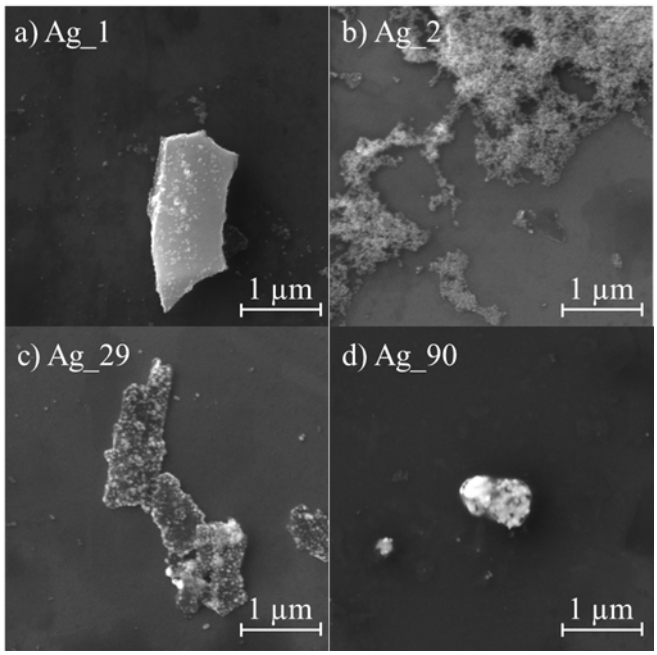

Fig. 2. SEM images of AgNP prepared with PVP; a) and b) M_n = 10,000 g/mol, c) M_n = 29,000 g/mol, d) M_n = 90,000 g/mol.

The morphology of the prepared samples was determined using SEM analysis. Fig. 2. shows the formation of irregular Ag NP with sizes ranging between 20 nm and 60 nm. In samples labelled Ag_1, Ag_29, Ag_90, particles are capped with a surrounding layer. This layer most likely consists of organic compounds, more specifically, PVP polymer chains. SEM images show agglomerates in samples where higher M_n PVP was used (M_n = 29,000, 90,000 g/mol), suggesting these particles may also agglomerate in EG solution. In contrast, Ag_1 and Ag_2, prepared with lower M_n PVP (10,000 g/mol), show less agglomeration in SEM images, particularly for sample Ag_2, where $AgNO_3$/PVP ratio was 14.7. This observation implies that the particles are likely well dispersed in EG solution without forming agglomerates.

Table 2. DLS Measurements of AgNPs Showing Hydrodynamic Diameter and Size Distribution (PDI)

Sample name	Hydrodynamic diameter, nm	PDI, %
Ag_1	44	26
Ag_2	41	0.18
Ag_29	394	22
Ag_90	1246	29

DLS measurements (Table 2) confirm these observations. For Ag_90, the measured hydrodynamic diameter is 1246 nm, likely representing organic-coated agglomerates rather than individual Ag NPs. Similarly, Ag_29 has a hydrodynamic diameter of 394 nm. In contrast, Ag_1 and Ag_2 show similar nanoparticle sizes (44 and 41 nm, respectively) but differ in polydispersity index (PDI), with Ag_2 exhibiting a narrower size distribution (PDI = 0.18 %). SEM images support this, showing less agglomeration in Ag_2 and suggesting that PVP provides better stabilization of nanoparticles in this sample.

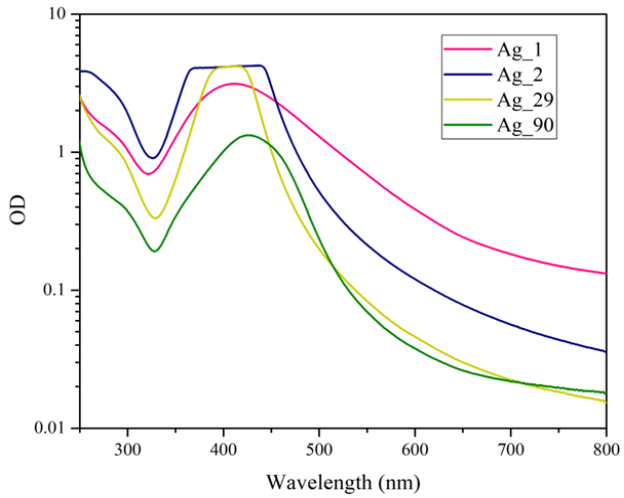

Fig. 3. The optical density (OD) of AgNP solution (1:1) in ethylene glycol.

The OD of the AgNP suspension in EG was measured using a spectrophotometer (Fig. 3.), employing EG in the reference beam to account for its baseline absorption. The Ag_2 sample (M_n PVP = 10,000 g/mol, $AgNO_3$ to PVP mole ratio 14.7) exhibited the highest absorption in the UV and blue spectral range, with a prominent peak around 400–450 nm, which was characteristic due to their SPR. Typically, AgNPs with sizes around 10–50 nm display a strong absorption band in this region, as the collective oscillation of conduction electrons on their surface resonates with incident light, particularly in the visible and near-UV ranges. This SPR peak intensity and position are influenced by nanoparticle size, shape, and the refractive index of surrounding media. The observed high OD in the Ag_2 sample suggests efficient UV-blue light absorption, which is ideal for photothermal applications requiring localised heating and enhanced responsiveness in SMPs.

Following the optical density measurements, we assessed the photothermal heating effect of the AgNP solution in EG by coupling a temperature sensor with a blue light-emitting diode. The resulting temperature changes are depicted in Fig. 4.

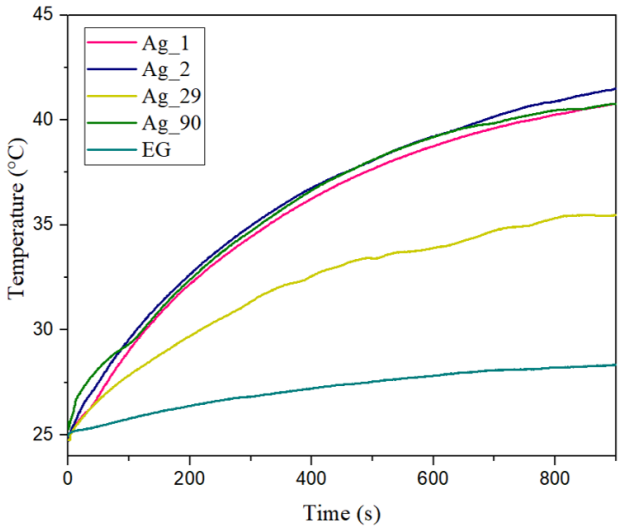

Fig. 4. Temperature change for different AgNP samples under blue light exposure.

This setup allowed us to monitor the temperature changes induced by light absorption directly within the AgNP solution. The temperature profiles of different AgNP samples in EG demonstrated a similar trend: upon blue light exposure, the temperature initially increased, with each sample exhibiting a distinct heating rate. However, after a certain period, the temperature reached a plateau, indicating that the heating rate due to light absorption balanced with the cooling rate to the surrounding environment. This equilibrium point reflects the thermal stability achievable with each sample under continuous illumination, determined by factors such as nanoparticle concentration, size, and light absorption efficiency. The variations in heating rates before reaching the plateau also highlight differences in the photothermal conversion efficiency of each sample. The Ag_2 and Ag_90 samples exhibited the fastest heat-

ing rate and the largest plateau temperature, which is also above the transition temperature for the PU polymer – that means these two NP samples could be used for the light-activated shape memory polymer.

The nanoparticle sample Ag_2, which showed the best heating efficiency, was embedded in the polymer for the PU-nanoparticle composite, and the shape memory effect was tested and compared to a polymer without nanoparticles. Both samples were cut into equal size: thin, straight strips. They were submerged in 38 °C hot water and formed in the temporary shape – a ring, and after that, the samples were rapidly cooled in cold water to fix the temporary shape. Both samples showed a stable temporary shape. After that, an LED (40 mW, 420 nm, Thorlabs) was placed 5 cm from the samples, and the shape recovery was observed. The polymer without nanoparticles did not recover its original shape. It remained in ring form, but the PU-AgNP composite unrolled to the original shape, thus demonstrating the shape memory effect (Fig. 5.).

Fig. 5. Unfolding of the shape-memory PU/AgNP composite under 420 nm light stimulus; rolled polymer (t = 0s), unrolled polymer (t = 50s).

4. CONCLUSIONS

Silver nanoparticles stabilised by polyvinylpyrrolidone were successfully synthesized using a microwave-assisted solvothermal method. The molecular weight and concentration of PVP played a critical role in determining the size and distribution of the nanoparticles, with different $AgNO_3$/PVP ratios resulting in varied nanoparticle characteristics. Dynamic light scattering and scanning electron microscopy analyses confirmed the size and morphology of the AgNPs. SEM images revealed PVP coated irregularly shaped silver nanoparticles, while DLS measurements indicated that samples synthesised with lower molecular weight PVP had a narrower size distribution, suggesting that the molecular weight of PVP affects synthesized nanoparticle distribution.

Notably, the smallest size distribution was observed in the Ag_2 sample, where the $AgNO_3$/PVP ratio was 14.7, differing from other samples. This indicated that the PVP concentration significantly influences particle agglomeration, which is critical for achieving efficient light absorption and photothermal conversion. Among the synthesized samples, Ag_2 sample exhibited optimal photothermal activity. This sample demonstrated high UV-blue light absorp-

tion efficiency, which is attributed to its surface plasmon resonance. This enhanced photothermal effect is crucial for light-activated shape-memory applications. When integrated into a polyurethane matrix, Ag_2 nanoparticles enabled the composite to respond to UV-blue light, thus triggering the shape memory effect. It was tested that while a PU sample without nanoparticles did not revert to its original shape, the PU-AgNP composite demonstrated successful shape recovery under UV-blue light, proving the effectiveness of AgNPs in inducing light-activated shape memory effect. This study supports that the potential of AgNP-integrated shape memory polymers for applications in remote-controlled actuation is advantageous. Future research should focus on optimising the concentration of AgNPs within the polymer to improve heating efficiency and further enhance the material's shape-memory capabilities.

ACKNOWLEDGEMENTS

Virginija Vitola acknowledges the project LZP-2023/1-0521. The authors acknowledge the Institute of Solid State Physics of the University of Latvia, which, as a center of excellence, has received funding from the European Union framework program Horizon 2020 H2020-WIDESPREAD-01-2026-2017-TeamingPhase2 within grant agreement No. 739508 of the CAMART2 project.

REFERENCES

1. Delaey, J., Dubruel, P., & Van Vlierberghe, S. (2020). Shape-Memory Polymers for Biomedical Applications. *Adv Funct Mater., 30*, 1909047. https://doi.org/10.1002/ADFM.201909047
2. Vidakis, N., Petousis, M., Velidakis, E., Liebscher, M., & Tzounis, L. (2020). Three-Dimensional Printed Antimicrobial Objects of Polylactic Acid (PLA)-Silver Nanoparticle Nanocomposite Filaments Produced by an In-Situ Reduction Reactive Melt Mixing Process. *Biomimetics*, *5*, 42. https://doi.org/10.3390/BIOMIMETICS5030042
3. Holman, H., Kavarana, M.N., & Rajab, T.K.v (2021). Smart Materials in Cardiovascular Implants: Shape Memory Alloys and Shape Memory Polymers. *Artif. Organs, 45,* 454–463. https://doi.org/10.1111/AOR.13851
4. Luo, L., Zhang, F., Wang, L., Liu, Y., & Leng, J. (2024). Recent Advances in Shape Memory Polymers: Multifunctional Materials, Multiscale Structures, and Applications. *Adv Funct Mater., 34*, 2312036. https://doi.org/10.1002/ADFM.202312036
5. Iorio, L., Quadrini, F., Santo, L., Circi, C., Cavallini, E., & Carmine Pellegrini, R. (2024). Shape Memory Polymer Composite Hinges for Solar Sails. *Advances in Space Research, 74*, 3201–3215. https://doi.org/10.1016/J.ASR.2024.07.010
6. Wang, X., He, Y., Liu, Y., & Leng, J. (2022). Advances in Shape Memory Polymers: Remote Actuation, Multi-Stimuli Control, 4D Printing and Prospective Applications. *Materials Science and Engineering: R: Reports, 151*, 100702. https://doi.org/10.1016/J.MSER.2022.100702.
7. Hassan, H., Hallez, H., Thielemans, W., & Vandeginste, V. (2024). A Review of Electro-Active Shape Memory Polymer Composites: Materials Engineering Strategies for Shape Memory Enhancement. *Eur Polym J., 208*, 112861. https://doi.org/10.1016/J.EURPOLYMJ.2024.112861

8. Yun, G., Tang, S.Y., Sun, S., Yuan, D., Zhao, Q., Deng, L., … & Li, W. (2019). Liquid Metal-Filled Magnetorheological Elastomer with Positive Piezoconductivity. *Nature Communications, 10* (1), 1–9. https://doi.org/10.1038/s41467-019-09325-4
9. Vitola, V., Bite, I., Apsite, I., Zolotarjovs, A., & Biswas, A. (2021). CuS/polyurethane Composite Appropriate for 4D Printing. *Journal of Polymer Research, 28*, 1–6. https://doi.org/10.1007/S10965-020-02375-Z/TABLES/1
10. Xia, Y., He, Y., Zhang, F., Liu, Y., & Leng, J. (2021). A Review of Shape Memory Polymers and Composites: Mechanisms, Materials, and Applications. *Advanced Materials, 33*, 2000713. https://doi.org/10.1002/ADMA.202000713
11. Wang, L., Zhang, F., Liu, Y., & Leng, J. (2021). Shape Memory Polymer Fibers: Materials, Structures, and Applications. *Advanced Fiber Materials, 4* (1), 5–23. https://doi.org/10.1007/S42765-021-00073-Z
12. Ma, S., Jiang, Z., Wang, M., Zhang, L., Liang, Y., Zhang, Z., Ren L, & Ren L. (2021). 4D printing of PLA/PCL Shape Memory Composites with Controllable Sequential Deformation. *Biodes Manuf., 4*, 867–878. https://doi.org/10.1007/S42242-021-00151-6/FIGURES/12
13. Margoy, D., Gouzman, I., Grossman, E., Bolker, A., Eliaz, N., & Verker, R. (2021). Epoxy-Based Shape Memory Composite for Space Applications. *Acta Astronaut, 178*, 908–919. https://doi.org/10.1016/J.ACTAASTRO.2020.08.026
14. Kong, D., Li, J., Guo, A., & Xiao, X. (2021). High Temperature Electromagnetic Shielding Shape Memory Polymer Composite. *Chemical Engineering Journal, 408,* 127365. https://doi.org/10.1016/J.CEJ.2020.127365
15. Pilate, F., Toncheva, A., Dubois, P., & Raquez, J. M. (2016). Shape-Memory Polymers for Multiple Applications in the Materials World. *Eur Polym J., 80*, 268–294. https://doi.org/10.1016/J.EURPOLYMJ.2016.05.004
16. Rahmatabadi, D., Aberoumand, M., Soltanmohammadi, K., Soleyman, E., Ghasemi, I., Baniassadi, M., … & Baghani, M. (2022). A New Strategy for Achieving Shape Memory Effects in 4D Printed Two-Layer Composite Structures. *Polymers, 14*, 5446. https://doi.org/10.3390/POLYM14245446
17. Zhao, T., Yu, R., Li, X., Cheng, B., Zhang, Y., Yang, X., … & Huang, W. (2018). 4D Printing of Shape Memory Polyurethane via Stereolithography. *Eur Polym J., 101*, 120–126. https://doi.org/10.1016/J.EURPOLYMJ.2018.02.021
18. Ramezani, M., & Monroe, M.B.B. (2022). Biostable Segmented Thermoplastic Polyurethane Shape Memory Polymers for Smart Biomedical Applications. *ACS Appl Polym Mater., 4*, 1956–1965. https://doi.org/10.1021/ACSAPM.1C01808/ASSET/IMAGES/LARGE/AP1C01808_0010.JPEG
19. Biswas, A., Apsite, I., Rosenfeldt, S., Bite, I., Vitola, V., & Ionov, L. (2024). Modular Photoorigami-Based 4D Manufacturing of Vascular Junction Elements. *J Mater Chem. B, 12*, 5405–5417. https://doi.org/10.1039/D4TB00236A
20. Jia, H., Gu, S.Y., & Chang, K. (2018). 3D Printed Self-Expandable Vascular Stents from Biodegradable Shape Memory Polymer. *Advances in Polymer Technology, 37,* 3222–3228. https://doi.org/10.1002/ADV.22091
21. Wang, L., Ma, J., Guo, T., Zhang, F., Dong, A., Zhang, S., … & Leng, J. (2023). Control of Surface Wrinkles on Shape Memory PLA/PPDO Micro-nanofibers and Their Applications in Drug Release and Anti-scarring. *Advanced Fiber Materials, 5*, 632–649. https://doi.org/10.1007/S42765-022-00249-1/FIGURES/7
22. Molina, B.G., Ocón, G., Silva, F.M., Iribarren, J. I., Armelin, E., & Alemán C. (2023). Thermally-Induced Shape Memory Behavior of Polylactic Acid/Polycaprolactone Blends. *Eur Polym J., 196*, 112230. https://doi.org/10.1016/J.EURPOLYMJ.2023.112230

23. Yang, C.S., Wu, H.C., Sun, J.S., Hsiao, H.M., & Wang, T.W. (2013). Thermo-Induced Shape-Memory PEG-PCL Copolymer as a Dual-Drug-Eluting Biodegradable Stent. *ACS Appl Mater Interfaces, 5,* 10985–10994. https://doi.org/10.1021/AM4032295/SUPPL_FILE/AM4032295_SI_001.PDF
24. Lv, H., Tang, D., Sun, Z., Gao, J., Yang, X., Jia, S., & Peng, J. (2020). Electrospun PCL-Based Polyurethane/HA Microfibers as Drug Carrier of Dexamethasone with Enhanced Biodegradability and Shape Memory Performances. *Colloid Polym Sci., 298*, 103–111. https://doi.org/10.1007/S00396-019-04568-5/FIGURES/11
25. Herath, M., Epaarachchi, J., Islam, M., Fang, L., & Leng, J. (2020). Light Activated Shape Memory Polymers and Composites: A Review. *Eur Polym J., 136,* 109912. https://doi.org/10.1016/J.EURPOLYMJ.2020.109912
26. Khurana, K., & Jaggi, N. (2021). Localized Surface Plasmonic Properties of Au and Ag Nanoparticles for Sensors: A Review. *Plasmonics, 16* (4), 981–99. https://doi.org/10.1007/S11468-021-01381-1
27. Cui, X., Ruan, Q., Zhuo, X., Xia, X., Hu, J., Fu, R., … & Xu, H. (2023). Photothermal Nanomaterials: A Powerful Light-to-Heat Converter. *Chem Rev., 123,* 6891–952. https://doi.org/10.1021/ACS.CHEMREV.3C00159/ASSET/IMAGES/LARGE/CR3C00159_0029.JPEG
28. Stoychev, G., Kirillova, A., & Ionov, L. (2019). Light-Responsive Shape-Changing Polymers. *Adv Opt Mater., 7*, 1900067. https://doi.org/10.1002/ADOM.201900067

sciendo

LATVIAN JOURNAL OF PHYSICS
AND TECHNICAL SCIENCES
2025, N 3

DOI: 10.2478/lpts-2025-0018

DEVELOPMENT AND CHARACTERISATION OF BIAXIAL PAN NANOFIBER MATS

J. V. Sanchaniya*, A. K. Prasad, T. Soni, I. Lasenko

Riga Technical University,
Faculty of Civil and Mechanical Engineering,
Institute of Mechanics and Mechanical Engineering,
6B Kipsala Str., Riga, LV-1048, LATVIA
*e-mail: jaymin.sanchaniya@rtu.lv

This study addresses the challenge of enhancing the strength of polyacrylonitrile (PAN) nanofiber mats in the transverse direction, which is a critical aspect for filtration applications targeting micro-sized viruses and bacteria. Traditional methods of producing orientated nanofibers often result in mats with limited transverse strength. To overcome this, our research focused on developing biaxial nanofibers, which exhibit enhanced interbonding in both axial and transverse directions. Using a single-syringe electrospinning setup with a rotating drum collector, we successfully fabricated biaxially orientated PAN nanofiber mats. Scanning electron microscopy (SEM) analysis was employed to visualise and confirm the biaxial arrangement and porous structure of the mats. Mechanical testing further demonstrated that these biaxially arranged nanofibers possessed comparable strength in both orientations, signifying a significant advancement in the structural integrity of PAN nanofiber mats for filtration applications.

Keywords*: Aligned nanofibers, biaxial nanofibers, polyacrylonitrile (PAN), porosity.*

1. INTRODUCTION

Electrospinning emerges as a cost-effective technique for the manufacture of polymer fibres, characterised by diameters ranging from ten to several hundred nanometres [1]. This method has engendered a wide array of applications, notably in the realms of optical materials [2], sensor fabrication [3], nanocomposites [4]–[7], tissue engineering scaffolds [8], wound care, drug delivery systems [9], filtration technologies [10], protective clothing [11], and antibacterial textiles [5], [12], [13].

Polyacrylonitrile (PAN) nanofibers, produced through electrospinning, are fre-

quently employed as precursors for continuous carbon nanofibers via processes such as stabilisation and carbonisation. Additionally, these fibres are extensively used in filtration and catalysis. PAN nanofibers are particularly effective in various filtering scenarios, encompassing air and water purification, biofluid processing, and the extraction of toxic substances and deleterious contaminants from contaminated aqueous environments [14]. Because of their expansive surface area and electrostatic properties, PAN nanofibers are proficient at trapping airborne particles, such as dust and microbes, in air filtration systems. Similarly, in water filtration applications, they efficiently eliminate pollutants, including toxic agents, chemical compounds, and bacteria [15].

The biocompatibility and environmental safety of PAN nanofibers render them particularly suitable for medical and biological applications. For example, they can be used as filtering materials on dialysis machines, in wound dressings [16], or as scaffolds for tissue engineering [17]. PAN nanofibers have numerous advantages over traditional filtration media, establishing their utility in a wide spectrum of filtering applications [18].

However, a notable challenge with conventionally aligned nanofiber mats lies in their limited strength in the transverse direction. These mats predominantly bear loads along the direction of the nanofibers, resulting in increased susceptibility to particle penetration. This limitation significantly undermines their effectiveness in filtration applications [19].

To address this issue, we introduce a novel method for producing biaxially arranged nanofiber mats at a laboratory scale. The approach involves the preparation of orientated nanofiber mats which are subsequently sectioned into smaller pieces. These segments then undergo a secondary electrospinning process to create an additional aligned layer, culminating in a biaxial arrangement. The fabricated nanofiber mats were subjected to a rigorous evaluation, including mechanical testing, analysis of fibre orientation, and scanning electron microscopy (SEM) analysis. This comprehensive investigation aims to determine the efficacy of the biaxial nanofiber configuration in enhancing the mechanical properties and, as a consequence, for the subsequent enhancement of the filtration efficiency of PAN nanofiber mats.

2. MATERIALS AND METHODOLOGY

In the fabrication of biaxial nanofibers, polyacrylonitrile (PAN) with an average molecular weight of 150,000 (typical) and a CAS number of 25014-41-9 was used. The solvent used for this process was N, N-Dimethylformamide (DMF), which has an average molecular weight of 73.10 g/mol, designated as ACS Reagent (solvent) with a purity of >=99.8 %, and a CAS number of 68-12-2. This solvent was obtained from Sigma Aldrich Chemicals, Germany.

The electrospinning process was carried out as previously described by the authors [19]–[21], with a notable modification. Following the production of a 40 cm x 5 cm nanofiber mat, it was segmented into 5 cm x 5 cm squares. These sections were then rotated 90 degrees and reattached to the rotating drum to facilitate the formation of a secondary layer of nanofibers, thus achieving a biaxial configuration. The entire procedure of biaxial nanofiber fabrication is illustrated in Fig. 1.

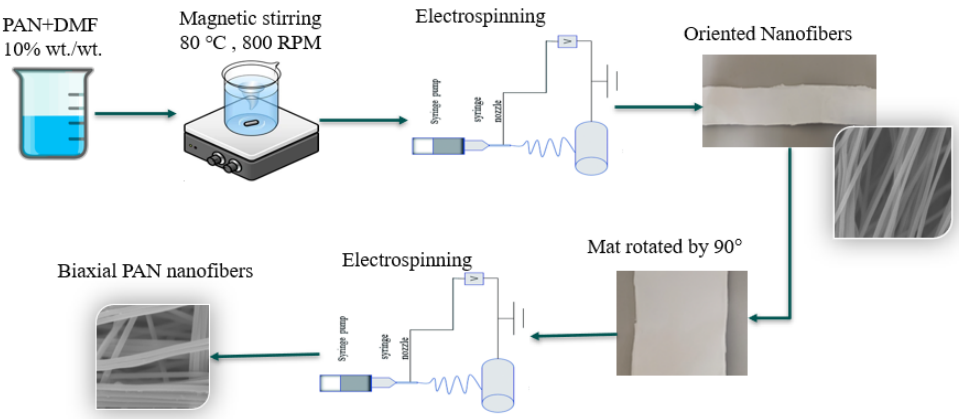

Fig. 1. Fabrication process of orientated and biaxial nanofibers.

For the acquisition of scanning electron microscopy (SEM) images, a Hitachi TM300 tabletop SEM was used. This instrument was set to a magnification of 1500, a vacuum of 10^{-2} Torr, and an ion coating current of 6 mA. The nanofibers were coated with a layer of gold (Au) with a thickness of 150 Å to enhance image quality. The orientation and porosity of the fibres were analysed using the OrientationJ plug-in for ImageJ software (ImageJ, National Institutes of Health, Bethesda, MD, USA). Contrast enhancement was applied to the SEM images to facilitate clearer observation. The mean diameter and standard deviation of the nanofibers were determined by measuring the diameter of 100 randomly selected nanofibers from three different SEM images.

Tensile properties were measured using a Mecmesin Multi-Test 2.5-i tensile testing machine equipped with a 25-N sensor (PPT Group UK Ltd., t/a Mecmesin, Newton House, Spring Copse Business Park, Slinfold, UK). Samples were conditioned at room temperature according to ISO 139:1973, "Standard Environments for Conditioning and Testing". This standard specifies a temperature of 21 ± 1 °C, a relative air humidity of 60 %, and an atmospheric pressure of 760 mm Hg. The dimensions of the test samples were 50 mm × 10 mm (length × width), according to ASTM D882-18. A total of five measurements were made to ascertain the tensile properties of the nanofiber mats. The thickness of these mats was measured using a digital micrometre (range: 0–25 mm; Digimatic micrometre, MDC-25PX, code No. 293-240-30, serial No. 71912410, Mitutoyo, Japan) [19].

2. RESULTS AND DISCUSSION

Scanning electron microscopy (SEM) images presented in Figs. 2a and 2b depict the microstructure of polyacrylonitrile (PAN) nanofibers, both in their orientated and biaxial configurations. These images unequivocally demonstrate that by rotating the initial nanofiber mat and subsequently performing a secondary electrospinning process, it is feasible to fabricate biaxial nanofibers.

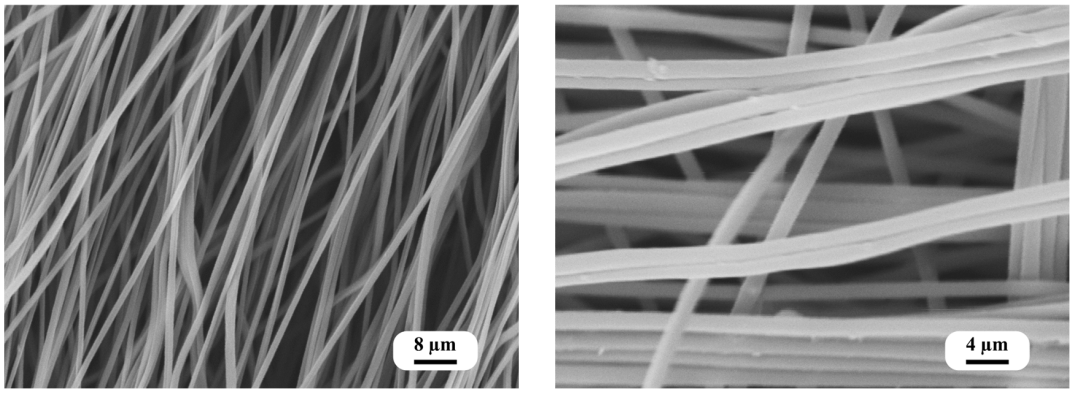

Fig. 2. SEM images of (a) oriented and (b) biaxial PAN nanofibers.

Figure 3 illustrates the diameter distribution of the nanofibers. Analysis of the SEM images of uniaxial and biaxial nanofiber samples revealed that the average diameter of the nanofibers was 512 nm, with a standard deviation in a normal distribution of ± 95 nm. In certain instances, the nanofibers exhibited a minimum diameter of 325.045 nm and a maximum diameter of 805.713 nm.

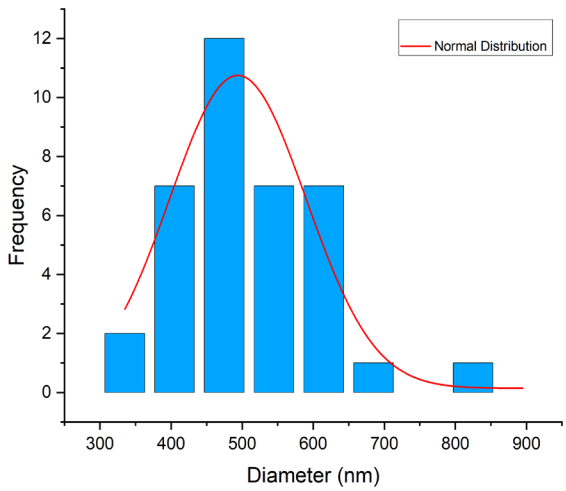

Fig. 3. Distribution of the diameter of nanofibers.

Porosity, indicative of the spaces within the nanofiber structure, is quantified as the ratio of the volume of voids to the total volume of the sample, typically expressed as a percentage. Porosity analysis revealed that uniaxial nanofibers exhibited a higher porosity of 52.7 %, in contrast to the 38.3 % observed in biaxial nanofibers. This difference is attributable to the single-axis orientation of the uniaxial fibres, leading to larger voids, while the biaxial fibres, aligned along the X and Y axes, exhibit reduced porosity.

Figures 4a and 4b present the orientation of nanofibers in uniaxial and biaxial arrangements. The orientation analysis indicated that the uniaxial fibres predomi-

nantly displayed angles within a maximum variation of 10 degrees, while the biaxial fibres exhibited orientation within a range of -1 to +1 degrees, perpendicular to the orientated fibres.

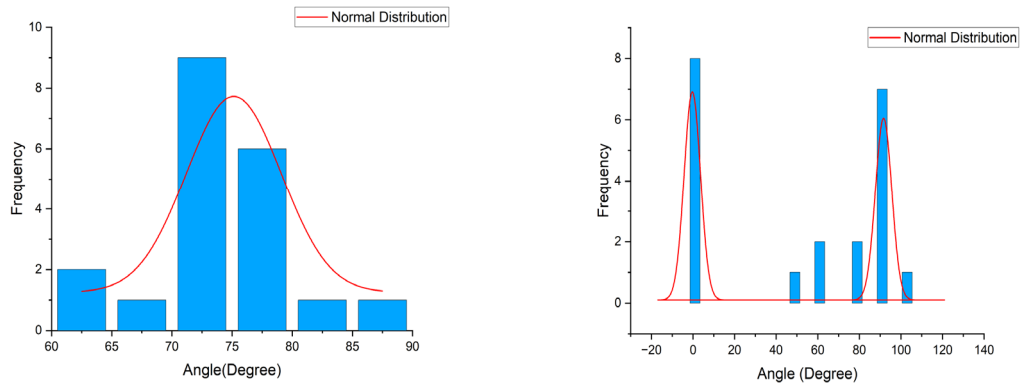

Fig. 4. Orientation of (a) aligned fibres and (b) biaxially arranged fibres.

Figure 5 shows the representative stress-strain curves for oriented and biaxially arranged nanofibers. The elastic modulus of the uniaxially oriented nanofibers was determined to be 524 ± 15 MPa, while for the biaxial nanofiber mats, it was 343 ± 12 MPa. The elongation at break was recorded at 12 ± 1 % for oriented fibres and 8 ± 1 % for biaxial fibres. The maximum tensile strength for uniaxial and biaxial fibres was found to be 11 ± 1 MPa and 8 ± 1 MPa, respectively. The summary of the mechanical properties of orientated and biaxial nanofibers is shown in Table 1.

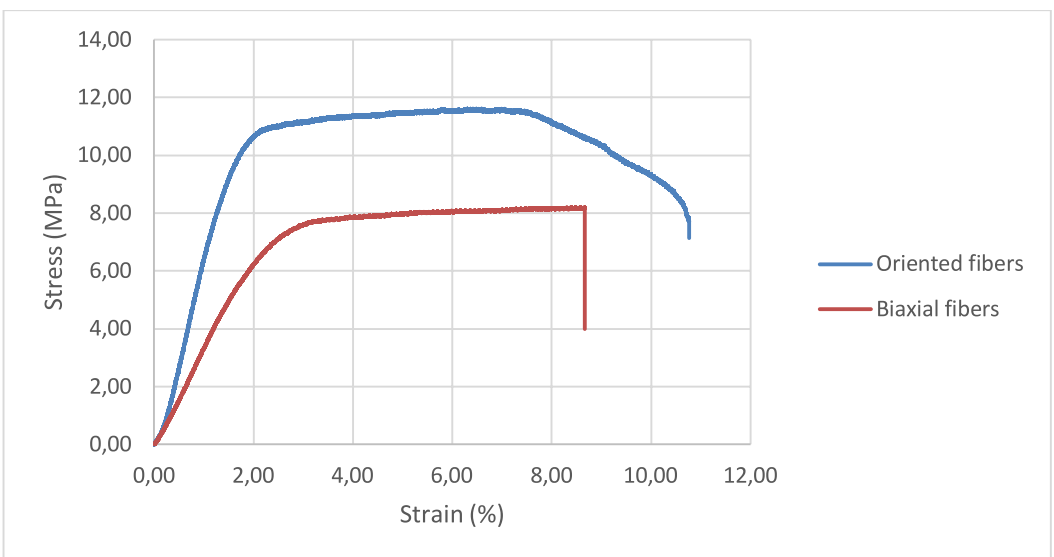

Fig. 5. Representative stress-strain curve of orientated and biaxial nanofibers.

Table 1. Summary of the Mechanical Properties of Orientated and Biaxial Nanofibers

	Thickness (μm)	Elastic modulus (MPa)	Ultimate tensile strength (MPa)	Elongation at break (%)
Nanofiber mat with oriented nanofibers	112±8	524±15	12±1	11±1
Nanofiber mat with biaxial nanofibers	225±10	343±12	8±1	8**±1**

Theoretically, the mechanical properties of biaxially arranged nanofibers would be approximately half of those observed in uniaxially aligned fibres. However, the findings of this study indicate a slight deviation from this expectation, with the properties being marginally above half. This discrepancy could be attributed to the phase in which the nanofibers are collected during electrospinning. The SEM analysis confirms that the fibres are not collected in a liquid phase. The observed mechanical properties suggest that some fibres are collected in a semi-solid state, leading to their fusion with the pre-existing-oriented nanofibers. This interaction could potentially contribute to the enhanced mechanical properties observed in biaxially arranged nanofiber mats.

3. CONCLUSIONS

This study has successfully demonstrated the feasibility of fabricating biaxially arranged polyacrylonitrile (PAN) nanofiber mats using an innovative electrospinning technique. This method involved the rotation and subsequent layering of electrospun nanofiber mats, resulting in a biaxial fibre arrangement. The comprehensive analysis conducted through scanning electron microscopy (SEM), mechanical testing, and porosity evaluation has yielded insightful findings relevant to the structural and functional attributes of these nanofiber mats.

SEM analysis provided a clear visual representation of the nanofibers in both their uniaxial and biaxial orientations. This image was pivotal in confirming the successful creation of biaxial nanofibers and their distinct morphology. The measured diameters of the nanofibers indicated reasonable uniformity with a moderate range of variance, thereby ensuring consistent fibre quality.

Porosity analysis revealed that the biaxial nanofibers exhibited a lower porosity percentage compared to their uniaxial counterparts. This result can be attributed to the dual-axis alignment in biaxial fibres, which effectively reduces void spaces, making them denser and potentially more suitable for applications requiring finer filtration capabilities.

The mechanical properties of the nanofiber mats, as assessed through tensile testing, indicated that the biaxially arranged nanofibers possess a mechanical strength slightly higher than theoretically predicted. Although the uniaxial nanofibers showed higher values in terms of elastic modulus, elongation at break, and ultimate tensile strength, the biaxial fibres demonstrated respectable performance, considering their structural complexity. This unexpected enhancement in mechanical properties can be partly attributed to the phase in which the nanofibers were collected during electrospinning, with some fibres potentially

being in a semi-solid state, leading to fusion with the preexisting-orientated nanofibers.

In conclusion, the development and characterisation of biaxial PAN nanofiber mats has opened new avenues in the field of nanofiber technology. The unique structure of these biaxially arranged nanofibers holds significant promise for a variety of applications, particularly in filtration and other fields where enhanced mechanical strength and reduced porosity are desirable. Future studies may focus on optimising the fabrication process to further improve the mechanical properties and functional performance of these biaxial nanofiber mats, potentially expanding their applicability in both industrial and medical domains.

ACKNOWLEDGEMENTS

This research/publication has been supported by the Doctoral Grant programme of Riga Technical University.

REFERENCES

1. Wang, Z., Sahadevan, R., Crandall, C., Menkhaus, T. J., & Fong, H. (2020). Hot-Pressed PAN/PVDF Hybrid Electrospun Nanofiber Membranes for Ultrafiltration. *J. Memb. Sci.*, *611*, 118327. DOI: 10.1016/j.memsci.2020.118327
2. Ding, B., Wang, M., Wang, X., Yu, J., & Sun, G. (2010). Electrospun Nanomaterials for Ultrasensitive Sensors. *Mater. Today*, *13* (11) 16–27. DOI: 10.1016/S1369-7021(10)70200-5
3. Jin, H., Nayeem, Md O. G., Lee, S., Matsuhima, N., Inuoe, D., Yokota, T., … & Someya, T. (2019). Highly Durable Nanofiber-Reinforced Elastic Conductors for Skin-tight electronic Textiles. *ACS Nano*, *13* (7), 7905–7912. DOI: 10.1021/acsnano.9b02297
4. Lasenko, I., Sanchaniya, J. V., Kanakuntla, S. P., Ladani, Y., Viluma-Gudona, A., Kononova, O., … & Selga, T. (2023). The Mechanical Properties of Nanocomposites Reinforced with PA6 Electrospun Nanofibers. *Polymers (Basel).*, *15* (3). DOI: 10.3390/polym15030673
5. Sanchaniya, J.-V., Kanukuntla, S.-P., Modappathi, P., & Macanovskis, A. (2022). Mechanical Behaviour Numerical Investigation of Composite Structure, Consisting of Polymeric Nanocomposite Mat and Textile. *21st Int. Sci. Conf. Eng. Rural Dev. Proc.*, *21*, 720–726. DOI: 10.22616/erdev.2022.21.tf225
6. Kanukuntla, S. P., Sanchaniya, J. V., & Kardani, U. (2023). Numerical Simulation of Polymeric Composite Nanofiber Mat. *Engineering for Rural Development,* 790–795.
7. Sanchaniya, J. V., Lasenko, I., Vijayan, V., Smogor, H., Gobins, V., Kobeissi, A., & Goljandin, D. (2024). A Novel Method to Enhance the Mechanical Properties of Polyacrylonitrile Nanofiber Mats: An Experimental and Numerical Investigation. *Polymers (Basel)*, *16* (7), 992. DOI: 10.3390/polym16070992
8. Wang, X., Ding, B., & Li, B. (2013). Biomimetic Electrospun nanofibrous structures for Tissue Engineering. *Mater. Today*, *16* (6), 229–241. DOI: 10.1016/j.mattod.2013.06.005
9. Duan, X., lan Chen, H., & Guo, C. (2022). Polymeric Nanofibers for Drug Delivery Applications: A Recent Review. *J. Mater. Sci. Mater. Med.*, *33* (12). DOI: 10.1007/s10856-022-06700-4
10. Zhou, Y., Liu, Y., Zhang, M., Feng, Z., Yu, D. G., & Wang, K. (2022). Electrospun

Nanofiber Membranes for Air Filtration: A Review. *Nanomaterials*, *12* (7). DOI: 10.3390/nano12071077

11. Gorji, M., Bagherzadeh, R., & Fashandi, H. (2017). Electrospun nanofibers in protective clothing. *Woodhead Publishing Series in Textiles, Electrospun Nanofibers*, 571–598. DOI: 10.1016/B978-0-08-100907-9.00021-0
12. Lasenko, I., Grauda, D., Butkauskas, D., Sanchaniya, J. V., Viluma-Gudmona, A., & Lusis, V. (2022). Testing the Physical and Mechanical Properties of Polyacrylonitrile Nanofibers Reinforced with Succinite and Silicon Dioxide Nanoparticles. *Textiles*, *2* (1), 62–173. DOI: 10.3390/textiles2010009
13. Grauda, D., Butkauskas, D., Vyðniauskienë, R., Ranèelienë, D., Krasņevska, A., Miķelsone, A., … & Ļašenko, I. (2023). Establishment of Biotesting System to Study Features of Innovative Multifunctional Biotextile. *Proc. Latv. Acad. Sci. Sect. B Nat. Exact, Appl. Sci.*, *77* (3–4), 186–192. DOI: 10.2478/prolas-2023-0026
14. Myndrul, V., Coy, E., Bechelany, M., & Iatsunskyi, I. (2021). Photoluminescence Label-Free Immunosensor for the Detection of Aflatoxin B1 Using Polyacrylonitrile/ Zinc Oxide Nanofibers. *Mater. Sci. Eng. C*, *118*, 111401. DOI: 10.1016/j. msec.2020.111401
15. Anusiya, G., & Jaiganesh, R. (2022). A Review on Fabrication Methods of Nanofibers and a Special Focus on Application of Cellulose Nanofibers. *Carbohydr. Polym. Technol. Appl.*, *4*, 100262. DOI: 10.1016/j.carpta.2022.100262
16. Chen, K., Hu, H., Zeng, Y., Pan, H., Wang, S., Zhang, Y., … & Liu, H. (2022). Recent Advances in Electrospun Nanofibers for Wound Dressing. *Eur. Polym. J.*, *178*, 111490. DOI: 10.1016/j. eurpolymj.2022.111490
17. Liao, Y., Loh, C. H., Tian, M., Wang, R., & Fane, A. G. (2018). Progress in Electrospun Polymeric Nanofibrous Membranes for Water Treatment: Fabrication, Modification and Applications. *Prog. Polym. Sci.*, *77*, 69–94. DOI: 10.1016/j. progpolymsci.2017.10.003
18. Sridhara, P. K., Masso, F., Olsén, P., & Vilaseca, F. (2021). Strong Polyamide-6 Nanocomposites with Cellulose Nanofibers Mediated by Green Solvent Mixtures. *Nanomaterials*, *11* (8), 1–17. DOI: 10.3390/ nano11082127
19. Sanchaniya, J. V., Lasenko, I., Kanukuntala, S. P., Smogor, H., Viluma-Gudmona, A., Krasnikovs, A., … & Gobins, V. (2023). Mechanical and Thermal Characteristics of Annealed-Oriented PAN Nanofibers. *Polymers (Basel)*, *15* (15), 3287. DOI: 10.3390/polym15153287
20. Sanchaniya, J. V., Lasenko, I., Kanukuntla, S. P., Mannodi, A., Viluma-Gudmona, A., & Gobins, V. (2023). Preparation and Characterization of Non-Crimping Laminated Textile Composites Reinforced with Electrospun Nanofibers. *Nanomaterials*, *13* (13), 1949. DOI: 10.3390/nano13131949
21. Sanchaniya, J. V., Lasenko, I., Gobins, V., & Kobeissi, A. (2024). A Finite Element Method for Determining the Mechanical Properties of Electrospun Nanofibrous Mats. *Polym.*, *16* (6), 852. DOI: 10.3390/ polym16060852

sciendo

LATVIAN JOURNAL OF PHYSICS
AND TECHNICAL SCIENCES
2025, N 3

DOI: 10.2478/lpts-2025-0019

INVESTIGATION OF RADIATIVE INTERFERENCE IN VARIABLE-FREQUENCY DRIVES (VFD)

J. Kallunki

Metropolia University of Applied Sciences,
Leiritie 1, Vantaa, 01600, FINLAND
E-mail: juha.kallunki@metropolia.fi

Alternating current (AC) motor applications are commonly controlled using variable-frequency drives (VFDs), which provide benefits such as enhanced system controllability and improved energy efficiency. Despite these advantages, VFDs are associated with challenges, particularly the generation of electromagnetic interference (EMI). This study examines the radiative EMI characteristics of VFDs and evaluates straightforward technical solutions, with a primary emphasis on shielding techniques, to mitigate their impact. For a low-power VFD, a test system was specifically designed for this investigation. The analysis revealed that the most significant broadband EMI emissions originated from the motor cable and the VFD unit itself. By implementing appropriate shielding strategies, we substantially reduced the EMI signal strength, with some cases demonstrating complete suppression. Furthermore, this experimental setup will serve as a practical component in laboratory exercises for undergraduate students, offering hands-on experience with EMI analysis and mitigation methodologies.

Keywords: *Education, electromagnetic compatibility, electromagnetic interference, variable-frequency drive.*

1. INTRODUCTION

The adoption of frequency-controlled motors, commonly referred to as variable-frequency drives (VFDs), has grown significantly over recent decades. The benefits of VFDs are well-documented, including enhanced process control and improved energy efficiency. Notably, energy efficiency has become increasingly critical in light of the ongoing green transition. Despite their advantages, VFDs present notable challenges, particularly as sources of electromagnetic interference (EMI), e.g., [1]–[8]. These EMI issues can lead to malfunctions in other electronic devices, additional energy losses, motor bearing failures, and broader disruptions in systems where signal integrity is essential.

The source of this interference can be traced to the control strategies employed in motor drives. Achieving precise control necessitates high switching frequencies, often reaching hundreds of kilohertz, facilitated by power semiconductor devices such as insulated gate bipolar transistors (IGBTs) or gate turn-off (GTO) thyristors. These high switching frequencies produce rapid voltage and current transitions, which in turn generate high-frequency voltage and current components. These unwanted high-frequency components are the primary contributors to many interference issues.

Electromagnetic interference (EMI) issues in VFD systems can be classified as either conductive or radiative emissions. Conductive EMI is transmitted along physical connections, such as wiring, whereas radiative EMI propagates through electric or magnetic fields. In VFD systems, both transmission mechanisms contribute to EMI propagation.

Mitigation strategies include the use of various filtering solutions [7], [9], [10] and the careful selection of appropriate materials. Additionally, strict adherence to the manufacturer's installation guidelines and related recommendations is essential to minimise EMI-related problems. Regulatory standards define permissible EMI emission levels for VFDs, with the IEC 61800-3 standard, *Adjustable Speed Electrical Power Drive Systems – Part 3: EMC Requirements and Specific Test Methods*, providing a comprehensive framework for ensuring compliance.

Effective shielding techniques are essential to mitigate radiative emissions. Specifically, the cable connecting the converter unit to the motor must be shielded. Shielded cables should be grounded, typically at least at one end; however, in certain applications, grounding at both ends is required. The choice of grounding configuration is highly context-dependent and must account for local conditions. In addition to shielding, common-mode filters are frequently employed to attenuate high-frequency voltages and currents. These filters are typically installed on both phase conductors and ground wires to further suppress EMI and enhance system performance.

Figure 1 provides an overview of a VFD system. According to the IEC 61800-5-1 standard, the drive system, excluding the motor and any sensors mechanically coupled to the motor shafts, is referred to as the Complete Drive Module (CDM). In this study, the term "VFD unit" is used synonymously with the Complete Drive Module (CDM), representing the entire physical VFD unit. CDMs are typically well-shielded and engineered to minimise EMI emissions, making them less significant as sources of interference. Instead, the motor cable is the primary determinant of the overall EMI performance of the VFD system. In contrast, the feed cable, which connects the power input to the drive unit, has a relatively minor influence on total EMI performance. While standard cables are generally sufficient for feed cable applications, shielded feed cables may be necessary in sensitive installations where strict EMI mitigation is required.

In Fig. 1, potential locations for detecting radiative EMI are highlighted with red flashes. The size of each flash represents the relative likelihood of encountering radiative EMI at that specific location. Interference currents and voltages are characterised by high-frequency signals, with their frequencies proportional to the switching frequency of the VFD. These interference signals can extend into the high-frequency range, reaching several hundred megahertz or even into the gigahertz spectrum. Like other power electronic devices, VFDs are typically non-linear loads, which generate

harmonic distortions in the input power network. These harmonic voltages can contribute to additional energy losses and may cause malfunctions in other connected devices. To mitigate harmonics, various filtering techniques can be employed, including passive filters, such as inductors and capacitors, and active filters, which dynamically compensate for harmonic distortions.

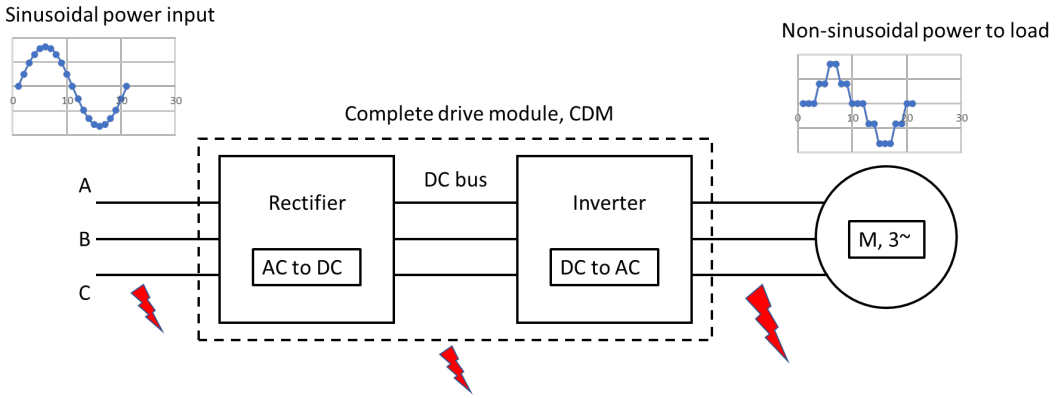

Fig. 1. The frequency-controlled motor drive comprises three main components: the rectifier, the direct current (DC) bus, and the inverter. Red flashes highlight potential sources of radiative EMI, with the size of each flash representing the relative likelihood of EMI occurrence. The motor cable, marked by the largest flash, is identified as the most significant source of radiative EMI. Additionally, the feed cable, connecting the input power network to the VFD unit (or Complete Drive Module, CDM), may also contribute to radiative EMI, albeit to a lesser extent.

Conductive EMI in VFDs has been studied more extensively than radiative EMI. However, the significance of addressing radiative EMI is increasing, particularly as industrial environments become more dependent on wireless communication systems, which are highly susceptible to various forms of interference. As a result, understanding the radiative emission characteristics of VFDs is becoming increasingly crucial. Given the widespread use of VFDs across diverse applications and environments, the potential for interference with other devices is rising. Radiative EMI emissions are often referred to as radio frequency interference (RFI), as these interfering signals typically operate at relatively high frequencies.

Section 2 describes the test setup and the radiative interference measurements conducted in this study. Section 3 presents the results of these measurements, along with key observations drawn from the data. Finally, Section 4 provides the conclusions, including recommendations for future research and potential areas for improvement.

2. MEASUREMENT SETUP AND EMI MEASUREMENTS

This study investigates the radiative interference emissions from a VFD system, with all measurements conducted in the radiative near-field. The objective is not to standardise electromagnetic compatibility (EMC) measurements but to identify

the locations of the strongest interference signals and assess whether their magnitudes are sufficient to disrupt other systems potentially. Additionally, we evaluate the effectiveness of traditional shielding methods in mitigating the interference levels. While absolute signal strength is not the primary focus of this study, the main goal is to pinpoint the origins of the EMI signals.

It is likely that VFDs operating at high power levels also generate radiative interference in the far-field; however, this aspect falls outside the scope of the present study. Standardised EMC measurements typically require specialised infrastructure, such as an anechoic chamber, which was unavailable for this work. Alternatively, using a semi-anechoic chamber could also be considered, as suggested in [11]. In the real-world environment where our measurements were conducted, it was crucial to minimise the influence of other devices on the results, particularly for far-field observations.

For the test environment, we selected a mini-scale VFD with a nominal operating power of 750 W. This VFD drives a small three-phase induction motor with a nominal power rating of 40 W. A small-scale VFD was chosen due to its ease of modification, which facilitates efficient adjustments during testing. Additionally, the system lacks any filters, allowing for accurate identification of the sources of harmful radio emissions. Figure 2 illustrates the VFD system used in the experiment.

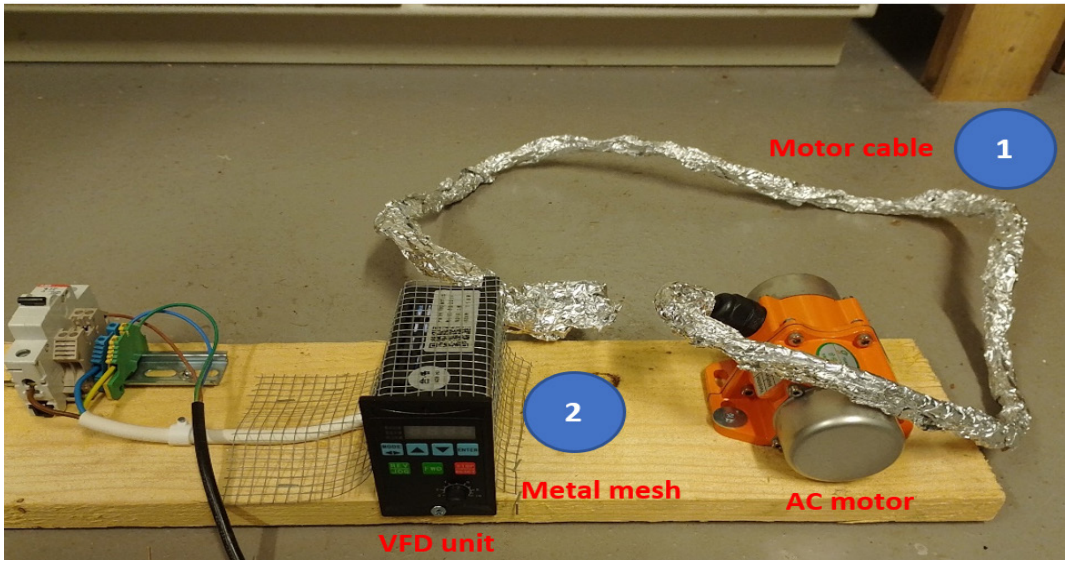

Fig. 2. VFD test setup. The numbers (1 and 2) indicate the measurement locations. Measurements were taken both with and without shielding. The motor cable was shielded using aluminium foil, while the VFD unit was shielded with a metallic mesh.

The measurements were performed using a handheld spectrum analyzer and a near-field probe antenna. The emission levels were sufficiently high that no additional low-noise amplifier was needed. The frequency range analysed in this study spans from 10 kHz to 200 MHz. The alternating current generates a magnetic field, which, when the wire is unshielded, can be detected in the near field using a loop antenna. The operating principle is illustrated in Figure 3.

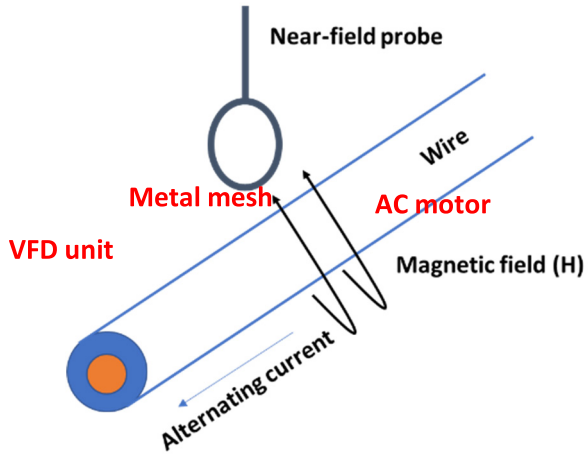

Fig. 3. The near-field probe should be positioned close to the conductor, allowing the magnetic field lines to pass through the loop antenna (near-field probe). The probe is then connected to the spectrum analyzer for measurement.

The distance of the near-field (d_f) can be calculated as follows:

$$d_f = \frac{\lambda}{2\pi},$$

where λ is the wavelength. In this study, the shortest near-field distance is approximately 24 cm at 200 MHz. The loop antenna was positioned about 1 cm from the measurement target, ensuring that all measurements were conducted within the near-field. In addition, the magnetic field (B) around a straight cable can be calculated as follows:

$$B = \frac{\mu_0 I}{2\pi r},$$

where μ_0 is permeability of free space ($\sim 4\pi \times 10^{-7}$ H/m); I is a current through the wire, and r is distance from the wire. It is evident that the magnetic field strength decreases as the distance from the wire increases. However, with our measurement setup, we observed that the magnetic field did not attenuate significantly. Shielding effectiveness (SE) refers to the ability of a material to attenuate radio frequency (RF) signals, indicating how effectively the material blocks or reduces electromagnetic interference. For metal mesh net shielding effectiveness (in near-field for the magnetic field) can be defined as follows:

$$SE(db) = 20 \times \log\left(\frac{\pi r}{g}\right),$$

where g is mesh's grid size. In our case, it is 6 mm. If we assume that the loop antenna is located around 1 cm away from the measurement target ($r = 0.01\ m$), the SE is about 14.4 dB.

The motor was tested under three different rotational speed conditions: 10 %, 50 %, and 100 % of the nominal speed. However, no significant differences in the interference levels were observed across these conditions. Figure 4 presents the spectrum measured from the motor cable when the system was powered off. This plot illustrates that the spectrum was free of interference sources, serving as the baseline (background noise level) for the subsequent measurements.

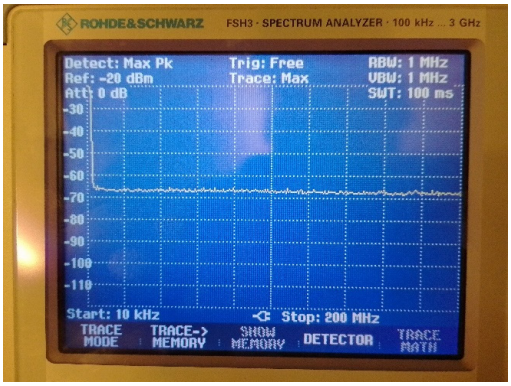

Fig. 4. The measured spectrum (10 kHz–200 MHz) from the motor cable, when the system was powered off, serves as the background level for the measurements. From this spectrum, it is also evident that the room where the tests were conducted was free from radiative interference sources.

Strong radiative emissions were detected from the motor cable (Fig. 5, left plot) and the VFD unit (Fig. 6, left plot). The interference originating from the VFD unit was the most prominent, with a maximum signal level of approximately -28 dBm. Other components of the system, such as the input cable, were also examined, but no significant interference was detected from these locations.

In both cases (motor cable and VFD unit), the interference signals were broadband, spanning the entire frequency range under study (10 kHz to 200 MHz). Additionally, the signal levels at their peak exceeded the reference level by more than 30 dB.

The original motor cable in the system was an unshielded polyvinyl chloride (PVC) cable. To mitigate the emissions, we wrapped the cable with aluminium foil (commercial-grade foil with a thickness of 0.03–0.04 mm). This shielding method proved highly effective, as no significant radiative interference was detected from the cable afterward (Fig. 5, right plot), with only minor peaks (~5 dB above the reference level) observed within the 10 kHz to 200 MHz frequency range. Therefore, we can conclude that the applied shielding significantly reduced the radiative interference from the motor cable.

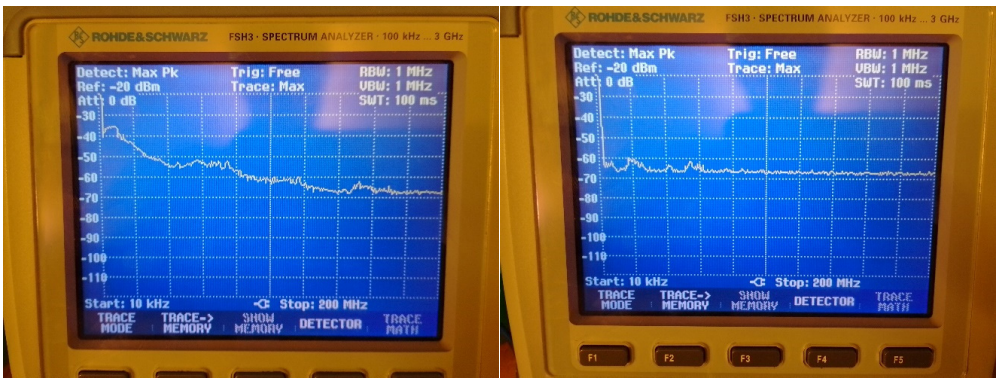

Fig. 5. The measured spectrum (10 kHz–200 MHz) from the motor cable is shown in the plots. The left plot displays the spectrum when the system was running, while the right plot shows the spectrum after the cable was shielded. The shielding effectively eliminated most of the wide-band interference, with only minor interference remaining between 10 kHz and 60 MHz.

The VFD unit is not fully shielded, primarily due to its cooling requirements. Both sides of the VFD feature ventilation holes, which are suboptimal from an EMC perspective. To address this issue, we shielded both sides of the VFD using a metallic mesh with a grid size of 6 mm × 6 mm. After applying this shielding, we repeated the measurements, and the results were promising (Fig. 6, right plot). The interference signal level was reduced by more than 10 dB, as anticipated based on our calculations, representing a significant improvement over the original condition. While using a foil similar to that applied to the motor cable would likely offer better shielding efficiency, it would also cause overheating due to obstruction of the natural ventilation. These findings underscore the importance of implementing proper EMC solutions in areas requiring ventilation. For example, fans equipped with EMC filters could be used to maintain adequate ventilation while minimising interference.

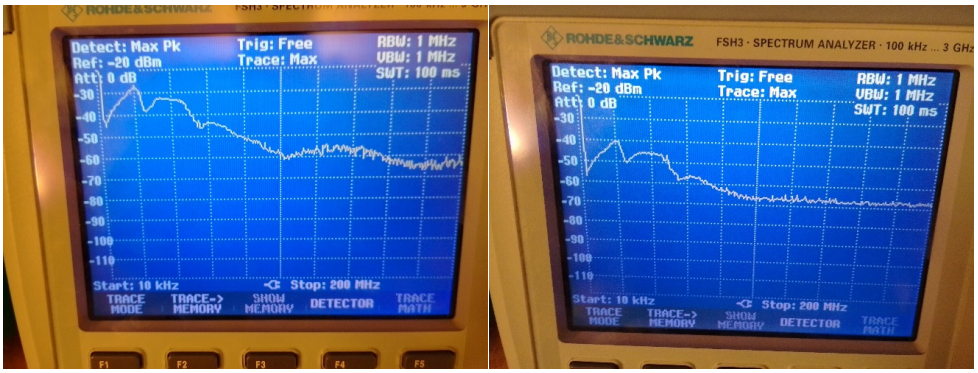

Fig. 6. Measured spectrum (10 kHz–200 MHz) from the VFD unit: the left plot shows the spectrum when the system was running, and the right plot shows the spectrum after the unit was shielded. The shielding reduced the signal level by approximately 10 dB across the entire frequency range.

3. RESULTS

Methods to reduce harmful emissions are relatively straightforward. The use of shielded cables, especially shielded motor cables, is one of the simplest and most effective ways to minimise radiative interference. Additionally, common-mode filters, when installed around cables or individual wires, provide another effective mitigation technique. Proper grounding is also a critical measure for preventing radiative emissions.

Conductive interference can be mitigated using various filter solutions. It is important to recognise that conductive and radiative emissions are closely interconnected. Radiative interference can result from conductive emissions, as leakage voltages and currents may transfer to metallic structures, which can then function as antennas, converting the interference into radiative emissions. In this study, we primarily focused on radiative electromagnetic interference from the motor cable, specifically the cable connecting the VFD to the motor. We conducted various measurements to compare the interference levels between non-shielded and shielded cables.

Additionally, radiative electromagnetic

interference was assessed and measured from the input cables and the VFD unit itself. The shielding methods we employed were straightforward to implement and, as noted earlier, proved highly effective. As VFDs become more prevalent in consumer electronics and household applications, understanding their EMC properties is crucial.

4. CONCLUSIONS

The present study serves as a demonstrative example of the importance of EMC design, particularly in VFD applications. VFDs are potent sources of EMI and should never be used without appropriate shielding solutions. Additionally, this study will form the basis for a future laboratory exercise for bachelor-level students, providing hands-on experience with EMC-related topics.

In the exercise, students will first identify the sources of EMI within the system. They will then implement shielding techniques to mitigate radiative EMI and validate the effectiveness of their solutions through measurements. This educational application was a key motivation behind the study. The test setup was designed to be portable, facilitating its use across different laboratory spaces. With this setup, students can directly observe how the mitigation techniques impact the overall EMI performance.

Similar interference behaviour was observed in larger VFD systems in the kilowatt range, particularly when operated with unshielded motor cables. In high-quality VFDs, EMI properties are carefully addressed, i.e., the VFD unit does not generate as much radiative interference as the unit tested in this study.

Future investigations should also focus on conductive interference. VFDs generate harmonic voltages and currents, which can cause significant issues if effective mitigation measures, such as EMI filters, are not implemented. Furthermore, performing radiative EMI measurements in the far-field would be of interest. Since the EMI strength was considerable in the near-field, it is likely that interference could also be detected in the far-field.

REFERENCES

1. Post, C. F. (2014). EMC design considerations for medium to large variable speed drives in industry. In *31st URSI General Assembly and Scientific Symposium (URSI GASS),* (pp. 1–4). Beijing, China, 2014. https://doi.org/10.1109/URSIGASS.2014.6929538
2. Zare, F. (2009). EMI in Modern AC Motor Drive Systems. *IEEE EMC Society Newsletters*, summer(222), 53–58.
3. Kosobudzki, G., & Florek, A. (2017). EMC Requirements for Power Drive Systems. *Power Electronics and Drives, 2* (2), 127–135. https://doi.org/10.5277/ped170207
4. Novak, J., Simanek, J., Cerny, O., & Dolecek, R. (2008). EMC of Frequency Controlled Electric Drives. *Radioengineering, 17* (4), 101–105.
5. Novak, J., Dolecek, R., & Cerny, O. (2009). EMC Specific Problems of Frequency Converters Used at Interlocking Device. *Radioengineering, 18* (4), 606–610.
6. Yuan, L., Zhang, J., Liang, Z., Hu, M., Chen, G., & Lu, W. (2023). EMI Challenges in Modern Power Electronic-Based Converters: Recent Advances and Mitigation Techniques. *Front. Electron., 4,* 1274258. https://doi.org/10.3389/felec.2023.1274258

7. Takahashi, S., Wada, K., Ayano, H., Ogasawara, S., & Shimizu, T. (2022). Review of Modeling and Suppression Techniques for Electromagnetic Interference in Power Conversion Systems. *IEEJ Journal of Industry Applications, 11* (1), 7–19. https://doi.org/10.1541/ieejjia.21006800
8. Miloudi, H., Miloudi, M., Ardjoun, S. A. E. M., Mahmoud, M. M., Telba, A. A., & Denai, M. (2024). Electromagnetic Compatibility Characterization of Start-Capacitor Single-Phase Induction Motor. *IEEE Access, 12*, 2313–2326. https://doi.org/10.1109/ACCESS.2023.3349018
9. Zeliang, Z., Yihua, H., Xiao, C., Jewell, G. W., & Li, H. (2021). A Review on Conductive Common-Mode EMI Suppression Methods in Inverter Fed Motor Drives. *IEEE Access, 9*, 18345–18360. https://doi.org/10.1109/ACCESS.2021.3054514
10. Kallunki, J. (2024). A Practical Solution to Reduce Interference from Led Lights. *Latvian Journal of Physics and Technical Sciences, 61* (1), 35–42. https://doi.org/10.2478/lpts-2024-0004
11. Kallunki, J. (2024). An Evaluation of the Portable Anechoic Chamber for Electromagnetic Compatibility (EMC) Studies. *Journal of Automation, Electronics and Electrical Engineering, 6* (2), 35–44. https://doi.org/10.24136/jeee.2024.006
12. Evans, R. W. (1997). *Design Guidelines for Shielding Effectiveness, Current Carrying Capability, and the Enhancement of Conductivity of Composite Materials under Contract NAS8-39983.* National Aeronautics and Space Administration.

sciendo

LATVIAN JOURNAL OF PHYSICS
AND TECHNICAL SCIENCES
2025, N 3

DOI: 10.2478/lpts-2025-0020

REDESIGN OF THE AD820 SINGLE-CHANNEL CIRCUIT FOR THE DEVELOPMENT OF THE ARD820 LOW-NOISE RAIL-TO-RAIL OPERATIONAL AMPLIFIER

D. Kostrichkin[1], S. Rudenko[1], M. Lapkis[1], A. Atvars[2*]

[1]JSC RD ALFA Microelectronics,
240 Latgales Str., Riga, LV-1063, LATVIA
[2]Photonics Lab, Institute of Astronomy,
Faculty of Science and Technology, University of Latvia,
19 Raina Blvd., Riga, LV-1586, LATVIA
*e-mail: aigars.atvars@lu.lv

The task of this study was to design and later produce a low-power (single supply 5–30 V, dual supply ± 2.5 V and ± 15 V) rail-to-rail operational amplifier aRD820 with low voltage noise (<4 μV, p-p. 0.1 to 10 Hz), ultralow input bias current (< 15 pA), and low offset voltage (< 500 μV) characteristics. Similar characteristics are presented by Analog Devices chip AD820. Thus, the task of the design team was to adapt the prototype circuity of AD820 to our technological capabilities, modify the circuit, if necessary, and eliminate any deficiency of the prototype. The input stage module got source followers at the input of the operational amplifier. The second stage module was modified to be more symmetric. The output stage module obtained additional resistors and capacitors to achieve frequency compensation. One FET transistor in the current reference module was substituted with other elements. Simplified electric schemes of these modules of AR820 and aRD820 are presented. The performance of modules of modified electric schemes was tested in Simulink software. Simulations of the full electric scheme for aRD820 demonstrated characteristics similar to those of AD820 data tables. Later production of the aRD820 chip and measurements demonstrated that the planned characteristics of the operational amplifier were met.

Keywords: *AD820, circuit, electric scheme, operational amplifier, rail-to-rail.*

1. INTRODUCTION

An operational amplifier (op-amp) is an essential component in electronics that amplifies voltage [1]–[3]. Op-amps are widely used in various applications, such as signal processing, filtering, and mathematical operations [4], [5] because they can increase the strength of weak electrical signals and perform complex tasks with simple configurations. While traditional operational amplifiers are designed to amplify voltage, operational transconductance amplifiers (OTAs) provide a current output, making them useful in several medical applications [6], [7]. CMOS operational amplifiers have gained widespread adoption in recent years due to their low power consumption and integration capabilities [8], [9], yet amplifiers based on complementary bipolar technology [10], [11], like the AD820, continue to excel in precision applications. Each technology serves distinct purposes: CMOS is ideal for modern, low-power digital systems, while bipolar amplifiers remain the gold standard for low-noise, high-precision analogue applications.

A rail-to-rail amplifier is a type of operational amplifier designed to utilise the full range of the power supply voltage, from the lowest supply rail (ground) to the highest supply rail (positive voltage). This means it can produce output voltages that go very close to the minimum and maximum supply voltages, enhancing its versatility in low-voltage applications. The development of low-voltage operational amplifiers capable of achieving rail-to-rail input and output operation has been a significant advancement in precision signal processing. One notable design achieves this functionality by incorporating a nested-loop frequency-compensation technique, allowing stable performance even at supply voltages as low as 1.5 V [12]. Operational amplifiers are also used for high supply voltages, e.g., 30 V [13]. For applications requiring rail-to-rail input and output, new bulk-driven amplifier designs offer significant performance improvements. The use of composite transistor arrays has been shown to provide superior voltage gain without sacrificing power efficiency [14]. A recent design using a folded cascode architecture and Class AB output stage achieved rail-to-rail performance with low power consumption and high gain [15]. Another work proposes a rail-to-rail auto-zero operational amplifier using a time-interleaved charge pump circuit to ensure low power consumption and low offset voltage [16].

Operational amplifiers could be single-stage, two-stage, three-stage, and multistage. The comparison of single and two-stage CMOS op-amps showed that single-stage op-amp is more stable and operates for longer duration of time, while two-stage op-amp produces a larger output with lower noise [17].

The design of operational amplifiers for space applications requires consideration of radiation-induced effects, such as total ionizing dose (TID). Techniques such as hardened-by-design (RHBD) have been successfully implemented to mitigate these effects, as demonstrated in the development of a rail-to-rail operational amplifier resilient to radiation doses up to 500 krad(Si) [18].

Analog Devices, Inc. developed a technology for vertical NPN and PNP transistors known as complementary bipolar (CB) technology. This innovation significantly enhanced various chip solutions, including operational amplifiers. Leveraging this technology, Analog Devices, Inc. intro-

duced several operational amplifiers – single-channel AD820 (1993), two-channel AD822 (1994), and four-channel D824 (1995). These amplifiers exhibited exceptional characteristics regarding input current, noise levels, dynamic performance, and low power consumption. While they did not achieve the highest possible specifications in any single parameter, their balanced performance made them highly useful in many applications, particularly those requiring low input currents.

The AD820 is a precision, low-power operational amplifier developed by Analog Devices, Inc., tailored for single-supply applications that demand high accuracy and efficiency. It operates over a wide supply voltage range (single supply 5–30 V, dual supply ± 2.5 V and ± 15 V), making it suitable for both low-voltage portable devices and higher-voltage industrial systems. Key features include an ultralow input bias current of less than 15 pA and a low input offset voltage below 500 μV, which minimise errors when interfacing with high-impedance sources and enhance overall measurement precision. The amplifier also exhibits low voltage noise, specified at less than 4 μV peak-to-peak within the 0.1 Hz to 10 Hz frequency band, crucial for applications involving low-frequency, low-level signal amplification, such as precision instrumentation and sensor signal conditioning. Moreover, the AD820 offers a rail-to-rail output swing, allowing the output voltage to approach the supply rails closely and thereby maximizing the dynamic range, especially in low-supply-voltage scenarios. Despite its low power consumption, with a typical quiescent current of only 800 μA, the amplifier maintains a moderate gain-bandwidth product suitable for various analogue signal processing tasks. Its design effectively minimises both flicker (1/f) noise and thermal noise contributions, ensuring signal integrity across varying temperatures and supply voltages. These attributes make the AD820 an excellent choice for precision analogue applications where low noise, ultralow input bias current, and low offset voltage are essential, including medical instrumentation, active filtering, and high precision data acquisition systems.

The task of this study was to design and later produce a low power (single supply 5–30V, dual supply ± 2.5V and ± 15 V) rail-to-rail operational amplifier with low voltage noise (<4 μV, p-p. 0.1 to10 Hz), ultralow input bias current (< 15pA), and low offset voltage (< 500 μV) characteristics. Similar characteristics are presented by Analog Devices chip AD820. Thus, the task of the design team of RD Alfa Microelectronics was to adapt the prototype circuity of AD820 to our technological capabilities, modify the circuit, if necessary, eliminate any deficiency of the prototype, and utilise previous results obtained from designing the low-voltage four-channel amplifier microchip aRD824 [19], [20].

The list of planned parameters of aRD820 compared to the datasheet values of AD820 is given in Table 1. It shows that aRD820 is expected to achieve similar characteristics to AD820 and even exceed in some parameters.

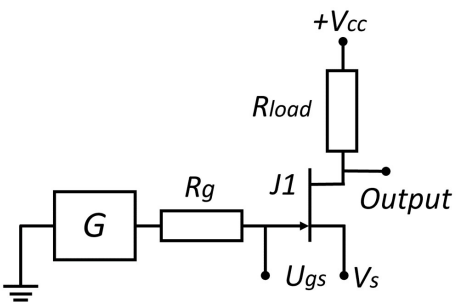

Fig. 1. Electric scheme to test FET transistors. $+V_{cc}$ – supply voltage, R_g – generator resistor, R_{load} – load resistor, $J1$ – FET transistor, G – signal generator, V_s – voltage on source, U_{gs} – voltage gate source.

Table 1. Planned Specification of an Operational Amplifier
aRD820 Chip and Specification of Analog Devices AD820 Chip

No.	Parameter	Tempera-ture*	aRD824 (planned)		AD820 (AD820A) [21]			Units
			Minimal values	Maximal values	Minimal values	Typical	Maximal values	
1	Offset Voltage	T_{NORM} T_{MIN} to T_{MAX}	-0.5 -1.5	0.5 1.5		0.1 0.5	0.8 1.2	mV
2	Input Bias Current	T_{NORM} T_{MIN} to T_{MAX}	-15 -4000	15 4000		2 500	25 5000	pA
3	Input Offset Current	T_{NORM} T_{MIN} to T_{MAX}	-10 -500	10 500		2 500	20	pA
4	Large Signal Voltage Gain R_L = 1 kΩ R_L = 2 kΩ R_L = 10 kΩ R_L = 100 kΩ	 T_{NORM} T_{NORM} T_{MIN} to T_{MAX} T_{NORM} T_{MIN} to T_{MAX} T_{NORM} T_{MIN} to T_{MAX}	 10 50 250 180		 15 10 80 80 400 400	 30 150 1000		V/mV
5	Output Voltage (High)** I_{SOURCE} = 20 **µA** I_{SOURCE} = 2.5 mA I_{SOURCE} = 15 mA	 T_{NORM} T_{MIN} to T_{MAX} T_{NORM} T_{MIN} to T_{MAX} T_{NORM} T_{MIN} to T_{MAX}		 14 20 110 160 1500 1500		 10 80 800	 14 20 110 160 1500 1900	mV
6	Output Voltage (Low)*** I_{SOURCE} = 20 **µA** I_{SOURCE} = 2.5 mA I_{SOURCE} = 15 mA	 T_{NORM} T_{MIN} to T_{MAX} T_{NORM} T_{MIN} to T_{MAX} T_{NORM} T_{MIN} to T_{MAX}		 7 10 55 80 500 500		 5 40 300	 7 10 55 80 500 1000	mV
7	Voltage noise, 0.1 Hz to 10 Hz			4		2		**µV**, p-p

*T_{NORM} is +22 ± 3 °C for aRD820 and +25 °C for AD820. T_{MIN} to T_{MAX} is a temperature range (-60 ... +125 °C) for aRD820 and range (–40 ... +85 °C) for AD820.

**Output saturation Voltage (High) is the difference between the highest possible output voltage and the positive supply voltage.

***Output Saturation Voltage (Low) is the difference between the lowest possible output voltage and the negative supply rail.

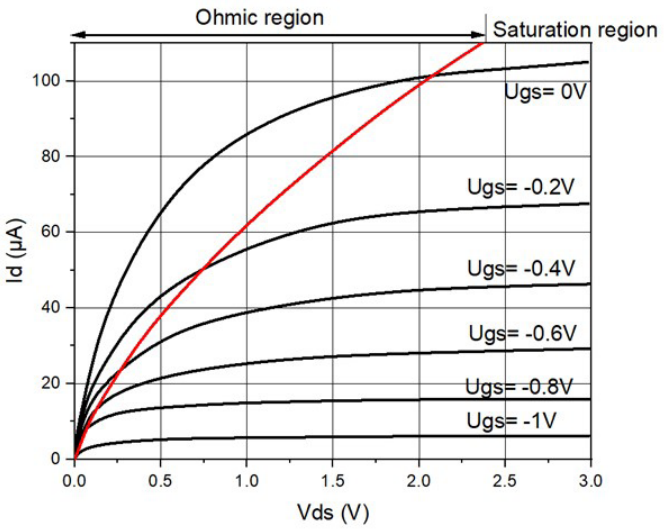

Fig. 2. Exit current-voltage characteristics FET transistor. V_{ds} – voltage drain source, I_d – drain current, U_{gs} – voltage gate source, red line – separation between ohmic and saturation regions for various U_{gs}.

2. INSPECTION OF AD820, REPLICATION, AND DRAWBACK ANALYSIS

We inspected AD820 chip and derived its electric scheme. Then, we replicated this electric scheme on a chip produced in our production facilities. Tests on several such chips showed drawbacks that did not allow them to reach the performance of AD820. We analysed the drawbacks and came to several conclusions.

First, our N-channel FET transistors are inferior to similar transistors used in the input stages and reference source circuits of the AD820. Specifically, amplifier stages using these transistors have poor noise characteristics. The noise voltage swing Vinp-p, referenced to the input, in the range of 0.1 Hz to 10Hz in the circuit shown in Fig. 1 is 5 μV...10 μV, which is more than five times the corresponding value obtained in a similar circuit using an NPN transistor.

Second, the output voltage-current characteristic of our FET transistors has a broader "Ohmic region" compared to the FET transistors of the AD820. The initial section of the voltage-current characteristic of our FET transistor is shown in Fig. 2. The "Ohmic region" is characterised by significantly lower transconductance (gm) values compared to the saturation region: $g_m = dI_d/dV_{gs}$, where dI_d – increment of a drain current I_d, and dV_{gs} – increment of a gate-source voltage V_{gs}. If the FET transistor enters the "Ohmic region" (i.e., the source voltage is close to the drain voltage), the circuit's gain significantly decreases. Since the input stage of the AD820 is similar to the circuit in Fig. 1, its gain undergoes the same changes. When the input voltage (V_{in}) increases to $+V_{cc}$ -2V... + V_{cc} -1V, the op-amp gain can drop to several hundred, especially in amplifiers with a higher gate cutoff voltage (in absolute value) V_{gs0} (the gate source voltage at which I_d becomes 0). Of two operational amplifiers with gate cut-off voltages of -2 V and -1 V, the gain

reduction for input signals close to $+V_{cc}$ will be more significant in the amplifier with the gate cut-off voltage of -2 V, since at equal V_{in} values, the V_{ds} value of these transistors will be lower by approximately 1 V (i.e., it will enter the "Ohmic region" earlier).

Third, our FET transistors have a large spread in gate cutoff voltages V_{gs0}, ranging from -0.5V to -2.5V. This leads to an inability to set the required reference current on crystals with extreme V_{gs0} values, resulting in a low yield of good chips. To demonstrate this assertion, we calculate the value of resistor R_2 (Fig. 3) needed to obtain a 20 μA current flowing through the FET transistor J2: $I_d = I_{d0}(1 - V_{gs}/V_{gs0})^2$, where I_d is the drain current, I_{d0} is the drain current when the gate-source voltage is 0, V_{gs} is the gate-source voltage, and V_{gs0} is the gate cut-off voltage. $V_{gs} = -I_d R_2$; we get: $I_d = I_{d0}(1 + I_d R_2/V_{gs0})^2$. The I_{d0} values obtained from the test FET transistors are as follows: for transistors with V_{gs0} = -0.5 V, I_{d0} is 32 μA. For transistors with V_{gs0} = -2.5 V, I_{d0} is 1600 μA. Substituting the values of V_{gs0} and I_{d0}, we get R_2 values of 5.2 kΩ (V_{gs0} = -0.5 V) and 110 kΩ (V_{gs0} = -2.5 V). This resistance range exceeds the adjustment capabilities of resistors available in our technological line.

Fourth, at drain-gate voltages (V_{dg}) greater than 22 V...25 V, the drain-gate reverse current increases sharply. It can exceed 1 μA, which is unacceptable for input transistors. Therefore, an additional circuit to limit Vdg is needed for the input transistors.

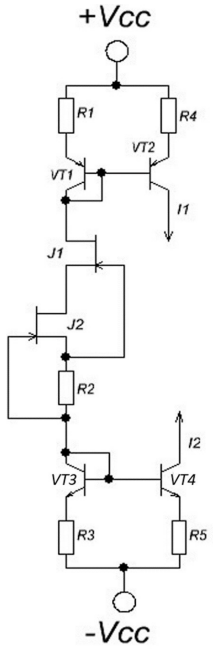

Fig. 3. Electrical scheme used for calculations. Vcc – supply voltage; R1–R5 – resistors; J1, J2 – FET transistors; VT2, VT3, VT4 – NPN transistors; I1, I2 – currents.

Fifth, it was found that produced thin-film resistors had poor characteristics. Therefore, they should be replaced by ion-implanted resistors [22].

Based on the conclusions outlined before, we proposed several modifications for the electric scheme of AD820 that would allow us to reach similar performance, but using strengths and limits of our production facilities. Changes were proposed for the input stage, second (pre-final) stage, output stage, and current reference.

3. PROPOSED DESIGN OF OPERATIONAL AMPLIFIER ARD820

In Microsim software, we developed a model of the AD820 electrical schematic and configured the parameters of the electronic components within limits that can be reached by our production line, e.g., parameters for FET transistors. The simulation results showed that we could not achieve the desired parameters corresponding to the technical data of AD820 [21]. Therefore, several modifications to the elec-

tric scheme of AD820 were proposed and tested. Finally, we got an electric scheme for operational amplifier aRD820 with good simulation performance corresponding to the targeted parameters (see Table 1). Below, we describe several modules of the aRD820 electrical schematic and explain why its performance surpasses that of the AD820 schematic. It should be emphasised that the AD820 electrical schematic is well suited for the production capabilities of Analog Devices, Inc., which manufactures the AD820 that allows it to reach good performance. However, due to the limitations of our production line, this electric scheme does not allow us to reach the expected performance.

3.1. Modification of Input Stage Module

The input stage of an op-amp is designed to receive the input signal and provide initial amplification. This stage is typically implemented as a differential amplifier, which amplifies the voltage difference between the inverting and non-inverting inputs. One of the key functions of this stage is to reject common mode signals, ensuring that only the differential signal is amplified. The input stage is crucial for maintaining a high input impedance, which minimises the loading effect on the preceding circuit. In addition, the bias circuit within the input stage ensures that the transistors operate in the correct region, thus stabilising the overall performance.

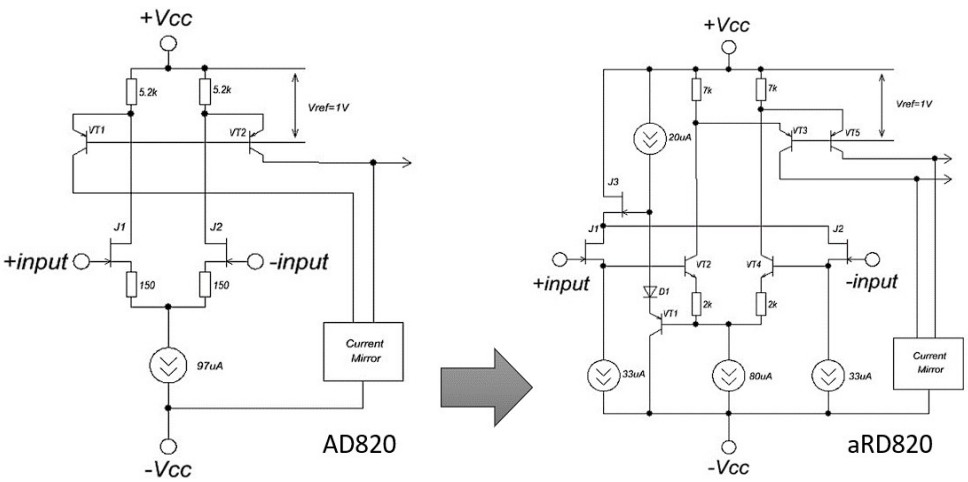

Fig. 4. A simplified electric scheme of the input stage modules of AD820 and aRD820.

Figure 4 shows simplified circuits of the AD820 and aRD820 input stages. By modifying the aRD820 input stage circuit relative to the AD820, we attempted to solve three problems. First, we attempted to reduce the noise of the input stage. Second, we expanded the input signal range toward voltages close to +Vcc. Third, we intended to limit and stabilise the Vds voltage of the input transistors. As indicated above, implementing the input stage as given for AD820 could result in an input noise voltage swing (Vinp-p) of 5 μV to 10 μV in the range of 0.1 H to 10 Hz. Therefore, it was proposed to place source followers J1, J2 at the input of the operational amplifier. This configu-

ration should reduce noise by five times or more. At the same time, using source followers and a differential pair of NPN transistors VT2 and VT4 allows raising the upper limit of the allowable common-mode input signal by at least 0.4 V (since the voltages at the drains of J1 and J2 in these cases are +Vcc - Vref + Vbe for AD820 and +Vcc for aRD820).

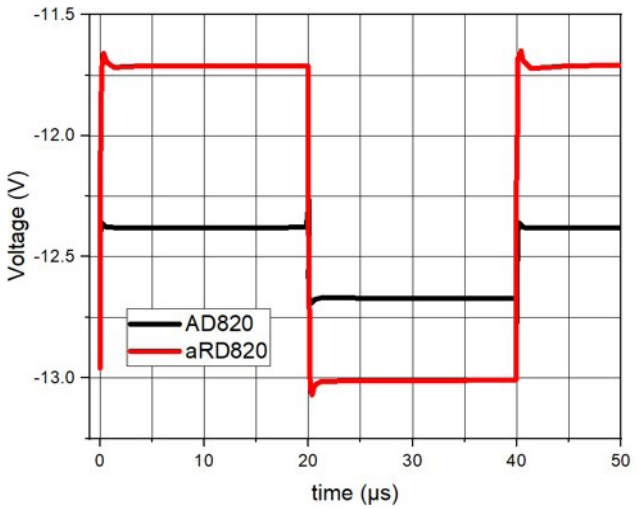

Fig. 5. Signal response of input stage modules of AD820 and aRD820.
Vcc = ±15 V, V(+inp) = 10 V, V(-inp) = 9.9 V ... 10.1 V. Black line: Voltage on the collector of the transistor VT2 of AD820 scheme (Fig. 4), Vout(p-p) = 1.25 V. Red line: Voltage on the collector of transistor VT5 of aRD820 scheme (Fig. 4), Vout(p-p) = 1.5 V.

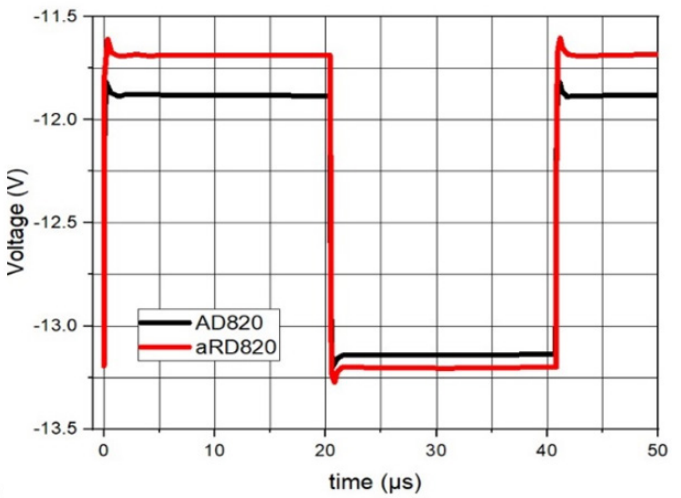

Fig. 6. Signal response of input stage modules of AD820 and aRD820.
Vcc = ±15 V, V(+inp) = 13 V, V(-inp) = 12.9 V ... 13.1 V. Black line: Voltage on the collector of transistor VT2 of AD820 scheme (Fig. 4), Vout p-p = 0.33V. Red line: Voltage on the collector of transistor VT5 of aRD820 scheme (Fig. 4), Vout p-p = 1.3 V.

Figures 5 and 6 illustrate the described advantage of the circuit for aRD820 in Fig. 4, obtained from computer models for input signals close to +Vcc. Instead of a current mirror, a resistive load of 50 kΩ was used, and the FET transistors' gate cut-off voltage was assumed to be Vgs0 = -2 V. In Fig. 5, signal response of input stage modules of AD820 and aRD820 schemes are presented. Parameters used in simulations were Vcc = ±15 V, V(+inp) = 10 V, and V(-inp) is changed from 9.9 V to 10.1 V. The black line corresponds to the voltage Vc(VT2) on the collector of the transistor VT2 of AD820 scheme (Fig. 4) giving peak-to-peak value Vout(p-p) = 1.25 V. The red line corresponds to the voltage Vc(VT5) on the collector of the transistor VT5 of aRD820 (Fig. 4) giving peak-to-peak value Vout(p-p) = 1.5 V.

Figure 6 shows signal response of input stage modules of AD820 and aRD820 schemes. Parameters used in simulations were Vcc = ±15 V, V(+inp) = 13 V, and V(-inp) is changed from 12.9 V to 13.1 V. The black line corresponds to the voltage Vc(VT2) on transistor VT2 of AD820 (Fig. 4) giving peak-to-peak value Vout(p-p) = 0.33 V. The red line corresponds to the voltage Vc(VT5) on transistor VT5 of aRD820 (Fig. 4) giving peak-to-peak value Vout(p-p) = 1.3 V.

Figures 5 and 6 show that for the change of the input signal from +13 V to + 10 V, the gain of the circuit of AD820 drops four times, while the gain drop of the circuit of aRD820 is only 15 %. Similar simulations were made with parameters Vcc = ±15 V, V(+inp) = 14.5 V and V(-inp) change from 14.4 V to 14.6 V. Then, voltage Vc(VT2) on the collector of the transistor VT2 of AD820 showed peak-to-peak value Vout(p-p) = 26 mV. Correspondingly, voltage Vc(VT5) on the collector of the transistor VT5 of aRD820 showed peak-to-peak value Vout(p-p) = 28 mV.

At high supply voltages (+Vcc = +30 V; -Vcc = 0 V) and low input signals (Vin < 7 V), there is a significant reverse current at the drain-gate junctions of the input transistors J1, J2 of (Fig. 4, electrical scheme AD820), causing the input current of the operational amplifier to exceed the norm. To avoid this effect, the aRD820 uses a circuit limiting the voltage in the drains of the input transistors, including the transistors VT1, J3, the diode D1, and a current source of 30 μA. This ensures that the voltages at the drains of J1 and J2 are approximately equal to Vin - 2Vgs +Vbe, where Vgs is the gate-source voltage of J1 (J2). The average Vgs is -1.2 V, and Vbe is 0.65 V. Therefore, the drain voltages of J1 and J2 will be Vin + 3.05 V, and Vdg at the input signals Vin < +Vcc - 3.05 V remain almost constant at 3.05 V.

The input stage circuit of aRD820 has two drawbacks. First, the introduction of an additional stage increases the phase shift and theoretically reduces the stability. Second, the introduction of an additional stage imposes a restriction on the gate cut-off voltage Vgs0 of the input transistors J1 and J2. The gate cutoff voltage must not exceed - 0.8 V ... -0.9 V (i.e., it must be between -0.9 V and -2.5 V). Otherwise, the differential stage transistors VT2, VT3 will close when an input signal close to -Vcc is applied. Considering the advantages and disadvantages of the input stage circuit of aRD820, we deemed it feasible to use this circuit, addressing stability issues by modifying the pre-final stage, using additional frequency compensation in the final stage, and selecting wafers based on the Vgs0 parameter of test FET transistors during manufacturing.

During the design of the input stage, special attention was paid to minimising the offset voltage of the operational amplifier. In AD820, it does not exceed 800 μV and

is achieved by laser trimming of thin-film resistors located in the sources of the input FET transistors. Since we decided not to use thin-film resistors, we proposed to use an array of cutting resistors with fuses, blown by current, in aRD820. The trimming resistors are located in both arms of the lower NPN transistors of the current mirror of aRD820. The resistor values are chosen so that the adjustment range of the operational amplifier offset voltage is from -10 mV to +10 mV, with the total voltage drop across the resistors not exceeding 100 mV.

3.2. Modification of the Second (Pre-final) Stage Module

Typically, the second stage, also known as the gain stage, provides most of the op-amp's voltage gain. This stage may employ a common emitter or common source amplifier configuration, which enables high-voltage amplification. The high gain of this stage allows the op-amp to amplify even very small input signals effectively. Additionally, this stage ften includes frequency compensation, typically in the form of a Miller compensation capacitor, which helps to stabilise the amplifier by controlling the bandwidth and preventing oscillations. This ensures that the op-amp remains stable across a wide range of frequencies. For our scheme of aRD820, the main gain of op-amp was performed at the first stage.

Figure 7 shows simplified circuits of the second (pre-final) stages of AD820 and aRD820. The second stage of aRD820 has a symmetrical structure, resulting in equal signal propagation times in the upper and lower arms. In AD820, the additional signal delay in the upper arm (VT1-VT3-VT2-VT4) is compensated by the parallel connection of capacitor C1. Calculations showed that the signal delay (and, consequently, phase shift) in the circuit in the aRD820 scheme is 3.5 times less than in the circuit in the AD820 scheme, even at lower operating currents in the stage. Thus, the circuit of aRD820 will provide greater stability to the operational amplifier compared to the circuit of AD820. Additionally, the circuit of aRD820 uses additional emitter followers VT3, I3, and VT4, I4 to reduce the operational amplifier's offset voltage. They ensure identical input currents of the stage for any β values of the Npn and Pnp transistors.

3.3. Modification of Output Stage Module

The output stage of an operational amplifier is responsible for driving the load connected to the op-amp's output. To achieve this, the output stage often uses a push-pull configuration, which can both source and sink current, making it highly efficient and capable of driving low-impedance loads. This stage provides current gain and reduces output impedance, ensuring that the op-amp can deliver sufficient current to the load without significant distortion. In some designs, a buffer is also used in the output stage to isolate the high-gain second stage from the load, further improving performance.

Figure 8 shows simplified circuits of the output stages of AD820 and aRD820. To compensate for the increased phase shift introduced by the VT2 and VT3 transistors in the aRD820 input stage (see Fig. 4), frequency compensation was proposed in the output stage. The compensation elements are C1, C2, R1, and R2.

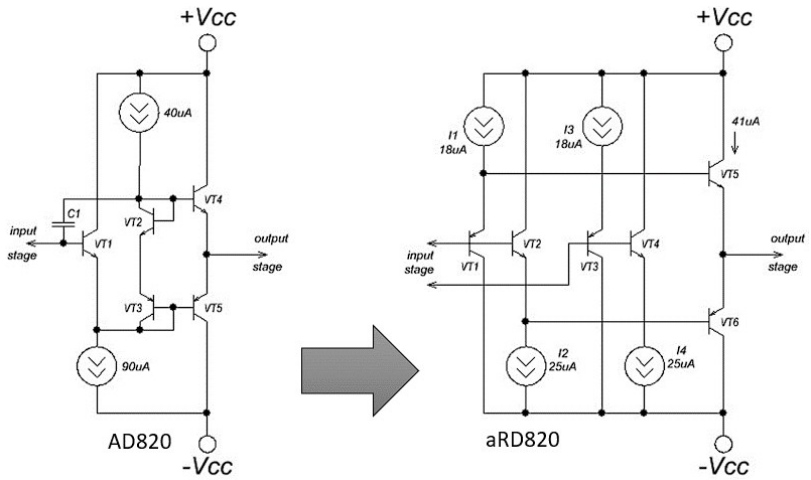

Fig. 7. Simplified electric schemes of the second (pre-final) stage modules of AD820 and aRD820.

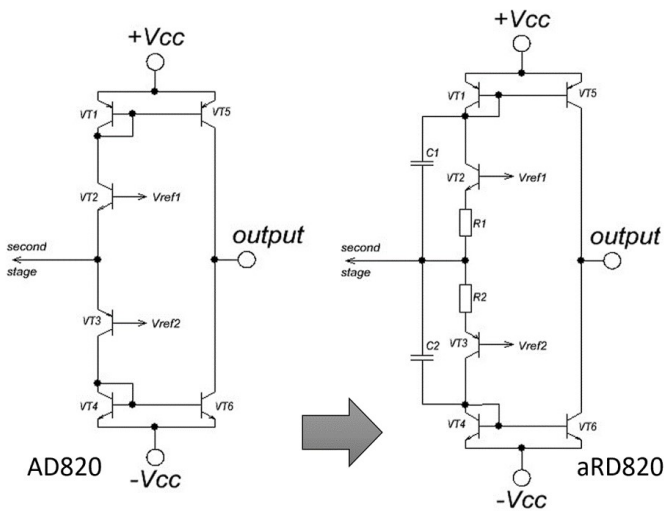

Fig. 8. Simplified electric schemes of the output stage modules of AD820 and aRD820.

Figures 9 and 10 illustrate a comparative analysis of the amplitude-frequency and phase-frequency characteristics of simulated signals of the circuits AD820 and aRD820. The parameters used in simulations were Vcc = ±15V, VACinp = 1mV, Rload = ∞, and Cload = 0. The gain of the output stage of aRD820 is lower than that of the circuit in AD820, but we considered this acceptable due to the ample margin for this parameter. The phase-frequency characteristic of the circuit of aRD820 appears preferable to that of AD820 scheme. The phase margin of the circuit of AD820 at 3MHz is 68.6 degrees, while for aRD820 it is 89.6 degrees. The frequency of 3 MHz was chosen because it is close to the unity gain frequency of the operational amplifier. The operational amplifier is considered stable with a phase margin of at least 45 degrees at the unity gain frequency.

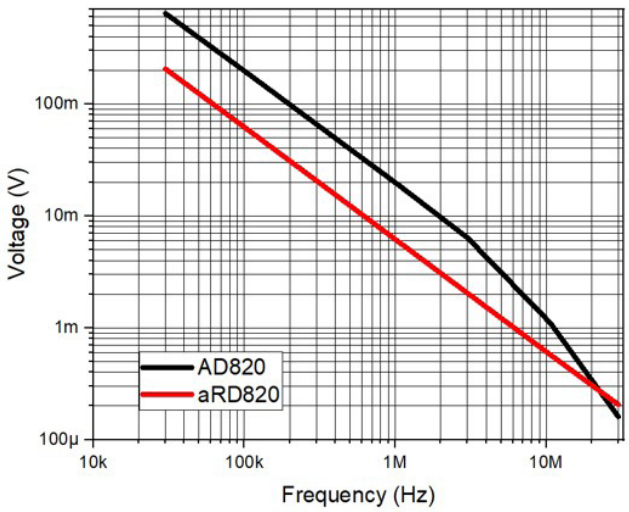

Fig. 9. Simulation of output module of operation amplifiers AD820 and aRD820. Voltage vs. frequency.

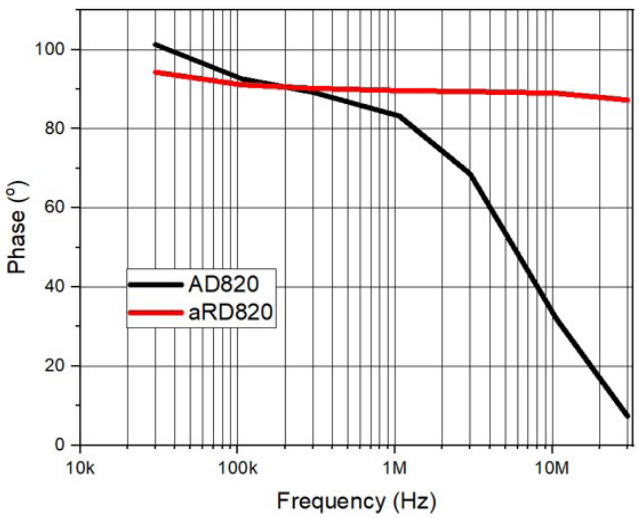

Fig. 10. Simulation of output module of operation amplifiers AD820 and aRD820. Phase vs. frequency.

3.4. Modification of the Current Reference Module

The current reference circuit is a fundamental component that ensures stable operation of the op-amp under varying conditions, such as changes in temperature or power supply voltage. The current reference typically consists of a constant current source and current mirrors, which provide a stable bias current to the transistors in both the input and second stages. This stable biasing ensures consistent operation, allowing the op-amp to maintain its performance across a range of operating conditions.

As described earlier, using a reference source circuit of AD820 would inevitably result in a low yield of good op-amp chips. Therefore, it was proposed to eliminate the FET transistors determining the reference current magnitude. Figure 10 shows the reference source circuits of the AD820 and aRD820. In the current reference circuit of aRD820, there is only one FET transistor that is used as an element to initiate the circuit, so it can also work with average characteristics. The reference current is set using the PNP transistor VT10. This current is approximately equal to the sum of the currents through resistors R3 and R4.

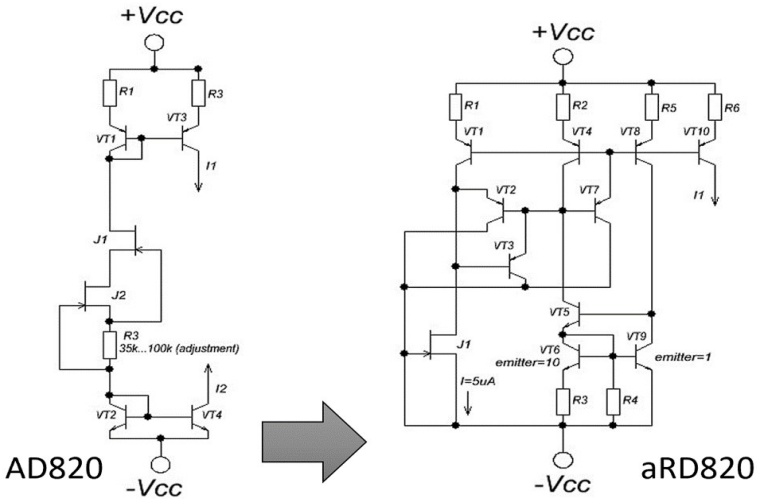

Fig. 11. Simplified electric schemes of the current reference modules of AD820 and aRD820.

The current through resistor R3 has a positive temperature coefficient, while the current through resistor R4 has a negative one. Thus, the resistances of R3 and R4 are chosen so that the current through VT10 remains constant over a temperature range of -40 °C to +85 °C. The exact reference current value will be set using trimming resistors connected in series with R6. The total drift of the reference current over the temperature range of -40 °C to +85 °C and the entire supply voltage range should not exceed 5 % to 10 %.

3.5. Simulations of the Full Electric Schemes of AD820 and aRD820

The modified components described above and the complete operational amplifier circuit were simulated using the Microsim circuit simulation program. Parameters of the components and the entire operational amplifier model were determined over temperature ranges (-40 °C to +85 °C), supply voltages (+30 V 0V; +5 V 0 V; ±2.5 V; ± 5V; ± 15V), input signals (-Vcc ... +Vcc), load capacitances (up to 350 pF), and output currents (up to 20 mA).

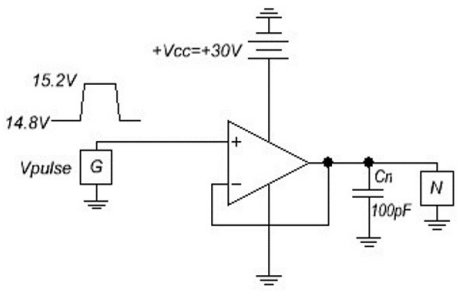

Fig. 12. Schematics to test the performance of operation amplifiers AD820 and aRD820.

Particular attention was paid to the impact of replacing thin-film resistors (as in AD820) with diffusion and ion-implanted resistors, as diffusion and ion-implanted resistors have significantly higher temperature coefficient of resistance. Simulation showed that this replacement did not significantly affect the operational amplifier parameters. Moreover, special attention was given to the model's dynamic properties, specifically its stability. To assess stability, an operational amplifier configuration with a gain of A = +1 and a load capacitance of Cn = 100 pF was used (Fig. 12).

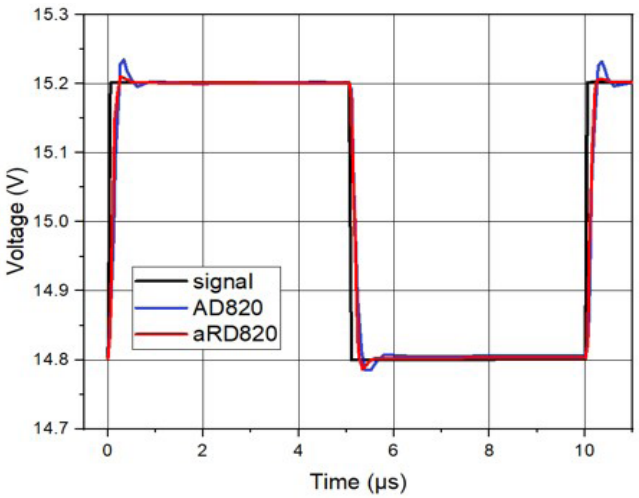

Fig. 13. Input and output signal oscillograms (simulations).

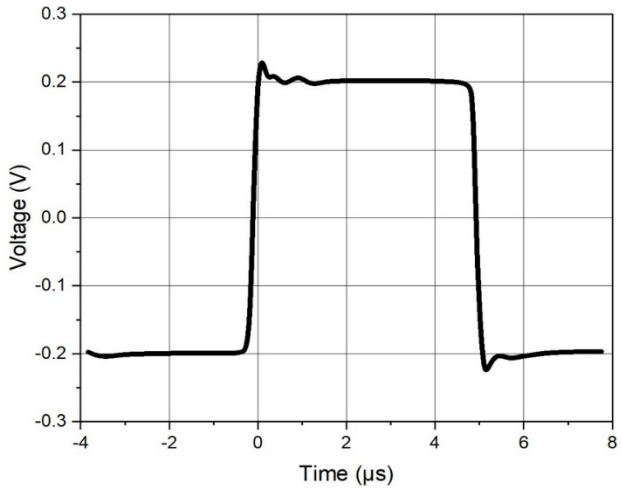

Fig. 14. Output signal oscillograms (tests).

Figure 13 shows the input and simulated output signal oscillograms of the AD820 and aRD820 models for the above configuration. As seen, the AD820 has a longer transition process during voltage jumps. Additionally, the aRD820 has a slightly higher slew rate. Finally, Fig. 14 shows the output signal oscillogram of the

actual aRD820 microchip (Vcc = ±15 V) demonstrating similar performance.

Later production and tests of aRD820 chips showed that the expected parameters of the operational amplifier given in Table 1 were achieved.

4. CONCLUSION

The task of the research was to design, construct, and test a single-channel, low-noise, rail-to-rail operation amplifier aRD820 with the specification given in Table 1, based on an initial prototype of the Analog Device AD820 chip. Due to limitations and specificity of available production lines, the construction of a chip that has implemented an electric scheme of AD820 prototype is not reasonable, as a high rate of damaged chips with poor performance will be obtained. Therefore, a modified electric scheme of AD820 prototype was proposed, allowing it to reach the targeted performance.

The input stage module got source followers at the input of the operational amplifier (Fig. 4). The second stage module was modified to be more symmetric (Fig. 7). The output stage module obtained additional resistors and capacitors to achieve frequency compensation (Fig. 8). One FET transistor in the current reference module was substituted with other elements (Fig. 11). The performance of modules with modified electric schemes was tested in Simulink software. Simulations of the full electric scheme for aRD820 showed that it exhibited characteristics like those of AD820 data tables. The aRD820 chip was produced, and measurements demonstrated that the planned characteristics of the operational amplifier were met.

ACKNOWLEDGEMENTS

The research activities were funded by the Latvian Recovery and Resilience Mechanism Plan under reform and investment direction 5.1.r. “Increasing Productivity through Increasing the Amount of Investment in R&D”, reform 5.1.1.r. “Management of Innovations and Motivation of Private R&D Investments”, investment 5.1.1.2.i. “Support Instrument for the Development of Innovation Clusters”, project No. 5.1.1.2.i.0/1/22/A/CFLA/002 “Competence Center of the Latvian Electrical and Optical Equipment Manufacturing Industry”.

REFERENCES

1. Horowitz, P., & Hill, W. (2015). *The Art of Electronics*. Cambridge University Press.
2. Huijsing, J. (2017). *Operational Amplifiers. Theory and Design* (3rd ed.). Springer International Publishing.
3. Franco, S. (2015). *Design with Operational Amplifiers and Analog Integrated Circuits* (4th ed.). McGraw-Hill Education,.
4. Jung, W. (2005). *Op Amp Applications Handbook*. Elsevier.
5. Yuce, E., & Minaei, S. (2024). *Passive and Active Circuits by Example*. Springer Nature, Switzerland. DOI:10.1007/978-3-031-44966-6

6. Manturshettar, S. V., & Sunita, M. S. (2019). A low noise low power operational transconductance amplifier for biomedical applications. In *2019 IEEE 16th India Council International Conference (INDICON), IEEE*, (pp. 1–4). DOI:10.1109/INDICON47234.2019.9030285
7. Almalah, N. T., & Aldabbagh, F. H. (2022). Inductanceless High Order Low Frequency Filters for Medical Applications. *International Journal of Electrical and Computer Engineering, 12,* 1299–1307. DOI:10.11591/ijece.v12i2.pp1299-1307
8. Sharma, D., & Nath, V. (2024). CMOS Operational Amplifier Design for Industrial and Biopotential Applications: Comprehensive Review and Circuit Implementation. *Results in Engineering, 22*, 102357. DOI:10.1016/j.rineng.2024.102357
9. Hussein, Z. S., & Motlak, H. J. (2024). Design Methodology for a Low-Power Two-Stage CMOS Operational Amplifier for Optical Receiver Applications. *Journal Europeen des Syst´emes Automatis`es, 57*, 815–822. DOI:10.18280/jesa.570320
10. Malhi, S., Salama, C., & Donnison, W. (1981). A Low-Voltage Micropower JFET/Bipolar Operational Amplifier. *IEEE Journal of Solid-State Circuits 16,* 669–676. DOI:10.1109/JSSC.1981.1051660
11. Bowers, D., & Wurcer, S. (1999). Recent developments in bipolar operational amplifiers. In Proceedings of the 1999 Bipolar/BiCMOS Circuits and Technology Meeting (Cat. No.99CH37024), IEEE, (pp. 38–45). DOI:10.1109/BIPOL.1999.803521
12. Huijsing, J., & Linebarger, D. (1985). Low-Voltage Operational Amplifier with Rail-to-Rail Input and Output Ranges. *IEEE Journal of Solid-State Circuits, 20*, 1144–1150. DOI:10.1109/JSSC.1985.1052452
13. Wang, C.-C., Tsai, T.-Y., Lu, W.-J., Chen, C.-L., & Wu, Y.-L. (2015). A 30 V Rail-to-Rail Operational Amplifier. *Microelectronics Journal, 46*, 911–915. DOI:10.1016/j.mejo.2015.06.015
14. Rodovalho, L. H., Rodrigues, C. R., & Aiello, O. (2023). Rail-to-Rail Input/Output Bulk Driven Class AB Operational Amplifier with Improved Composite Transistors. *Analog Integrated Circuits and Signal Processing, 115*, 279– 291. DOI:10.1007/s10470-023-02160-0
15. Guang, Y., & Bin, Y. (2012). Design and Analysis of a High-Gain Rail-to-Rail Operational Amplifier. *Procedia Engineering, 29*, 3039–3043. DOI:10.1016/j.proeng.2012.01.436.
16. Zhang, J., Zhang, C., Feng, Y., Zhang, Q., & Li, T. (2024). A 65 nm CMOS Rail-to-Rail Auto-Zero Operational Amplifier Based on Charge Pump Internal Power Supply. *Microelectronics Journal, 145*, 106098. DOI:10.1016/j.mejo.2024.106098
17. Menberu, T. (2023). Analysis and Comparison of Two Stage and Single Stage Operational Amplifiers Using 0.18 μm Technology. *American Journal of Physics and Applications, 10*, 72. DOI:10.11648/j.ajpa.20221006.11
18. Agostinho, P. R., Goncalez, O. L., & Wirth, G. (2016). Rail to Rail Radiation Hardened Operational Amplifier in Standard CMOS Technology with Standard Layout Techniques. *Microelectronics Reliability, 67,* 99–103. DOI:10.1016/j.microrel.2016.11.001
19. Kostrichkin, D., Rudenko, S., Lapkis, M, & Atvars, A. (2022). Development of Electric Scheme for 4-Channel Low Noise Rail-to-Rail Operational Amplifier aRD824 Based on AD824 Prototype. *Engineering for Rural Development, 21*, 962–968. DOI:10.22616/ERDev.2022.21.TF317
20. Kostrichkin, D., Rudenko, S., Lapkis, M., & Atvars, A. (2022). Simulation and Test Results of 4-Channel Low Noise Rail-to-Rail Operational Amplifier aRD824 Based on AD824 Prototype. *Engineering for Rural Development, 21,* 969–977. DOI:10.22616/ERDev.2022.21.TF318
21. Analog devices, Inc. (2011). *Data Sheet. AD820: Single-Supply, Rail-to-Rail, Low Power, FET Input Op Amp Data Sheet.* Available: https://www.analog.com/media/en/technical-documentation/data-sheets/AD820.pdf
22. Qian, M., & Wang, D. (2005). A Precision Physical Model for Three Terminal Diffused or Ion-Implanted Resistors. *Solid-State Electronics, 49*, 323–327. DOI:10.1016/j.sse.2004.11.002

sciendo

LATVIAN JOURNAL OF PHYSICS
AND TECHNICAL SCIENCES
2025, N 3

DOI: 10.2478/lpts-2025-0021

SHARED UNDERSTANDING OF LOCAL ENERGY COMMUNITY TERMINOLOGY: A CATALYST FOR INTERDISCIPLINARY COLLABORATION AND STAKEHOLDER ENGAGEMENT

A. Mutule[1*], I. Antoskova[1], P. Caroll[2], D. Biswas[2]

[1] Institute of Physical Energetics,
Smart Grid Research Centre,
14 Dzerbenes Str., Riga, LV-1006, LATVIA
[2] College of Business, University College Dublin,
Belfield, Dublin 4, IRELAND
*e-mail: amutule@edi.lv

Local Energy Communities (LECs) are an essential component of the clean energy transition in Europe. However, differences in terminology and interpretation across disciplines and among stakeholder groups present challenges to their effective development and operation. This paper explores three key concepts frequently encountered in LEC research and practice: prosumers and self-consumption, flexibility and demand response, and uncertainty. We provide both a Power Systems and an Operations Research (OR) perspective on each term, highlighting how varying definitions can lead to misunderstandings and misaligned decision models. By promoting greater clarity and shared understanding of these terms, we aim to support more effective interdisciplinary collaboration and the development of robust decision support tools for the design and operation of LECs.

Keywords: *Energy community, interdisciplinary collaboration, stakeholder engagement.*

1. INTRODUCTION

The European Union (EU) has ambitious plans for the transformation of the energy sector to provide secure, sustainable, competitive, and affordable energy for all Europeans. Modern fossil or nuclear power plants convert fuel to electricity with an efficiency of 30–40 % [1], [2]. Transporting electricity from power plants to homes and businesses incurs further losses of 1–4 % on the transmission level and 2–23% on the distribution level [3]. Therefore, decentralised decarbonised electricity generation forms part of the clean energy response to climate change and can reduce greenhouse gas emissions, improve supply security, and enhance resilience.

An essential element of the new electricity market design is active participation of empowered consumers. It aims to integrate higher proportions of renewable energy, allow prosumers (participants who both consume and produce electricity) to sell their excess self-generated electricity back to the grid, and allow them to benefit from cheaper electricity during off-peak periods. Interested citizens can group together to form a local energy community (LEC). LECs are called Advanced Energy Communities in the US, Smart Communities in Japan, and are gaining traction in Europe [4], [5].

The EU legislation is moving at pace to ensure a clean and fair energy transition at all levels of the economy. The Clean Energy Package makes the EU's electricity market more interconnected, flexible, and consumer-centred. The Electricity Market Directive is consumer-focused and outlines requirements for Member States and Regulatory Authorities to develop frameworks that allow for consumer participation in energy markets [6]. There are two definitions of an energy community: Citizen Energy Community (CEC) is defined in the Electricity Market Directive [6], and Renewable Energy Community (REC) is defined in the Renewable Energy Directive [7]. In both cases, the communities are autonomous legal entities based on open and voluntary participation with the purpose of providing environmental, economic, or social community benefits for their shareholders or members rather than financial profits. They are entitled to generate, consume, store, and sell renewable energy and may be allowed to participate in cross-border electricity exchanges.

2. RESEARCH CONTEXT AND MOTIVATION

Despite the progress made, variations in the interpretation and application of LEC-related concepts remain a major challenge. The European framework allows Member States considerable flexibility in shaping tailored definitions and support measures of LECs [8]. However, EU countries are at different stages in transposing EU legislation [9] and adopt various approaches to REC, CEC, and collective self-consumption [10]. Regulatory challenges exist in defining the general meaning, the main activities, control and operation, membership, ownership and boundaries of LECs [10]. Meanwhile, scientific literature presents multiple related concepts, such as community energy storage, community microgrids, energy sharing, smart energy community, prosumer com-

munity, energy hub, community wind, community solar, virtual power plant, energy cooperative, etc. While "energy community" and "community energy" are the most commonly used terms in research – they tend to focus more on economic objectives rather than social goals, primarily referring to the community as a place [11]. In line with this idea, de São José, Faria, and Vale [12] distinguish between place-based and non-place-based communities. Additionally, another widely used term in research is "integrated community energy system" [12].

Furthermore, LECs unite multiple actors, such as consumers and prosumers, local authorities, distribution system operators (DSOs), service providers (e.g., Energy Service Companies (ESCOs)), and property investors [13]. These stakeholders may have controversial objectives and interpret LEC-related concepts differently. Even within the research community, different disciplines have multiple perspectives and priorities, which pose a challenge for true multi- and inter-disciplinary research. Therefore, addressing terminological inconsistencies is essential for creating a foundation for more effective communication and alignment of goals among diverse stakeholders.

In this paper, we explore some of the terminology that occurs in LEC research and practice. We select a subset of terms, with provision of a power system and Operations Research (OR) and analytics perspective and interpretation of each term. We aim to enhance shared understanding of these terms, create insights into how the disciplinary perspectives may complement each other, or give rise to mutual confusion and misunderstanding.

3. METHODOLOGICAL APPROACH TO GLOSSARY DEVELOPMENT

The SEC-OREA (Supporting Energy Communities – Operational Research and Energy Analytics) team responded to the call to create "Novel Computational Approaches for Environmental Sustainability" in the CHIST-ERA (European coordinated research on long-term Information and Communication Technologies (ICT) and ICT-based scientific challenges) 2019 call. Focusing on developing algorithms and analytics to serve the needs of emerging LECs, the team aims to provide decision support tools for the design and operation of LEC. Multiple skills and sets of knowledge are needed for the successful and sustained participation of LECs in EU energy markets.

The project is broken into work packages targeting just some of the associated disciplines and activity areas: (1) Energy Analytics that aims to extract insights and understanding relationships between weather, renewable energy source (RES) generation, and electricity demand; (2) Optimisation algorithms to capture the interaction of stakeholders with competing perspectives such as the LEC and DSO; Optimisation algorithms to solve the energy dispatch problem taking into account the variability of RES; and Power Systems. All the approaches are designed to assist LECs in understanding the business, regulatory and power system's perspectives, and to make good decisions about how to design and operate their LEC infrastructure.

The SEC-OREA team is composed of researchers from Business Analytics, Operations Research and Power Systems disciplines. Business Analytics and Operations Research use quantitative approaches

to enable better decision making. Business Analytics uses data modelling to understand relationships in empirical data. Mathematical modelling represents decision actions and the objectives and constraints of different decision makers and stakeholders in a form that appropriate algorithms can solve.

OR has an established history of modelling and solving energy optimisation problems [14]. It takes a formal approach to specifying a problem statement for the optimisation problem to ensure that the problem inputs, outputs, data, and assumptions are stated. The problem statement is then formulated in mathematical notation with precise definitions for all concepts, symbols, and data parameters or distributions. See, for example, the approach to solving the Unit Commitment problem in [15]. The OR approaches simplify assumptions, such as that all data parameters are known with certainty. These models and approaches can be extended to incorporate uncertainty, such as [16]. Understanding uncertainty is a significant challenge for LECs that may not have adequate business or data analytics expertise, or access to high-quality empirical data to create appropriate statistical or machine learning models.

The SEC-OREA project tries to complement the analytics and algorithmic expertise of the team with power systems insights. In that way, complementary perspectives can be encoded in the mathematical models, which, when solved, should provide more insightful and useful recommendations for LECs. However, this comes with a significant challenge as each discipline has its own methodological approaches and terminology and naming conventions.

4. EXAMPLES OF TERMINOLOGICAL AMBIGUITY

4.1. Prosumers and Self-consumption

The EU legislation per se does not include a definition of the term "prosumer". However, the term generally refers to energy consumers – typically connected to the distribution grid – who also produce and/or store electricity at their premises [17]. While prosumers are often associated with RES, using RES is not a strict requirement. The rapidly evolving concept of prosumers includes the ability to sell surplus electricity and provide various energy services, either individually or through collective structures such as energy communities [18], [19]. Ertz et al. [20] propose a contemporary definition of prosumers, highlighting their contribution to economic, social, and environmental goals and underlining their broader impact beyond individual energy production: "prosumers create value for themselves and others independently or in collaboration with organisations, communities or peers."

As the role of prosumers continues to expand, the EU has introduced the concept of the active customer within its legal framework to provide clarity and support inclusive participation in the energy transition. According to the EU Electricity Market Directive [6], an "active customer means a final customer, or a group of jointly acting final customers, who consumes or stores electricity generated within its premises located within confined boundaries or, where permitted by a Member State, within other premises, or who sells self-generated electricity or participates in flexibility or energy efficiency schemes, provided that those activities do not constitute its primary commercial or professional activity."

Notably, active customers are not required to generate electricity themselves – participation in flexibility or energy efficiency schemes is also sufficient – and where generation is involved, it is not limited to RES.

A distinct group within this framework is the renewable self-consumer, who primarily generates and consumes renewable energy at their premises, most typically from solar panels. According to the EU Renewable Energy Directive [7], "renewables self-consumer means a final customer operating within its premises located within confined boundaries or, where permitted by a Member State, within other premises, who generates renewable electricity for its own consumption, and who may store or sell self-generated renewable electricity, provided that, for a non-household renewables self-consumer, those activities do not constitute its primary commercial or professional activity". Thus, self-consumption refers to the consumption of energy at the same location where it is generated.

The EU Renewable Directive [7] also introduces the term "jointly acting self-consumers", as "a group of at least two jointly acting renewables self-consumers who are located in the same building or multi-apartment block". Often, the term "collective-self consumption" is used to describe jointly acting self-consumers [21]. Some authors use the term "collective self-consumption" to refer to community-level energy consumption, where a portion of the electricity is consumed collectively within the community [22], [23].

From an analytics and optimisation perspective, these definitions and sets of assumptions have implications when designing a related mathematical optimisation model and solution approach. The OR provides a resource allocation framework by creating an appropriate mathematical model of the decisions, objectives, and constraints. Traditional OR approaches have focused on the perspective of DSO and TSO (transmission system operators), mainly focusing on cost minimisation [16], [24]. More recently, as the number and type of actors in energy markets have grown, the concerns and objectives of individuals or groups of are included in the models [25]. Incorporating the competing objectives of prosumers and energy communities alongside those of established system operators leads to more challenging mathematical models. Creating a shared interpretation of the remit and objectives of the actors in an ever-changing regulatory landscape is a challenge, but it is necessary to ensure valid assumptions are encoded in the mathematical models.

4.2. Flexibility and Demand Response

The literature uses multiple similar but slightly different terms when referring to system flexibility, such as demand-side flexibility, demand response, and flexibility services. The EU Regulation on Improving Electricity Market Design defines flexibility as "the ability of an electricity system to adjust to the variability of generation and consumption patterns and to grid availability, across relevant market timeframes" [26]. Sources of flexibility can include demand response, energy storage, and other non-fossil flexibility solutions [26].

Consequently, the literature tends to focus either on quantifying the available flexibility potential that flexibility resources can offer or on the flexibility requirements necessary for stable system operation [27]. Degefa et al. [28] review existing definitions of flexibility and propose three essential criteria that a consistent definition should include: the type of flexibility, the

duration of its activation, and the incentive for activating the flexibility resource. They also identify several categories of flexibility resources: demand-side (shiftable in advance, delay, or both), supply-side, stationary storage (standalone or with generation), mobile storage (e.g., electric vehicles), and operational flexibility (e.g., dynamic line rating) [28]. Furthermore, flexibility services refer to products delivered by flexibility resources, which can be offered as ancillary services in existing markets or under alternative arrangements [28], [29].

The EU Energy Efficiency Directive emphasises the role of demand-side flexibility as an important energy efficiency measure [30]. At the same time, the EU Electricity Market Directive [6] market defines demand response as "the change of electricity load by final customers from their normal or current consumption patterns in response to market signals, including in response to time-variable electricity prices or incentive payments, or in response to the acceptance of the final customer's bid to sell demand reduction or increase at a price in an organised market, whether alone or through aggregation". Although the terms "demand-side flexibility" and "demand response" are sometimes used interchangeably, demand response typically focuses on consumer actions triggered by price signals or incentives [18, 31].

Thus, when discussing LECs, it may be more accurate to refer to demand-side flexibility, as this term better captures the diverse behaviours and technologies involved at the community level. Referring to flexibility services may be more appropriate at a higher level or in advanced community models where LECs act as service providers.

In both cases, OR mathematical optimisation models can be formulated to support the participation of LECs in these markets. An optimisation technique called Mixed Integer Linear Programming (MILP) is used by [32] to optimise collective self-consumption of an energy community of prosumers, traditional consumers, and distributed storage units by scheduling members' loads and implementing a Demand Side Management. A MILP model is also proposed in [33], whose authors explore three different objectives for the different types of ECs. They note individual households do not offer sufficient flexibility for any significant grid enhancement, but collectively in an EC their aggregate flexibility has the potential to operate as an aggregator and provide flexibility directly to the DSO.

4.3. Uncertainty

The last concept we address in this paper is "uncertainty". There is inherent unpredictability in factors affecting energy generation, consumption, and management. This unpredictability arises from various sources, including fluctuations in renewable energy generation due to changing weather conditions, variations in consumer behaviour influenced by lifestyle and occupancy patterns, shifts in market dynamics such as energy prices and policy regulations, and potential inefficiencies or failures in energy systems and storage technologies [34], [35]. However, "uncertainty" is interpreted and treated differently by different actors in the clean energy transition.

For example, within the Operations Research mathematical modelling and optimisation communities, "uncertainty" is given a mathematical definition to bound the values that specific parameters can take. When there is no uncertainty in the problem parameters, computationally efficient techniques such as Linear Programming

are used to find optimal solutions in the deterministic case. More advanced computational approaches are needed when the parameters are uncertain. Stochastic Programming offers an optimisation framework to address uncertainties and can be used in energy generation, consumption, and market dynamics problems. Uncertainty is incorporated if the parameter statistical distributions are known by creating sample scenarios from the probability distributions. This enables decision-makers to develop contingency-based energy management strategies that account for variability in factors such as renewable energy output, consumer demand, and price fluctuations [36], [37]. Stochastic Programming models are bigger as they include additional constraints for the set of scenarios, and are, therefore, more challenging to solve than deterministic Linear Programming models.

Robust optimisation is another optimisation technique that considers uncertainty in the model parameters but captures uncertainty differently. The goal of this approach is to ensure that optimal decisions are robust to fluctuations in the model parameters, even for their worst-case realisations. An uncertainty set defines the range of variation of the uncertain parameter. Uncertainty can be characterised in the form of a box, polyhedral, or ellipsoidal uncertainty sets based on the shape of the variation of the uncertain parameters. When the model simultaneously accounts for the worst-case realisation of all uncertain parameters, the optimal solution might be highly conservative and computationally expensive. In order to control the degree of conservativeness, the decision maker can allocate a budget for the uncertainty [38] in the parameters by imposing a cap on the number of parameters that can fluctuate within their specified bounds. The corresponding uncertainty set is called the budget uncertainty set. Sometimes, uncertain parameters like photovoltaic (PV) solar power supply and electricity demand may exhibit a spatio-temporal correlation between them, allowing for further reduction of the uncertainty space, easing the computational burden of the problem. Uncertainty sets of correlated parameters can be constructed using data-driven approaches by defining the boundaries of the spread of the data points in the form of a convex hull based on the actual empirical distribution.

This OR treatment of uncertainty in Robust Optimisation leads to conservative solutions from a power systems perspective that ensure the power system operates reliably under fluctuations in power supply and demand once they fall within the range of the uncertainty sets.

The effectiveness of legislative efforts towards energy transition and decarbonization depends on how policymakers address uncertainty [39]. Scott et al. [39] examine how different methods of representing long-term uncertainty affect the evaluation of renewable support policies. They find that relying on deterministic or scenario-based approaches can lead to overly restrictive policies, whereas stochastic optimisation offers more accurate insights despite higher computational requirements. Furthermore, uncertainty in policy, RES support mechanisms, and market prices can hinder investment decisions [40], [41] and particularly the employment of LECs and citizen involvement [42]. At the same time, TSOs and DSOs face uncertainties in both planning [43] and operation [44], [45] of power systems. Velásquez et al. [43] distinguish between two types of uncertainty: aleatory uncertainty, which stems from inherent variability in natural processes (e.g., wind speed or human behaviour), and epistemic uncertainty, which arises from a lack of knowledge and can potentially be reduced

through further research. At the same time, Bessa et al. [44] focus on decision-dependent uncertainty, which describes the state of electric devices (available or unavailable).

5. CONCLUSION

In this paper, we have explored just three of the terms that occur in LEC research and practice: prosumers and self-consumption, flexibility and demand response, and uncertainty. Our dual perspectives from the power system and OR show that providing as much definition of the term as possible can assist the two disciplines in appreciating the scope and focus of the research problem. Without agreeing on definitions and sharing understanding, the concepts and research direction may be misaligned. This can lead to wasted effort and poor decision recommendations for LECs.

By creating a shared understanding, each discipline can bring its strengths and expertise to bear in a complementary fashion, aligning the efforts of multiple disciplines, in this case, power systems and OR, can enhance the outputs and solutions provided to support LEC participation in the clean energy transition.

ACKNOWLEDGMENT

This work emanates from research supported by the ERA-NET co-fund grant under the CHIST-ERA IV Joint Call on Novel Computational Approaches for Environmental Sustainability (CES), project "Supporting Energy Communities – Operational Research and Energy Analytics" (SEC-OREA).

REFERENCES

1. Taylor, P., Lavagne d'Ortigue, O., Trudeau, N., & Francoeur, M. (2008). *Energy Efficiency Indicators for Public Electricity Production from Fossil Fuels*. International Energy Agency (IEA). Available at: https://iea.blob.core.windows.net/assets/acaecb98-4430-4395-a4fa-d1a4d5ccb3d3/EnergyEfficiencyIndicatorsforPublicElectricityProductionfromFossilFuels.pdf
2. Rahman, M. W., Abedin, M. Z., & Chowdhury, M. S. (2023). Efficiency Analysis of Nuclear Power Plants: A Comprehensive Review. *World Journal of Advanced Research and Reviews*, *19* (2), 527–540. https://doi.org/10.30574/wjarr.2023.19.2.1553
3. Council of European Energy Regulators (CEER). (2025). *3rd CEER Report on Power Losses*. Available at: https://www.ceer.eu/wp-content/uploads/2025/02/3rd-CEER-Report-on-Power-Losses.pdf
4. Van Der Schoor, T., & Scholtens, B. (2015). Power to the People: Local Community Initiatives and the Transition to Sustainable Energy. *Renewable and Sustainable Energy Reviews*, *43*, 666–675.
5. Gancheva, M., O'Brien, S., Crook, N., & Monteiro, C. (2018). *Models of Local Energy Ownership and the Role of Local Energy Communities in Energy Transition in Europe.* European Committee of the Regions. QG-01-18-933-EN-N; DOI:10.2863/603673

6. European Parliament and Council. (2019). *Directive (EU) 2019/944 of the European Parliament and of the Council of 5 June 2019 on common rules for the internal market for electricity and amending Directive 2012/27/EU.* Official Journal of the European Union, 158, 125–199.
7. European Parliament and Council. (2018). *Directive (EU) 2018/2001 of the European Parliament and of the Council of 11 December 2018 on the promotion of the use of energy from renewable sources.* Official Journal of the European Union, 128, 83–206.
8. Roberts, J. (2020). Power to the People? Implications of the Clean Energy Package for the Role of Community Ownership in Europe's Energy Transition. *Review of European, Comparative & International Environmental Law*, *29* (2), 232–244. https://doi.org/10.1111/reel.12346
9. Ahmed, S., Ali, A., & D'angola, A. (2024). A Review of Renewable Energy Communities: Concepts, Scope, Progress, Challenges, and Recommendations. *Sustainability*, *16* (5), 1749. https://doi.org/10.3390/su16051749
10. Bashi, M. H., De Tommasi, L., Le Cam, A., Relaño, L. S., Lyons, P., Mundó, J., ... & Stancioff, C. E. (2023). A Review and Mapping Exercise of Energy Community Regulatory Challenges in European Member States Based on a Survey of Collective Energy Actors. *Renewable and Sustainable Energy Reviews*, *172*, 113055. https://doi.org/10.1016/j.rser.2022.113055
11. Bauwens, T., Schraven, D., Drewing, E., Radtke, J., Holstenkamp, L., Gotchev, B., & Yildiz, Ö. (2022). Conceptualizing Community in Energy Systems: A Systematic Review of 183 Definitions. *Renewable and Sustainable Energy Reviews, 156*, 111999. https://doi.org/10.1016/j.rser.2021.111999
12. de São José, D., Faria, P., & Vale, Z. (2021). Smart Energy Community: A Systematic Review with Metanalysis. *Energy Strategy Reviews*, *36*, 100678. https://doi.org/10.1016/j.esr.2021.100678
13. Lode, M. L., Heuninckx, S., Te Boveldt, G., Macharis, C., & Coosemans, T. (2022). Designing Successful Energy Communities: A comparison of Seven Pilots in Europe Applying the Multi-Actor Multi-Criteria Analysis. *Energy Research & Social Science*, *90*, 102671. https://doi.org/10.1016/j.erss.2022.102671
14. Hobbs, B. F. (1995). Optimization Methods for Electric Utility Resource Planning. *European Journal of Operational Research*, *83* (1), 1–20. https://doi.org/10.1016/0377-2217(94)00190-N
15. Carroll, P., Flynn, D., Fortz, B., & Melhorn, A. (2017). Sub-hour unit commitment MILP model with benchmark problem instances. In *Computational Science and Its Applications–ICCSA 2017: 17th International Conference, Proceedings, Part II 17* (pp. 635–651). 3–6 July 2017, Trieste, Italy. https://doi.org/10.1007/978-3-319-62395-5_44
16. Bertsimas, D., Litvinov, E., Sun, X. A., Zhao, J., & Zheng, T. (2012). Adaptive Robust Optimization for the Security Constrained Unit Commitment Problem. *IEEE Transactions on Power Systems*, *28*(1), 52–63. https://doi.org/10.1109/TPWRS.2012.2205021
17. Doumen, S. C., Nguyen, P., & Kok, K. (2022). Challenges for Large-Scale Local Electricity Market Implementation Reviewed from the Stakeholder Perspective. *Renewable and Sustainable Energy Reviews*, *165*, 112569. https://doi.org/10.1016/j.rser.2022.112569
18. Gržanić, M., Capuder, T., Zhang, N., & Huang, W. (2022). Prosumers as Active Market Participants: A Systematic Review of Evolution of Opportunities, Models and Challenges. *Renewable and Sustainable Energy Reviews*, *154*, 111859. https://doi.org/10.1016/j.rser.2021.11185
19. Parra-Dominguez, J., Sánchez, E., & Ordóñez, Á. (2023). The Prosumer: A Systematic Review of the New Paradigm in Energy and Sustainable Development. *Sustainability*, *15* (13), 10552. https://doi.org/10.3390/su151310552

20. Ertz, M., Maravilla, J. M. B., & Cao, X. (2025). Prosumer: A New Approach to Conceptualisation. *Journal of Innovation & Knowledge*, *10* (1), 100653. https://doi.org/10.1016/j.jik.2025.100653
21. Frieden, D., Tuerk, A., Neumann, C., d'Herbemont, S., Roberts, J., Gubina, A., ... & Rónai, B. (2020). Collective Self-consumption and Energy Communities: Trends and Challenges in the Transposition of the EU Framework. REScoop.eu. Available at: https://www.rescoop.eu/uploads/rescoop/downloads/Collective-self-consumption-and-energy-communities.-Trends-and-challenges-in-the-transposition-of-the-EU-framework.pdf
22. Gjorgievski, V. Z., Cundeva, S., Markovska, N., & Georghiou, G. E. (2022). Virtual Net-Billing: A Fair Energy Sharing Method for Collective Self-consumption. *Energy*, *254*, 124246. https://doi.org/10.1016/j.energy.2022.124246
23. Gorbatcheva, A., Watson, N., Schneiders, A., Shipworth, D., & Fell, M. J. (2024). Defining Characteristics of Peer-to-Peer Energy Trading, Transactive Energy, and Community Self-consumption: A Review of Literature and Expert Perspectives. *Renewable and Sustainable Energy Reviews*, *202*, 114672. https://doi.org/10.1016/j.rser.2024.114672
24. Alguacil, N., Motto, A. L., & Conejo, A. J. (2003). Transmission Expansion Planning: A Mixed-Integer LP Approach. *IEEE Transactions on Power Systems*, *18* (3), 1070–1077. https://doi.org/10.1109/TPWRS.2003.814891
25. Sousa, T., Soares, T., Pinson, P., Moret, F., Baroche, T., & Sorin, E. (2019). Peer-to-Peer and Community-Based Markets: A Comprehensive Review. *Renewable and Sustainable Energy Reviews*, *104*, 367–378. https://doi.org/10.1016/j.rser.2019.01.036
26. European Union. (2024). Regulation (EU) 2024/1747 of the European Parliament and of the Council of 13 June 2024 amending Regulations (EU) 2019/942 and (EU) 2019/943 as regards improving the Union's electricity market design. Official Journal of the European Union, 174, 13.6.2024, 1–164.
27. Lechl, M., Fürmann, T., de Meer, H., & Weidlich, A. (2023). A Review of Models for Energy System Flexibility Requirements and Potentials Using the New FLEXBLOX Taxonomy. *Renewable and Sustainable Energy Reviews,* 184, 113570. https://doi.org/10.1016/j.rser.2023.113570
28. Degefa, M. Z., Sperstad, I. B., & Sæle, H. (2021). Comprehensive Classifications and Characterizations of Power System Flexibility Resources. *Electric Power Systems Research*, *194*, 107022. https://doi.org/10.1016/j.epsr.2021.107022
29. Universal Smart Energy Framework (USEF). (2019). Energy and Flexibility Services for Citizens Energy Communities: White Paper. Available at: https://www.usef.energy/app/uploads/2019/02/USEF-White-Paper-Energy-and-Flexibility-Services-for-Citizens-Energy-Communities-final-CM.pdf
30. European Parliament and Council. *Directive (EU) 2023/1791 of the European Parliament and of the Council of 13 September 2023 on energy efficiency and amending Regulation (EU) 2023/955 (recast)*. Official Journal of the European Union, L 231, 1–111.
31. Jordehi, A. R. (2019). Optimisation of Demand Response in Electric Power Systems, a Review. *Renewable and Sustainable Energy Reviews*, *103*, 308–319. https://doi.org/10.1016/j.rser.2018.12.054
32. Sangaré, M., Bourreau, E., Fortz, B., Pachurka, A., & Poss, M. (2023). Loads Scheduling for Demand Response in Energy Communities. *Computers & Operations Research*, *160*, 106358. https://doi.org/10.1016/j.cor.2023.106358
33. Korõtko, T., Plaum, F., Häring, T., Mutule, A., Lazdins, R., Borščevskis, O., ... & Carroll, P. (2023). Assessment of Power System Asset Dispatch under Different Local Energy Community Business Models. *Energies*, *16* (8), 3476. https://doi.org/10.3390/en16083476
34. Anuradha, K. B. J., Iria, J., & Mediwaththe, C. P. (2024). Multi-objective planning of Community Energy Storage Systems under Uncertainty. *Electric Power Systems Research*, *230*, 110286. https://doi.org/10.1016/j.epsr.2024.110286

35. Gruber, L., Bachhiesl, U., & Wogrin, S. (2021). The Current State of Research on Energy Communities. *Elektrotech. Informationstechnik*, *138* (8), 515–524. https://doi.org/10.1007/s00502-021-00943-9
36. Deng, L., Zhang, X., Yang, T., Sun, H., Fu, Y., Guo, Q., & Oren, S. S. (2024). Energy Management of Price-Maker Community Energy Storage by Stochastic Dynamic Programming. *CSEE Journal of Power and Energy Systems*, *10* (2), 492–503. https://doi.org/10.17775/CSEEJPES.2023.02720
37. García Muñoz, F., Teng, F., Junyent-Ferré, A., Díaz-González, F., & Corchero, C. (2022). Stochastic Optimization-Based Community Energy Trading Approach to Offer Reactive Power from Distributed Energy Resources for Ancillary Services Market. *SSRN 4145640.* http://dx.doi.org/10.2139/ssrn.4145640
38. Bertsimas, D., & Sim, M. (2004). The Price of Robustness. *Operations Research*, *52* (1), 35–53. https://doi.org/10.1287/opre.1030.0065
39. Scott, I. J., Botterud, A., Carvalho, P. M., & Silva, C. A. S. (2020). Renewable Energy Support Policy Evaluation: The Role of Long-Term Uncertainty in Market Modelling. *Applied Energy*, *278*, 115643. https://doi.org/10.1016/j.apenergy.2020.115643
40. Gazheli, A., & van den Bergh, J. (2018). Real Options Analysis of Investment in Solar vs. Wind Energy: Diversification Strategies under Uncertain Prices and Costs. *Renewable and Sustainable Energy Reviews*, *82*, 2693–2704. https://doi.org/10.1016/j.rser.2017.09.096
41. Kitzing, L., Juul, N., Drud, M., & Boomsma, T. K. (2017). A Real Options Approach to Analyse Wind Energy Investments under Different Support Schemes. *Applied Energy*, *188*, 83–96. https://doi.org/10.1016/j.apenergy.2016.11.104
42. Mutule, A., Borscevskis, O., Astapov, V., Antoskova, I., Carroll, P., & Kairisa, E. (2025). PV Energy Communities in Residential Apartments: Technical Capacities and Economic Viability. *Sustainability*, *17* (7), 2901. https://doi.org/10.3390/su17072901
43. Velásquez, C., Watts, D., Rudnick, H., & Bustos, C. (2016). A Framework for Transmission Expansion Planning: A Complex Problem Clouded by Uncertainty. *IEEE Power and Energy Magazine,* 14 (4), 20–29. https://doi.org/10.1109/MPE.2016.2547278
44. Bessa, R., Moreira, C., Silva, B., & Matos, M. (2019). Handling Renewable Energy Variability and Uncertainty in Power System Operation. *Advances in Energy Systems: The Large-scale Renewable Energy Integration Challenge*, 1–26. https://doi.org/10.1002/9781119508311.ch1
45. Hu, B., Pan, C., Shao, C., Xie, K., Niu, T., Li, C., & Peng, L. (2021). Decision-Dependent Uncertainty Modeling in Power System Operational Reliability Evaluations. *IEEE Transactions on Power Systems*, *36* (6), 5708–5721. https://doi.org/10.1109/TPWRS.2021.3081765

sciendo

LATVIAN JOURNAL OF PHYSICS
AND TECHNICAL SCIENCES
2025, N 3

DOI: 10.2478/lpts-2025-0022

MULTI-APARTMENT BUILDING ELECTRICITY CONSUMERS IN THE FRAMEWORK OF ENERGY COMMUNITIES

M. Auders*, I. Geipele, S. Lapuke

Riga Technical University,
6a Kipsala Str., Riga, LV-1048, LATVIA
*e-mail: martins.auders@rtu.edu.lv

This study investigates the role of electricity consumers in multi-apartment residential buildings, specifically condominiums, within the framework of energy communities in Latvia. With the European Union (EU) aiming for climate neutrality by 2050, energy communities are pivotal in promoting renewable energy. The study examines current electricity supply models in Latvia, analysing whether they allow residents to become active customers, engage in collective self-consumption, or join energy communities. The findings reveal that existing regulatory and infrastructural limitations restrict the participation of many apartment residents in the electricity market. The study suggests legal amendments to enable more inclusive engagement of apartment owners and communities, promoting energy self-sufficiency and supporting the EU climate targets.

Keywords: *Energy community, legal framework, renewable energy.*

1. INTRODUCTION

The European Union (EU) has set targets for achieving climate neutrality by 2050 and reducing dependence on fossil fuels. In the context of the targets set, energy communities are seen as one of the key elements in achieving the EU's energy transition: by 2050, half of Europe's population could produce up to half of the EU's renewable energy [1].

Energy communities (ECs) are also a means of restructuring the energy system, as they will enable citizens to play an active role in the energy transition, bringing them direct benefits, such as increasing energy efficiency, reducing electricity bills, reducing carbon emissions, supporting the local economy, and creating local job opportunities [2].

In accordance with Directive (EU) 2019/944 of the European Parliament and of the Council on common rules for the

internal market for electricity and amending Directive 2012/27/EU (Directive (EU) 2019/944) [3], participation in a citizen EC is open and voluntary, its members or shareholders may be natural persons, local authorities, including municipalities, or small enterprises.

Given that the participation of citizens in ECs is voluntary, the issue of the motivation of citizens to join energy communities is relevant. To date, several studies have been carried out that considered the factors that could influence the involvement of citizens in energy communities. As it is indicated in the literature, the population always has certain motives: these motives are heterogeneous and complex [4]. Other authors point out various factors that influence the motivation of citizens to accept renewable energy projects, such as financial and environmental factors, self-sufficiency, factors of uncertainty and trust, level of inconvenience, impact on residence, as well as different views of citizens. These factors are also linked to concerns about energy self-sufficiency [6], participation in the community's energy transition [7], energy efficiency and the development of a renewable energy production system [8], as well as opportunities to own renewable energy projects, which would include direct involvement – responsibility for aspects of renewable energy projects and direct involvement in the project planning process [9]. The simplicity of participation is also mentioned as a significant factor.

Similarly, in the context of the participation of citizens in energy communities without factors related to motivation, the existence of preconditions for a resident of an apartment building to become, for example, an active customer or a member of EC is no less important. This would make the energy consumer more self-sufficient, more energy independent and contribute to climate neutrality and environmental objectives.

The hypothesis of this study is that not all electricity consumers in multi-apartment residential buildings in Latvia can participate in the electricity market as active users, participants of collective self-consumption or members of ECs.

Within the framework of the study, the following research questions are raised:

- Do electricity supply models that exist in Latvia ensure the status of an active user, a participant in collective self-consumption or a member of the energy community for a person living in multi-apartment residential building as an energy consumer?
- Can the community of apartment owners, as a legal entity uniting all apartment owners of an apartment building (communities of apartment owners), participate in the electricity market?

As part of the study, the following tasks are performed:

- the status of a person living in multi-apartment residential buildings as an energy consumer has been investigated depending on the electricity supply model and the connection of such a status with the status of an active user, collective self-consumption participant or member of the energy community;
- the prerequisites have been identified so that an apartment owner community may operate in the electricity market.

The study is based on the literature review method, using both scientific literature and regulatory enactments of the EU and the Republic of Latvia. During the research process, the authors used generally accepted qualitative methods – analysis, synthesis and logically constructive and comparative methods.

2. STATUS OF A PERSON LIVING IN AN APARTMENT BUILDING AS AN ENERGY CONSUMER

The types of activities to be performed in the electricity market in Latvia, which include the production of electricity, transmission of electricity, distribution and trade of electricity, are regulated by the Electricity Market Law [10]. Regulatory enactments distinguish the following statuses of electricity consumers:

- energy user – a natural or legal person who buys and consumes a particular type of energy or fuel from energy supply merchants for his or her own needs or uses it in energy supply or other type of commercial activity [11];
- final customer – an energy customer who purchases energy for use for his own needs (final consumption) in commercial activities [11];
- sub-user – a person who, upon agreement with the user, uses the electricity grids owned or possessed by him or her to receive electricity and does not purchase electricity from a trader or system operator [12].

Thus, the energy user is a broader concept than the term "final customer" and includes the right not only to consume energy for its own purposes, but also to use it for energy supply or use it on other commercial activities. On the other hand, the sub-user differs from the final customer or energy user as the sub-user does not purchase electricity directly from the trader through networks belonging to the system operator because he or she uses networks belonging to the energy user to receive electricity.

At the same time, it is important that the status of the final customer or sub-user within the meaning of regulatory enactments is not linked to the ownership rights of the apartment, which means that both the owner of the apartment and the tenant may be the final or sub-users of energy. In turn, the status of a person living in an apartment building (owner of an apartment or tenant of an apartment) as an energy consumer depends on the boundary of ownership to electrical installations, up to which electricity is supplied to the electricity user [10].

There are two models of electricity supply in Latvia, observing electricity accounting, as well as the boundary of ownership to electrical installations.

- Electricity is supplied to each owner (or tenant) of apartments in an apartment building and is accounted for with a meter for commercial accounting of electricity, which is installed on the boundary of ownership to electrical installations. Separately, the electricity consumed for the common use of a residential building is also accounted for by means of a commercial electricity meter. In such a model, the owner (or tenant) of an apartment building has the status of an end user. This model also includes cases where a commercial meter is installed not on the boundary of ownership of the distribution system operator, but already beyond it. However, in these cases, the consumer is the end-user.
- All electricity supplied to one or more apartment buildings is accounted for by a common meter for commercial electricity accounting. The amount of electricity consumed in apartments and residential buildings for the purposes of sharing is determined by using commercial electricity meters. In such a model,

the owner (or tenant) of apartments in an apartment building has the status of a sub-user, while the energy user status in most cases lies with the manager of the apartment building.

The electricity supply model, in which the owner (or tenant) of apartments in an apartment building has the status of a sub-user, can be created in already built apartment buildings, if a written consent of the owners of the apartment building and all users in the building to terminate contractual obligations with the system operator has been received. Also, due to the reduced costs associated with the creation of electricity connections, such a model is created by up to two-thirds of the newly built apartment buildings and exists in about 500 objects [13]. At the same time, both the Ministry of Economics and the Ministry of Climate and Energy, which is responsible for the energy sector, have agreed that such a model is undesirable and, in the future, only the construction of apartment buildings in which electricity would be supplied to each owner (tenant) of apartments in an apartment building would be allowed as a final customer. This is because the sub-user cannot choose an electricity trader. Thus, in a situation where all residents of one or even several apartment buildings have the status of a sub-user, they will all have one electricity trader and one tariff plan that will not meet the needs and peculiarities of consumption of each resident. Considering the findings, the authors of the study conclude that it is necessary to develop amendments to Cabinet Regulation No. 693 of 19 October 2021 "Construction Standard for General Requirements for Structures LBN 200-21" by imposing such requirements for electricity connections and commercial accounting in order to ensure that apartment owners in all newly built houses have the status of an end user.

3. STATUS OF THE COMMUNITY OF APARTMENT OWNERS AS AN ENERGY CONSUMER

In addition to the energy consumed in the apartments, electricity is also consumed in the multi-apartment residential buildings for common use purposes – lighting of common areas, elevator, circulation pumps, etc. In the model, when the electricity supplied to one or more apartment buildings is accounted for by a common meter for commercial accounting of electricity, the energy user is the manager of the apartment building. As already mentioned above, electricity consumed in each apartment as well as in shared premises is determined by control meters. However, also in the model when electricity is supplied to each apartment owner (tenant) of a multi-apartment residential building and it is accounted for by a meter for the commercial accounting of electricity, the manager, who accordingly has the status of electricity user, shall enter a contract for the supply of electricity consumed for the purposes of sharing.

However, in accordance with the laws and regulations governing the management of residential buildings, the manager should act as a representative of the community of apartment owners and not become a user of electricity. In accordance with the Law on Administration of Residential Houses [14], one of the mandatory management activities is the provision of electricity to the part of the residential house in common ownership (also to ensure the operation of equipment under joint ownership). The Senate

of the Supreme Court has clarified [15] that the provision of utilities, also electricity, is understood not by the supply of a service, but the drawing up of a service contract. Also, the Senate of the Supreme Court has stated that the manager of a residential house must take all necessary actions to comply with the service provider on the conclusion of the above-mentioned contract, including organising in the apartment property house the decision of the community of apartment owners on the conclusion of the contract, contacting the provider and discussing with it the terms of the contract. Also, having previously assessed the role of the community of apartment owners and the manager in utility contracts, the Senate of the Supreme Court [16] pointed out that the Law on Administration of Residential Houses and the Law on Residential Properties create the concept sufficiently clear that all apartment owners together are the owner of a residential house, who is directly the legally entitled party to the contracts, as well as that the manager is a trustee by law, and not independently assumes obligations for himself.

With regard to the legal capacity of the community of apartment owners, the judgment of the Senate of the Supreme Court of 12 December 2019 in case SKC-109/2019, by which it was recognised that the community of apartment owners is a special type of legal entity that is able to acquire property, enter into obligations and be a defendant or plaintiff in court [17]. Recognition of the legal capacity of the community of apartment owners means that the totality of the owners of a residential house is primarily viewed as a special type of society endowed with legal capacity, and not as joint owners within the meaning of the Civil Law [18].

Recognising the communities of apartment owners as a legal entity, the Senate of the Supreme Court, in its judgment in case SKC-109/2019, stated that the status of the community as a legal entity makes it possible to separate the ownership of these funds from the funds belonging to the individual apartment owners and to dispose of those funds in order to achieve the objective of the community, namely the long-term [19] management of the apartment building. The concept of community of apartment owners as a special type of society endowed with legal capacity forms the framework for solving legal relations between apartment owners and plays an important role in clarifying the content of legal relations between the community of apartment owners and third parties, including the manager [19].

However, despite the case law of the Senate of the Supreme Court, as well as the fact that the findings contained in the judgment of case SKC-109/2019 were codified in the Law on Residential Properties [18], electricity traders do not enter into agreements with communities of apartment owners because electricity traders either "do not see" or "do not want to see" as counterparties.

However, the Senate of the Supreme Court explained in the judgment in SKC-109/2019 that the community of apartment owners is a special type (*sui generis*) legal entity – a company that does not fully correspond to one of the types of legal entities already recognised in the Latvian Civil Law. At the same time, the community of apartment owners has similar features to such types of legal entities as associations and capital companies [19]. However, in practice, electricity traders enter into contracts either with natural persons or legal entities. Although the community of apartment owners is the same legal fiction as a legal entity, the community of apartment owners differs from a legal entity in that it does not have a registration number, and also its representative may not be indicated in the public register.

To address the issue of assigning an identifier to communities of apartment owners and indicating this identifier, as well as a representative in a public register, the Ministry of Economics is currently drafting amendments to the Law on Residential Properties. The adoption of this bill would create prerequisites for the correct resolution of mutual legal relations between the community of apartment owners as an energy user and an electricity trader.

4. APARTMENT OWNERS AND THE COMMUNITY OF APARTMENT OWNERS AS AN ACTIVE USER, PARTICIPANT IN COLLECTIVE SELF-CONSUMPTION OR A MEMBER OF AN ENERGY COMMUNITY

According to the EU legislation, the following models related to decentralised energy exchange can be distinguished: individual self-consumption, collective self-consumption, peer-to-peer trading, energy communities [9].

In the case of individual self-consumption, the final customer who uses the self-generated electricity for self-consumption and transfers or sells the electricity that is not immediately consumed (surplus) to the electricity trader has the status of an active customer [10]. As a result, the status of the active user is linked to that of the end-user.

The owner (or tenant) of an apartment may be an active user in cases when the electricity consumed in the apartment is accounted for with a meter for commercial accounting of electricity. However, because the common elements of a residential building belong to the part in common ownership [20], in order, for example, to place electricity production equipment on the facade or roof of a house, apartment owners need the consent of the community of apartment owners. In turn, the placement of electricity production equipment in a separate property is problematic; therefore, the most common case will be if the active user will have several objects. Moreover, electricity will be produced at another object, while consumed in an apartment because the Electricity Market Law also allows consumption of the active user in several objects of the active user as self-consumption of the active user [10].

In the electricity metering model, when all electricity supplied to a residential building is accounted for with one commercial meter, the owner (tenant) of the apartment has the status of a sub-user; therefore, the owner of the apartment cannot become an active user. In this model, the manager who enters into a contract for the provision of electricity to one or several apartment buildings also has the status of a user. Thus, the manager as a user does not comply with the status of an active customer specified in the Electricity Market Law. In such a model, the owner (tenant) of the apartment, due to the absence of the status of the final customer, cannot also engage in collective self-consumption, or become a member of the energy community.

Apart from the case when the produced electricity is consumed in several objects of an active customer, the Electricity Market Law also defines the consumption of the produced electricity in the objects of active customers acting jointly or at the objects of the members of the energy community as self-consumption of the active customer [10]. Thus, it can be seen from the definition of the law that the self-consumption of an active customer includes the consumption of electricity both within collective

self-consumption and within energy communities, without distinguishing between these two models related to decentralized energy exchange.

As pointed out in the scientific literature, the main feature of collective self-consumption schemes is that their functioning exists independently of the specific organisational and market aspects, and whenever two or more customers come together to generate and consume electricity themselves, a collective self-consumption scheme is formed regardless of the nature of the legal relationship that distinguishes it from energy communities based on in specific types of legal relations [9]. At the level of the European Union Directives, too, a distinction has been made between collective self-consumption and energy communities. First, as opposed to collaborative active customers (collective self-consumption), Directive (EU) 2019/944 defines a citizen energy community as a legal entity [3]. Second, it follows from Directive (EU) 2018/2001 of the European Parliament and of the Council on the promotion of the use of energy from renewable sources that shared renewable energy must be produced through production units owned by the renewable energy community [20]. Consequently, the European Union directives provide that the energy produced by production units belonging to the energy community is to be owned by the energy community, whereas the fifth paragraph of article 377 of the Electricity Market Law provides that the electricity produced by a member of an electricity energy community is the property of the energy community [10]. At the same time, however, it is not clear how the regulation of the Electricity Market Law ensures the fulfilment of the conditions contained in Directive (EU) 2019/944 of the European Parliament and of the Council that members or shareholders of a citizen energy community do not lose their rights and obligations as household customers or active customers.

Section 37 of the Electricity Market Law Article 6 describes two cases of collective self-consumption [10]:

- in accordance with the requirements of the law, two or more final customers in the same building or in one other type of immovable property may act jointly and become active customers of electricity from renewable energy sources;
- jointly acting active customers of electricity from renewable energy sources shall be a legally compliant group of at least two final customers.

This means that currently, within the framework of collective self-consumption, it is possible to become active users of electricity, apartment owners, one of whom generates electricity in another object that is not located in a residential house, for example, in a summer cottage, but the generated electricity is consumed by the other apartment owners. However, the most appropriate model for a single apartment building would be if the community of apartment owners were recognised as an active user. This, in the case described in the Electricity Market Law, would allow the owners of apartments in one house to consume, within the framework of collective self-consumption, electricity produced by equipment that is located in the part of the residential house under common ownership – on roofs, facades and in the land plot, i.e., the condition is fulfilled that at least one final customer (community of apartment owners) has installed electricity production equipment in which only renewable ones are used for the production of electricity energy resources and also used by other final customers.

In accordance with the provisions of the Electricity Market Law, members or share-

holders of the electricity energy community are final customers and active customers whose objects are connected to the system of one system operator. Thus, in the case of an energy community, the owner (tenant) of an apartment needs the status of a final customer to become a member of the energy community, and a sub-user cannot become a member of the energy community. Similarly, the community of apartment owners could also become a member of the energy community if its status as a user is recognised.

5. CONCLUSIONS AND PROPOSALS

A prerequisite for the status of an end-user is a prerequisite for a resident of an apartment building to become an active customer, a participant in collective self-consumption, or a member of an energy community. Of the two electricity supply models existing in Latvia, only the model, when the electricity consumed by each owner of the apartment of an apartment building is accounted for with a meter for commercial accounting of electricity registered by the system operator, ensures the involvement of inhabitants in energy communities. On the other hand, in a model where all electricity supplied to a multi-apartment residential house is accounted for by a common meter for commercial accounting of electricity, but the amount of electricity consumed in an apartment is determined by control meters, residents of an apartment building as sub-users not only cannot choose an electricity trader, but also become active customers or members of the energy community. Although sub-users, exercising the rights of apartment owners, can decide on the installation of electricity production equipment in the residential house they own and consume the generated electricity, thus essentially becoming a participant in collective self-consumption. However, such a collective self-consumption scheme is not recognized in the Electricity Market Law and a person, usually the manager, who has entered into a contract for the supply of electricity to the relevant residential house will be considered as the user of electricity and the owner of the electricity produced in the residential house. A solution to such a situation could be the installation of commercial metering devices not on the boundary of ownership of the distribution system operator, but beyond it. Such a solution already exists in practice; therefore, it would be necessary to regulate in regulatory enactments only the prerequisites for this type of accounting solution, if it is requested by sub-users.

The authors note that an additional problem is related to the conclusion of contracts for the electricity supplied to an apartment building for sharing purposes. In practice, the situation where contracts for the provision of electricity for common purposes are entered into by the manager is contrary to the regulation contained in the Law on Administration of Residential Houses and the Law on Residential Properties. Consequently, amendments to the Law on Residential Properties are required, which would allow electricity traders to conclude contracts with the community of apartment owners. Such a case would not only streamline the legal relationship between the parties involved in the management of residential buildings but would also allow apartment owners to become energetically self-sufficient through the community of apartment owners, reap economic benefits, as well as contribute to the achievement of climate neutrality objectives.

REFERENCES

1. European Commission. (2024, June 2). *Communication from the Commission to the European Parliament, the Council, the European Economic and Social Committee and the Committee of the regions: Securing our future Europe's 2040 climate target and path to climate neutrality by 2050 building a sustainable, just and prosperous society*. (Report COM/2024/63 final) https://eur-lex.europa.eu/legal-content/EN/TXT/?uri=celex:52024DC0063
2. Sarcina, A., & Canesi, R. (2023). Renewable Energy Community: Opportunities and Threats towards Green Transition. *Sustainability*, *15* (18), 13860. https://doi.org/10.3390/su151813860
3. Directive 2019/944. *Directive (EU) 2019/944 of the European Parliament and of the Council of 5 June 2019 on common rules for the internal market for electricity and amending Directive 2012/27/EU (recast) (Text with EEA relevance.)*. https://eur-lex.europa.eu/eli/dir/2019/944/oj/eng
4. De Franco, A., Venco, E., De Lotto, R., Pietra, C., Kutzner, F., Bielig, M., & Vogel, M. (2023). Drivers, Motivations, and Barriers in the Creation of Energy Communities: Insights from the City of Segrate, Italy. *Energies*, *16* (16), 5872. https://doi.org/10.3390/en16165872
5. Balcombe, P., Rigby, D., & Azapagic, A. (2014). Investigating the Importance of Motivations and Barriers Related to Microgeneration Uptake in the UK. *Applied Energy, 130*, 403–418. https://doi.org/10.1016/j.apenergy.2014.05.047
6. Soeiro, S., & Dias, M. F. (2020). Renewable Energy Community and the European Energy Market: Main Motivations. *Heliyon, 6* (7). https://doi.org/10.1016/j.heliyon.2020.e04511
7. Koltunov, M., Cittati V.-M., & Bisello A. (2022). Institutional and Policy Context of Energy Communities in France and Italy: How to Increase the Welfare-Enhancing Capacity of the Sector. *Energy Communities*, 341–361. https://doi.org/10.1016/B978-0-323-91135-1.00007-9
8. Bashi, M. H., Tommasi, L., Le Cam, A., Relano, L. S., Lyons, P., Mundo, J., … & Stancioff, C. E. (2023). A Review and Mapping Exercise of Energy Community Regulatory Challenges in European Member States Based on a Survey of Collective Energy Actors. *Renewable and Sustainable Energy Reviews*, *172*. https://doi.org/10.1016/j.rser.2022.113055
9. De Almeida, L., Cappelli, V., Klausmann, N., van Soest, H. (2021). Peer-to-Peer Trading and Energy Community in the Electricity Market – Analysing the Literature on Law and Regulation and Looking Ahead to Future Challenges. EUI RSC, 2021/35, Florence School of Regulation. https://hdl.handle.net/1814/70457
10. Saeima. (2005). *Electricity Market Law*. Vestnesis. https://likumi.lv/ta/en/en/id/108834
11. Saeima. (1998). *Energy Law*. Vestnesis. https://likumi.lv/ta/en/en/id/49833
12. Cabinet of Ministers. (2023, November 7*). Regulations Regarding the Trade and Use of Electricity.* Vestnesis. https://likumi.lv/ta/id/347235-elektroenergijas-tirdzniecibas-un-lietosanas-noteikumi
13. Ministry of Economics. (2023). *Data of the Ministry of Economics*. Not published.
14. Saeima. (2009). *Law on Administration of Residential Houses.* Vestnesis. https://likumi.lv/ta/id/193573-dzivojamo-maju-parvaldisanas-likums
15. Supreme Court Senate. (2021, April 22). *Judgment of the Senate of the Supreme Court of 22 April 2021 in case SKC-5/2021.*
16. Supreme Court Senate. (2013, December 2). *Judgment of the Senate of the Supreme Court of 2 December 2013 in case SKA-706/2013.*
17. Supreme Court Senate. (2019, December 12). *Judgment of the Senate of the Supreme Court of 12 December 2019 in case SKC-109/2019*.
18. Gulbis, R. (2020). Community of Apartment Owners as a Special Type of Legal Entity. *Lawyer's Name*, *14,* (1124), 11–18.

19. Supreme Court Senate. (2019, December 12). *Judgment of the Senate of the Supreme Court of 12 December 2019 in case SKC-109/2019.*
20. Saeima. (2022). *Amendments to the Law on Residential Properties.* Vestnesis. https://likumi.lv/ta/id/331195-grozijumi-dzivokla-ipasuma-likuma
21. Saeima. (2011). *Law on Residential Properties.* Vestnesis. https://likumi.lv/ta/en/en/id/221382

sciendo

LATVIAN JOURNAL OF PHYSICS
AND TECHNICAL SCIENCES
2025, N 3

DOI: 10.2478/lpts-2025-0023

ZnO-THIN FILM GROWTH PROCESSES: CORRELATION BETWEEN THE STRUCTURAL PROPERTIES OF HYDROCHLORIC ACID (HCl) AND WATER (H_2O) SOLUTION EFFECT USING INNOVATIVE ELECTROSTATIC SPRAY DEPOSITION (ESD) TECHNOLOGY

F. I. Abbas[1,2,3*], M. Sugiyama[1,4]

[1] Department of Electrical Engineering,
Tokyo University of Science,
2641 Yamazaki, Noda, Chiba 278-8510, JAPAN
[2]Department of Theoretical Physics, University of Dhaka,
Dhaka-1000, BANGLADESH
[3] Department of Electrical Engineering,
City University, Savar, Birulia, Dhaka, 1216, BANGLADESH
[4]Research Institute, RIST, Tokyo University of Science,
2641 Yamazaki, Noda-shi, Chiba-ken, 278-8510, JAPAN
*e-mail: fysolibnaabbas1988@gmail.com

This study carefully examined the influence of 0.005 M and 0.015 M HCl on the ZnO growth mechanism, implementing the solution-dependent ESD technique across a temperature range of 300 °C, 400 °C, and 500 °C, respectively. The ESD technique uses zinc chloride ($ZnCl_2$) as a precursor, which is dissolved in ethanol (CH_3CH_2OH) at a concentration of 0.1 M to generate a zinc complex molecule. ESD was used for six distinct prepared solutions on a conductive In_2O_3:Sn (ITiO) coated alkali-free glass substrate in order to explore the impact of varying the water (H_2O) ratio in the spray solution on the HCl. XRD depictions showed that the ZnO nanoparticles had a pristine wurtzite crystal structure. The microstructure properties (MSP) of ZnO thin films were analysed to understand the microlevel changes resulting from the ESD growth mechanism. Specifically, the lattice parameter ratio (c/a), positional parameter (μ), and bond length (L **(Å)**) were assessed. The XRD pattern demonstrated the predominant alignment of the (002) crystal planes in ZnO thin films. This work signifies an important phase in using cost-efficient ESD-deposited semiconductor applications in commercial and industrial uses.

Keywords: *Bond length, ESD, lattice parameter, positional parameter, ZnO growth mechanism.*

1. INTRODUCTION

ZnO is a significant material used in semiconductors and piezoelectric devices. It has a broad energy gap of 3.37 eV and a high exciton binding energy of 60 meV. Due to its distinctive material features and versatile uses in transducers, varistors, transparent conductors, transparent UV protection films, chemical sensors, solar cells, and more, it has garnered significant attention [1], [2]. Several techniques have been devised for the fabrication of ZnO nanostructures, including nanowires [3], nanotubes [4], nanocages between [5], nanoparticles [6], and nanoflowers [7]. ZnO thin films can be developed using many processes. Dry methods, such as sputtering [8] and pulsed laser deposition [9], are commonly utilised. Wet methods, namely chemical bath deposition [10], mist chemical vapor deposition [11], and spray pyrolysis [12], are also employed.

Additionally, this study aims to investigate the ZnO growth mechanism, and the MSP, namely, lattice parameter ratio (c/a), positional parameter (μ), and bond length (L (Å)). Using the novel ESD technology, the study examines both low concentration (0.005 M) and comparatively high HCl concentrations (0.015 M) in the prepared spray solution at three different temperatures: 300 °C, 400 °C, and 500 °C, by varying the H_2O ratio in the precursor solutions. First, ESD approach offers not only user-friendly functionality but also significant industrial advantages, including its capacity to effectively cover extensive regions due to its uncomplicated and easily accessible nature. Second, this method enables deposition without requiring a vacuum, and it offers relatively easy control of the composition ratio and doping. Third, to distribute the solution from the metal nozzle edge in ESD, a DC high voltage is positioned between the nozzle and the conductive substrate. When the flow rate and electric field are adjusted to match the viscosity and resistivity of the solution, the spray shape known as the "cone-jet mode" [13] is illustrated in Fig. 1 (a).

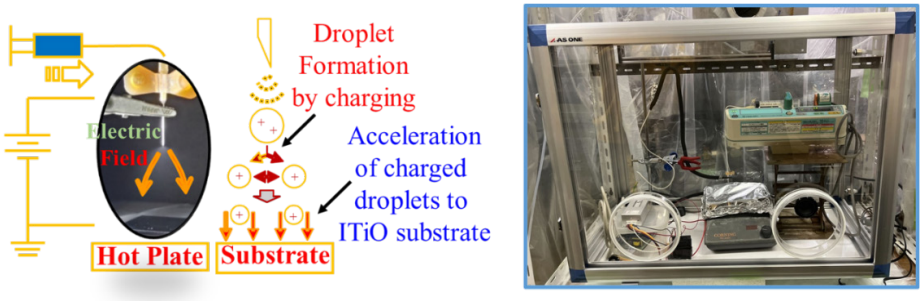

(a). Schematic diagram (b). Experimental setup

Fig. 1. Schematic diagram of ESD.

As the cone-jet mode is used, the droplets that are created are of the same size [14]. Fourth, as a result of the evaporation of the solvent in the droplets, the charge density on the surface of the droplets increases, which results in the droplets automatically splitting apart. Fifth, from a physics point of view, Coulomb forces cause the charged droplets to repel each other, preventing them from colliding. These features allow for creating dense and homogeneous thin films using ESD.

Moreover, few studies have examined the growth mechanism of oxide-based semiconductors deploying the ESD technique [15] and focused on the solution that was selected [16]. This study represents the first step in developing cost-effective and easy-to-use technologies that allow visible light to pass through without obstruction using the novel ESD method for oxide-based semiconductor research studies.

2. EXPERIMENTAL METHODS

The zinc sources used in this study were $ZnCl_2$ (98 % Assay, $ZnCl_2$=136.32), Lot. LEH7398, Mfg. Date. 2021.09, FUJIFILM Wako Pure Chemical Corporation). The solutes were ethanol (CH_3CH_2OH (99.5), Cat. No. 14033-70, FW: 46.07, KANTO CHEMICAL CO, INC) and deionized water (H_2O). ZnO films were deposited using ESD on a conductive In_2O_3:Sn (ITiO) coated alkali-free glass substrate. Figure 1 displays the ESD schematic experimental diagram. For the ESD spray method, 20 ml of six different spray solutions were made by changing the amounts of H_2O and HCl. In order to investigate the growth mechanism of ZnO, eighteen (18) ITiO substrates were used with sizes 7.5 mm × 7.5 mm. The previous work included detailed experimental procedures [16].

X-ray diffraction was used to gain insight into the crystallographic directions of the ZnO films (XRD; Rigaku Ultima IV, Rigaku SmartLab). The analysis of the ZnO thin films of MSP included assessing the ratio of lattice constant parameters, namely the c/a, ratio. Here, 'a' (Å) represents the lattice parameter along the x-axis, while 'c' (Å) represents the lattice parameter along the z-axis. Furthermore, the novel ESD method correlates the lattice positional parameter, μ, which is dimensionless parameter, and lattice bond length, L (Å) with the basic crystal growth mechanism [17], [18]. Below are the mathematical procedures relevant to this estimatio, (1–3) [19]–[21].

$$(c/a) = \left[\frac{\lambda}{sin\theta_{002}} \Big/ \frac{\lambda}{\sqrt{3} sin\theta_{100}} \right]; \quad (1)$$

$$\mu = \frac{a^2}{3c^2} + 0.25; \quad (2)$$

$$L = \left(\frac{a^2}{3c^2} + (0.5 - \mu)^2 * c^2 \right)^{1/2}; \quad (3)$$

where λ, θ, are lambda as the wavelength (1.54 Å), theta as angle (diffraction angle, Bragg's law), beta as angle (in radian), respectively.

3. RESULTS AND DISCUSSION

Equation (1) allows us to obtain the lattice constant ratio, c/a, of the unit cell for the hexagonal wurtzite structure of ZnO. The reported values for the c/a ratio for bulk ZnO are 1.602 [22]. In the previous study, all the samples showed varying values when the HCl concentration was changed with a variation in the H_2O ratio in the ESD spray samples [16]. These samples were tested at temperatures ranging from 300 °C to 500 °C.

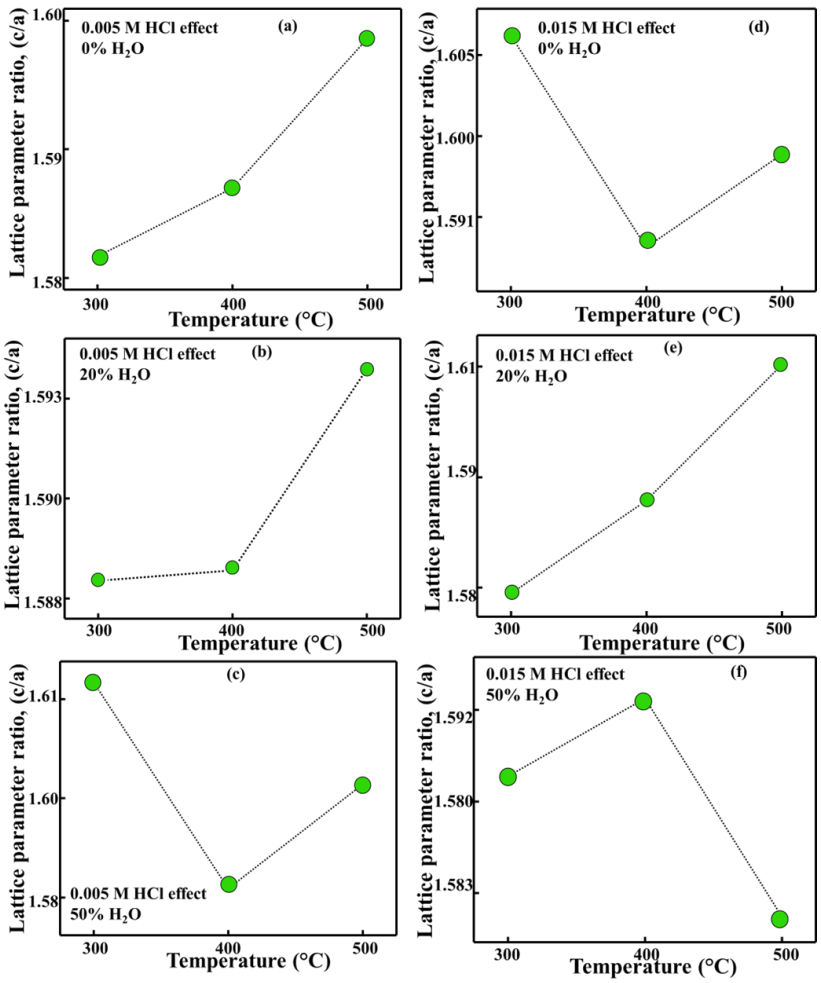

Fig. 2. Lattice parameter ratio, (c/a) of ZnO film according to (a–c) 0.005M HCl, and (d–f) 0.015M HCl weight ratio of H_2O/solvent in the solution deposited by ESD at 300 °C, 400 °C and 500 °C, respectively.

Figure 2 (a–c) and Fig. 2 (d–f) show the c/a results for the ZnO thin film study for the 0.005 M and 0.015 M HCl mixed samples, respectively. Figure 2 (a–b) demonstrates a progressive increase in the c/a ratio between temperatures of 300 °C and 500 °C. On the other hand, Fig. 2(c) shows a decrease in the value of c/a from 300 °C to 400 °C, followed by an increase from 400 °C to 500 °C. Figure 2 (d–f) depicts the results of the 0.015 M HCl mixed ESD spray sample. Figure 2 (d) and Fig. 2 (f) displayed remarkably random behaviours. Besides, 20 % H_20 mixed samples explain the increasing tendency of the c/a value. In comparison, the low-concentration HCl mixed samples showed an expansion in the behaviour of the c/a analysis results. On the other hand, the high concentration ESD samples demonstrate the compression nature of the c/a values. Perhaps, this is a link between the stiffness at the atomic level due to the high concentration (0.015 M) of the HCl component [16], [22].

The study of the positional parameter (μ) in the wurtzite structure measures the amount by which each atom gets displaced with respect to the next, and the value of

m can be calculated using Eq. (2). Figure 3 (a–c) and Fig. 3 (d–f) plot the results of μ, representing the mixed samples of 0.005 M and 0.015 M HCl, respectively. These samples have varying ratios of H_2O, specifically 0 %, 20 %, and 50 %, in the ESD.

Fig. 3 (a) consistently shows a decreasing trend for μ across the entire temperature range from 300 °C to 500 °C. Besides, Fig. 3 (b, c) represents the result of μ for the 20 % and 50 % H_2O ratios in the ESD spray technique. In both figures, in the temperature range from 300 °C to 400 °C, μ starts to increase, then from 400 °C to 500 °C, it decreases. Despite mixing a small amount of HCl, the behaviour of this sample remains highly dynamic. This rapidly evolving technique might enable the development of ZnO thin film technology using a novel electrostatic discharge (ESD) approach.

Figure 3 (d–f) illustrates the reaction of ESD spray solution samples to varying H_2O concentrations in 0.015 M HCl. Figure 3 (d–f) reveals a range of very random features that might be considered unstable in nature for high-concentration ESD samples. In Fig. 3 (d), μ starts to increase from 300 °C to 400 °C, and then it decreases from 400 °C to 500 °C. Fig. 3(e) consistently shows a decreasing trend for μ across the entire temperature range from 300 °C to 500 °C.

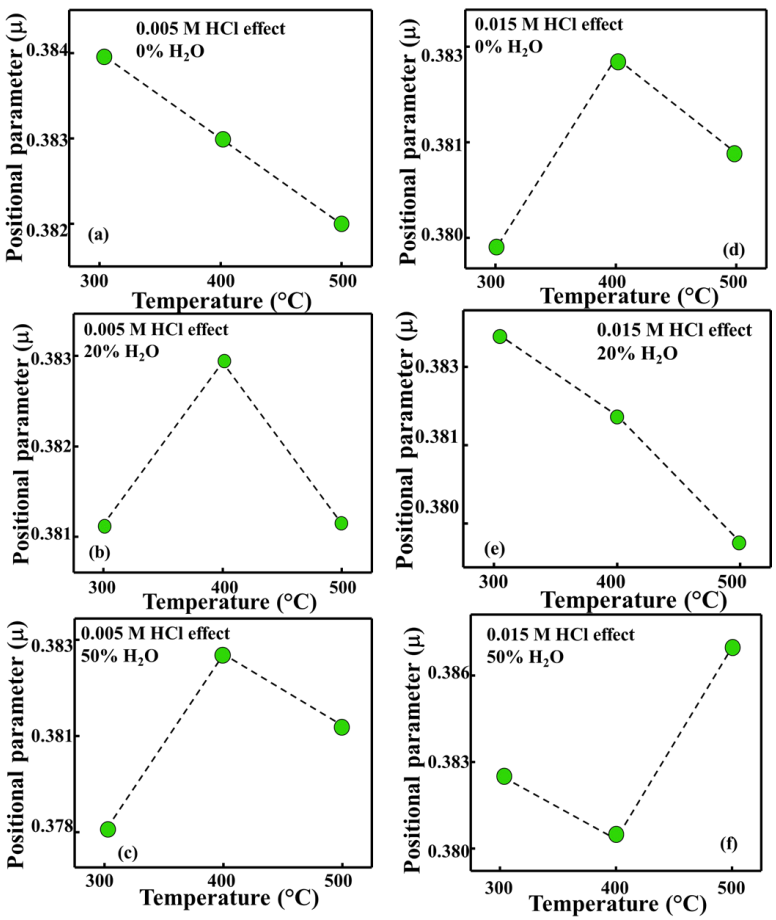

Fig. 3. Lattice positional parameter, (μ) of ZnO film according to (a–c) 0.005M HCl, and (d–f) 0.015M HCl weight ratio of H_2O/solvent in the solution deposited by ESD at 300 °C.

In addition, in Fig. 3(f), μ decreases from 300 °C to 400 °C and then increases from 400 °C to 500 °C. Furthermore, the microlevel atomic positional analysis reveals a subtle consistency in the low concentration of ESD spray samples.

In the wurtzite structure, the bond length, L (Å), is determined by measuring the closest distance between atoms in relation to the neighbouring atom. The value of L (Å) can be determined using Eq. (3). Figure 4 (a–c) and Fig. 4 (d–f) indicate the findings about the lattice bond length, L (Å), of ZnO thin film using ESD technology. In Fig. 4(a, b), L (Å) was found increasing in nature for the studied temperature ranges. However, in Fig. 4 (c), the results decreased. Figure 4 (d–f) showed an increasing value for the 0.015 M HCl results. When comparing the bond length results of HCl solutions with concentrations of 0.005 M and 0.015 M, it was found that the bond lengths were the same for the low concentration HCl mixed sample [17], [18], [22]. This suggests that the low concentration HCl sample stimulates the ZnO thin film growth mechanism through the innovative ESD technology.

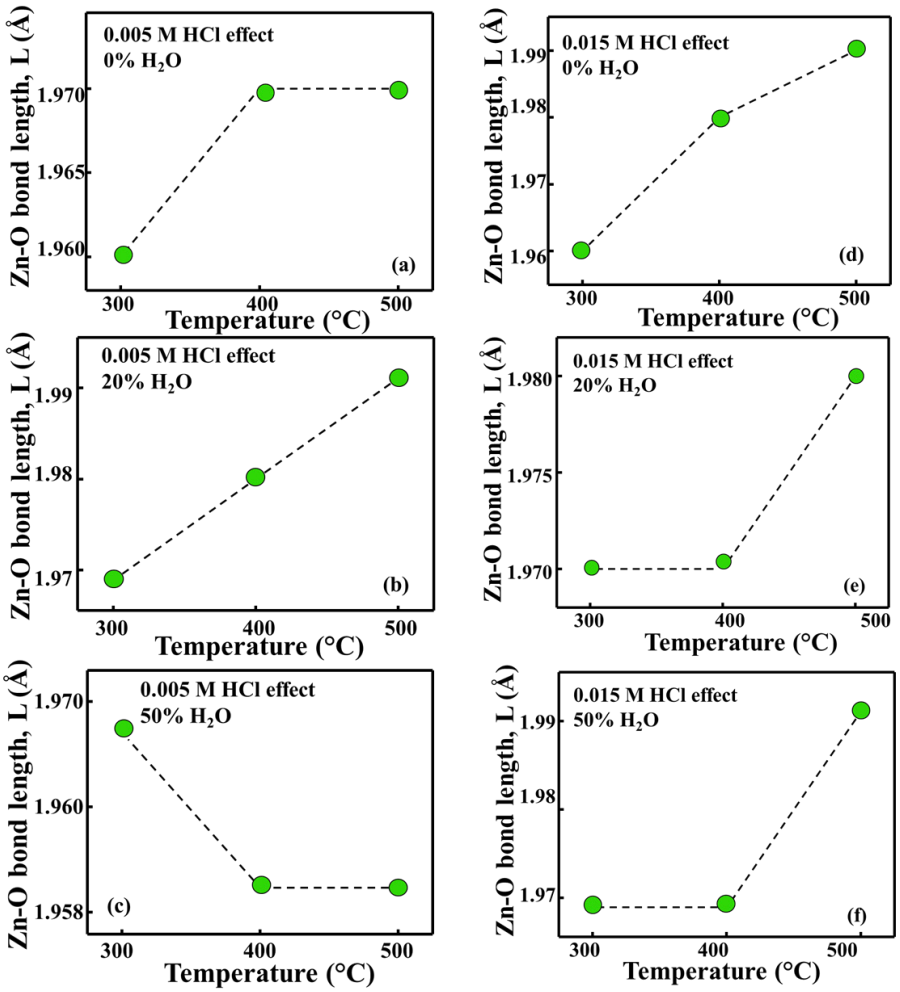

Fig. 4. Lattice bond-length, (L) of ZnO film according to (a–c) 0.005M HCl, and (d–f) 0.015M HCl weight ratio of H_2O/solvent in the solution deposited by ESD at 300 °C, 400 °C and 500 °C.

This study investigated the growth mechanism of ZnO semiconductor thin films by varying the H_2O ratio spray solution in the presence of HCl acid. We carried out the analysis using the ESD method on a conductive In_2O_3:Sn (ITiO)-coated alkali-free glass substrate at temperatures of 300 °C, 400 °C, and 500 °C. The crystal quality of ZnO thin films made with the new ESD technology is not as good as films made with evaporate [9], [10] or moist [22], which are earlier methods. However, XRD reveals that adding a small amount of HCl (0.005 M) significantly improves the growth process of these films with changing the H_2O ratio. When low concentrations of HCl (0.005 M) were mixed with ZnO thin films made using the novel ESD method, the structural parameters, μ, and L (Å) showed satisfactory stability and consistency. From a physical standpoint, this stability is very important for the growth of thin film development with high-quality crystal [22]. In contrast, the high concentrations (0.015 M) of the HCl mixed sample showed complex behaviour compared with low concentration HCl samples by ESD technology. Furthermore, it became clear that this conjugate pair of low-concentration HCl and H2O combinations could enhance the ZnO thin film. However, the results that emerged from the current study on the growth mechanism of ZnO thin films were physically satisfactory, indicating that they might be considered cost-effective. Further investigation on other properties is also needed for clear visualisation on ZnO growth mechanism by the novel ESD technique.

4. CONCLUSIONS

ESD differs from traditional methods in that it uses charged droplets to precisely regulate film homogeneity and density. This results in high-quality films with exceptional surface flatness and uniformity, as well as fewer flaws and reduced material wastage.

The correlation between the growing technique of ZnO semiconductor thin films and the microstructural properties (MSP) is easily discernible. Furthermore, future research on the steps involved in thin-film semiconductor development could make use of the ESD approach. The results of this study suggest that using ESD to deposit the ZnO film has benefits in the fabrication of stacked thin film devices. This is the first step toward producing inexpensive, simple, and transparent-to-visible-light ESD devices using semiconductor oxide-based materials.

ACKONWLEDGEMENTS

This study has been sponsored by MEXT for the scholarship of supporting international student (Fysol Ibna Abbas), JSPS KAKENHI (Grant number: 21K04696), and the Renewable Energy Science and Technology Research Division of the Tokyo University of Science.

REFERENCES

1. Tang, Z. K., Wong, G. K. L., Yu, P., Kawasaki, M., Ohtomo, A., Koinuma, H., & Segawa. Y. (1998). Room-Temperature Ultraviolet Laser Emission from Self-Assembled ZnO Microcrystallite Thin Films. *Appl. Phys. Lett., 72* (25), 3270–3272. https://doi.org/10.1063/1.121620
2. Kind, H., Yan, H., Law, M., Messer, B., & Yang, P. (2002). Nanowire Ultraviolet Photodetectors and Optical Switches. *AdV. Mater., 14* (2), 158–160.
3. https://doi.org/10.1002/1521-4095(20020116)14:2<158::AID-ADMA158>3.0.CO;2-W
4. Yin, M., Gu, Y., Kuskovsky, I. L., Andelman, T., Zhu, Y., Neumark, G. F., & O'Brien, S. (2004). Zinc Oxide Quantum Rods. *J. Am. Chem. Soc., 126* (20), 6206–6207. https://doi.org/10.1021/ja031696+
5. Wu, D., Huang, L. D., Wang, Q. J., Zhao, X. N., Li, A. D., Chen, Y. F., & Ming, N. (2005). Bell-Mouthed Single-Crystalline Tubular ZnO Prepared by a Soft Solution Method. *Mater. Chem. Phys., 96* (1), 51–54. https://doi.org/10.1016/j.matchemphys.2005.04.059
6. Fan, H. J., Scholz, R., Kolb, F. M., Zacharias, M., & Gosele, U. (2004). Growth Mechanism and Characterization of Zinc Oxide Microcages. *Solid State Commun., 130* (8), 517–521. https://doi.org/10.1016/j.ssc.2004.03.014
7. Zhang, W. H., Shi, J. L., Wang, L. Z., & Yan, D. S. (2000). Preparation and Characterization of ZnO Clusters inside Mesoporous Silica. *Chem. Mater., 12* (5), 1408–1413. https://doi.org/10.1021/cm990740a
8. Gao, P. X., Ding, Y., & Wang, Z. L. (2003). Crystallographic Orientation-Aligned ZnO Nanorods Grown by a Tin Catalyst. *Nano Letters*, *3* (9), 1315–1320. https://doi.org/10.1021/nl034548q
9. Ada, K., Goekgoez, M., Oenal, M., & Sankaya, Y. (2008). Preparation and Characterization of a ZnO Powder with the Hexagonal Plate Particles. *Powder Technology*, *181*, 285–291. https://doi.org/10.1016/j.powtec.2007.05.015
10. Thomas, D. G. (1960). The Exciton Spectrum of Zinc Oxide. *J. Phys. Che. Solids*, *15* (1–2), 86–96. https://doi.org/10.1016/0022-3697(60)90104-9
11. Nakai, H., Sugiyama, M., & Chichibu, S. F. (2017). Ultraviolet Light-Absorbing and Emitting Diodes Consisting of a p-Type Transparent-Semiconducting NiO Film Deposited on an n-Type GaN Homoepitaxial Layer. *Appl. Phys. Letter, 110* (18), 181102(1–5). https://doi.org/10.1063/1.4982653
12. Dutta, T., Gupta, P., Gupta, J., & Narayan, J. (2010). Effect of Li Doping in NiO Thin Films on its Transparent and Conducting Properties and its Application in Heteroepitaxial p-n Junctions. *J. Appl. Phys.*, *108* (8), 083715 (1–7). https://doi.org/10.1063/1.3499276
13. Xia, X. H., Tu, J. P., Zhang, J., Wang, X. L., Zhang, W. K., & Huang, H. (2008). Morphology Effect on the Electrochromic and Electrochemical Performances of NiO Thin Films, *Elec. Acta, 53* (18), 5721–5724. https://doi.org/10.1016/j.electacta.2008.03.047
14. Cloupeau, M., & Prunet-Foch, B. (1989). Electrostatic Spraying of Liquids in Cone–Jet Mode. *J. Electrostat.*, *22* (2), 135–159. https://doi.org/10.1016/0304-3886(89)90081-8
15. Jung, J. H., Oh, H., & Kim, S. S. (2010). Numerical Simulation of the Deposition Pattern in Multiple Electrohydrodynamic Spraying. *Powder Technol., 198* (3), 439–444. https://doi.org/10.1016/j.powtec.2009.12.006
16. Tomono, K., & Sugiyama, M. (2024). Investigating Electrical Properties and Crystal Growth in NiO Thin Films by Spray Pyrolysis and Electrostatic Spray Deposition. *J. J. A. Physics, 63*, 025504(1–5). https://doi.org/10.35848/1347-4065/ad1f09

17. Abbas, F. I., & Sugiyama, M. (2024). A Comparative Study of Property Measurement for ZnO-Thin Film Growth Processes Using Hydrocloric Acid (HCl) and Water (H2O) Solution-Dependent on Novel Electrostatic Spray Deposition (ESD). *Lat. Jour. Phy. Tec. Sciences, 62* (2), 30–41.
18. Kumar, V., Sharma, H., Singh, S. K., Kumar, S., & Vij, A. (2019). Enhanced Near-Band Edge Emission in Pulsed Laser Deposited ZnO/c-Sapphire Nanocrystalline Thin Films. *App. Physics A*, *125,* 212 (1–7). https://doi.org/10.1007/s00339-019-2485-0
19. Singh, S. K., & Singhal, R. (2018). Thermal-Induced SPR Tuning of Ag-ZnO Nanocomposite Thin Film for Plasmonic Applications. *Appl. Surf. Sci., 439*, 919–926. https://doi.org/10.1016/j.apsusc.2018.01.112
20. Gondal, M. A., Drmosh, Q. A., Yamani, Z. H., & Saleh, T. A. (2009). Synthesis of ZnO2 Nanoparticles by Laser Ablation in Liquid and their Annealing Transformation into ZnO Nanoparticles. *Appl. Surf. Science*, *256* (1), 298–304. https://doi.org/10.1016/j.apsusc.2009.08.019
21. Pal, U., Serrano, J. G., Santiago, P., Xiong, G., Ucer, K. B., & Williams, R. T. (2006). Synthesis and Optical Properties of ZnO Nanostructures with Different Morphologies. *Optical Materials*, *29* (1), 65– 69. https://doi.org/10.1016/j.optmat.2006.03.015
22. Modwi, A., Abbo, M. A., Hassan, E. A., Taha, K. K., Khezami, L., & Houas, A. (2016). Influence of Annealing Temperature on the Properties of ZnO Synthesized via 2.3. Dihydroxysuccinic Acid Using Flash Sol-Gel Method. *J. Ovo. Research, 12* (2), 59–66.
23. Thool, G. S., Singh, A. K., Singh, R. S., Gupta, A., & Susan, M. A. B. H. (2014). Facile Synthesis of Flat Crystal ZnO Thin Films by Solution Growth Method: A Micro-Structural Investigation. *Jou. Sau. Chem. Society, 18*, 712–721. https://doi.org/10.1016/j.apsusc.2018.01.112

sciendo

LATVIAN JOURNAL OF PHYSICS
AND TECHNICAL SCIENCES
2025, N 3

DOI: 10.2478/lpts-2025-0024

INVESTIGATING THE FEASIBILITY OF INTEGRATING VEGETATION INTO SOLAR CHIMNEY POWER PLANTS IN THE TAMANRASSET REGION

S. Ali[1,2]*, B. Djaouida[1]

[1] Faculty of Science and Technology,
University of Tamanrasset,
Tamanrasset, ALGERIA
[2] Materials and Energy Research Laboratory,
University of Tamanrasset,
Tamanrasset, ALGERIA
*e-mail: sellami2003@hotmail.com

The Solar Chimney Power Plant (SCPP) utilises a two-step procedure to transform solar energy into electricity. First, it uses a solar collector to turn sunlight into thermal energy. Then, this thermal energy is transformed into kinetic energy as it raises a chimney and finally into electrical energy via a wind turbine and generator. A numerical simulation of a prototype in Manzanares, Spain, was conducted using a 2D axi-symmetric model and computational fluid dynamics with an RNG k-turbulence model. The simulation also involved solving the radiative transfer equation with a two-band discrete ordinate radiation model. This study aims to evaluate the effect of vegetation beneath the collector roof on a solar chimney power plant's performance. Our research compared various designs of these power plants, both with and without vegetation. Three configurations were examined in this study: a standard power plant, a power plant with a secondary collector roof, and a power plant with both secondary and tertiary collector roofs. According to our findings, the system with secondary and tertiary collector roofs demonstrated the highest electricity generation capacity, yielding an annual output ranging from 34 to 80 kW. The findings indicate that adding vegetation into a solar chimney power plant is feasible but will most likely reduce the plant's energy generation.

Keywords: *Electrical generator, numerical simulation, solar chimney, solar energy, vegetation.*

1. INTRODUCTION

The growing need for energy and dependence on non-renewable fossil fuels has caused environmental concerns. Solar chimney power plants offer a promising solution as a clean energy source. The described system is a renewable energy technology that harnesses solar radiation to increase the internal energy of air, afterwards converting it into electrical energy through the utilisation of wind turbines. The concept of utilising air energy as a means of power generation was initially introduced by Spanish Colonel Cabanyes during the early 1900s [1]. In the 1980s, researchers put Cabanyes' idea to the test by building a prototype of a Solar Upwind Power Plant, also known as a Solar Chimney Energy System or Solar Tower [2]. Solar Upwind Power Plants are a clean and eco-friendly method of capturing solar energy to generate electricity [3]. The Solar Chimney Power Plant system represents a form of renewable energy generation that effectively converts solar energy into thermal energy, followed by the conversion of thermal energy into kinetic energy, and ultimately into electrical energy [4]. The Solar Chimney Power Plant was initially introduced by Professor Jörg Schlaich during the latter part of the 1970s. Subsequently, a prototype of this design was subjected to testing in Manzanares, Spain, during the early 1980s [5].

In recent times, several studies have undertaken an analysis of Solar Collector Performance Parameters (SCPP) utilising widely employed commercial Computational Fluid Dynamics (CFD) software packages, including FLUENT and TRNSYS [6]–[12]. A study by Ming et al. [13] analysed the impact of crosswind velocity on SCPP performance. Cao et al. [10] evaluated SCPP performance through a design and simulation analysis using TRNSYS. In their 2007 simulation, Huang et al. [14] employed a Spanish prototype plant and utilised the Boussinesq model and DO to simulate natural convection and radiation, respectively. It was discovered that augmented solar radiation resulted in elevated temperature disparities and differential pressure at the intake and outflow of the collector, as well as at the transition section between the collection and the chimney.

In their study, Gholamalizadeh and Kim (2016) employed a three-dimensional computational fluid dynamics (CFD) analysis together with a two-band radiation model to replicate the greenhouse effect and heat transport within the system [9]. Their research underscores the importance of greenhouse effect simulations in assessing the performance of solar combined power and cooling (SCPP) systems. The study conducted by Guo et al. [15] involved the integration of radiation, solar load, and an actual turbine in a simulation to investigate various power-regulating strategies for solar chimney turbines. The researchers compared the outcomes obtained from a fan model with those obtained from an actual turbine.

The study conducted by Nasirivatan et al. (2015) examined the influence of Corona wind on the performance of solar chimneys [16]. In 2016, Ghalamchi et al. conducted an optimisation study on a pilot solar chimney configuration, con-

sisting of a 3-meter height and a 3-meter collector [17]. Liu and Li (2020, 2021) conducted an assessment on the thermal efficiency of a solar chimney system incorporates a phase change material (PCM) [18], [19].

The study conducted by Attig et al. (2015) involved the comparison of a three-dimensional computational fluid dynamics (CFD) model of a solar chimney power plant (SCPP) with the Manzanares plant prototype [20]. The objective of the study was to investigate the operational aspects of SCPP in Tunisia. In their study, Akhtar and Rao conducted an analysis on the economic efficiency of a 200 MW supercritical coal-fired power plant (SCPP) located in Rajasthan, India [21].

The objective of this study is to investigate the feasibility of the incorporation of vegetation under the collector roof of a solar chimney.

2. PHYSICAL MODEL

A physical model of SCPP is established to examine the influence of buoyancy on flow and heat transfer. The design is based on the Manzanares power plant with a 194.6-meter-tall chimney (Hch) and 10.16-meter-wide diameter (rch). The collector has a radius (Rcol) of 122 meters and an average height (Hcol) of 1.85 meters, and the turbine is positioned 9 meters above the ground. The collector height increases to a maximum of 6 meters near the chimney base, which results in the airflow being directed upwards before reaching the turbine. The ground, serving as the energy storage medium, is assumed to be five meters thick. This design is illustrated in Fig. 1.

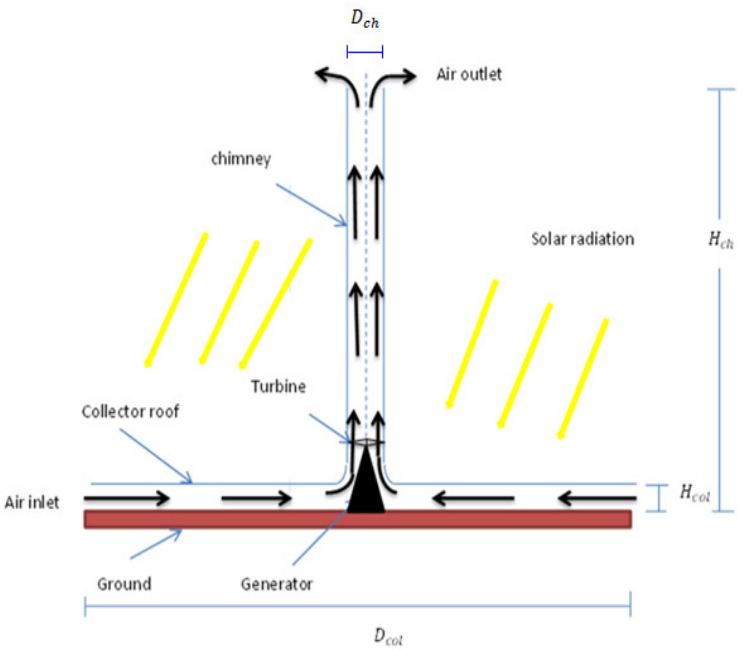

Fig. 1. A diagram of the solar chimney power plant system.

3. ELECTRICITY PRODUCTION

3.1. The Collector

The formula for the heat gained by air in the collector is as follows:

$$Q = \eta_{col.} A_{col.} G\,, \tag{1}$$

where $A_{col.}, G$ *and* η_{col} are the solar collector area ($A_{coll} = \pi R_{col}^{2}$), the solar radiation and the solar collector efficiency, respectively. Q represents also the generated heat due to the effect of the greenhouse in the collector and can be expressed as follows:

$$Q = C_{p.} m \Delta T\,, \tag{2}$$

where $m = \rho_{air.} V_{ch} A_{ch}$. (3)

Then, the efficiency of the solar collector is described as follows:

$$\eta_{col.} = \frac{\rho_{air} V_{ch} A_{ch} C_p \Delta T}{A_{col} G}\,. \tag{4}$$

In this context, m represents the mass flow, A_{ch} denotes the surface area, and V_{ch} signifies the velocity at the entrance to the chimney.

3.2. The Chimney

As stated in [24], the chimney's efficiency is defined as follows:

$$\eta_{ch} = \frac{g.H_{ch}}{C_p T_a}, \tag{5}$$

where H_{ch} represents the height of the chimney, T_a stands for the ambient air temperature, and the flow power P_{tot} is expressed as follows:

$$P_{tot} = \eta_{ch}\, \mathrm{Q} = \frac{g H_{ch}}{T_a} \rho_{col} V_{ch} \Delta T A_{ch}\,. \tag{6}$$

The pressure difference, ΔP_{tot}, created between the base of the chimney and its surroundings, is determined by:

$$\Delta P_{tot} = \rho_{col} g H_{ch} \frac{\Delta T}{T_a}. \tag{7}$$

3.3. The Turbine

Turbines are installed at the bottom of chimneys to transform the kinetic energy of air flow into mechanical energy through rotation. According to [22], the maximum amount of mechanical power that can be generated by the turbine is as follows:

$$P_m = \frac{2}{3} \eta_{col} \eta_{ch} A_{col} \mathrm{G}. \tag{8}$$

The amount of electrical energy generated by the central solar chimney is determined by:

$$P_e = \frac{2}{3} \eta_{col} \eta_{turb} \frac{g}{C_p T_a} H_{ch} A_{col} \mathrm{G}. \tag{9}$$

4. INCORPORATION OF VEGETATION UNDER THE COLLECTOR ROOF OF SOLAR CHIMNEY POWER PLANTS

With vegetation added to the collector, the existing physical model (shown in Fig. 1) must be modified. As shown in Fig. 2, the collector is divided into two parts: one for vegetation and one for the ground. The vegetation is assumed to be planted all around the collector's circumference (360°), extending inward from the collector's perimeter to a determined radius (Rveg). This allows vegetation to be situated under the collector roof without suffering from the high temperatures near the chimney.

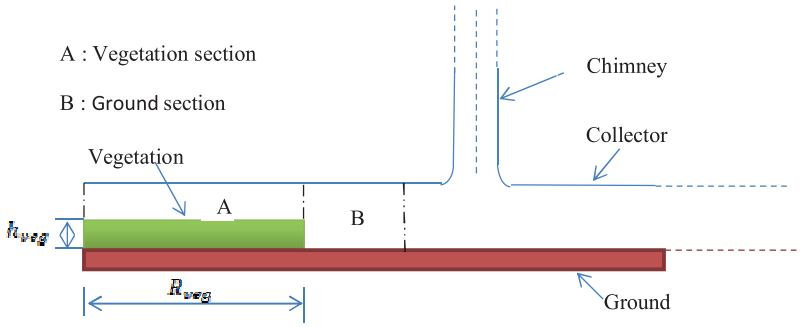

Fig. 2. The addition of vegetation under the collector roof creates two sections in the collector: the vegetation section and the ground section.

5. APPROACH FOR THE POROUS MEDIUM

Since the 1980s, the greenhouse climate uniformity assumption has been widely adopted for modelling heat and mass transfer. This assumption presumes that the greenhouse environment is perfectly uniform, with a single temperature and air speed assumed to be consistent near the walls and at ground level, or within the vegetation, which is typically modelled as a large, uniform-temperature "big leaf" [23].

Modelling the flow of heat, vapour, and momentum in a greenhouse is essential for understanding and predicting the crop's response to external physical factors. The complexity of defining and designing a 3D domain makes it challenging, but using vegetation as a porous medium is proposed as a solution [24], [25].

A porous material is composed of a solid matrix containing interconnected pores through which fluid can flow. The presence of the solid matrix significantly affects the transfer of properties such as momentum balance, as the friction on the matrix affects it. Darcy's law [26] is a simple model that explains the relationship between the pressure gradient and the velocity vector in a defined space.

$$gradP = -\frac{\mu}{K}u\,. \tag{10}$$

The intrinsic permeability of the porous medium, which only depends on its geometry, is represented by the coefficient K. This law does not include the inertia term and represents the momentum equation.

The validity of Darcy's law is defined by the modified Reynolds number [26].

$$\mathrm{Re}_P = \frac{U}{\nu}\sqrt{K}\,, \tag{11}$$

where U – wind speed and ν – the air's kinematic viscosity.

Many experiments have verified Darcy's law, but it only applies when the fluid flow is slow and the Reynolds number (Re_P) is below one based on typical pore size. This means that friction resistance is more significant than resistance due to changes in flow direction. Furthermore, there is a transition domain ($1 \prec \mathrm{Re}_P \prec 10$). When this occurs $\mathrm{Re}_P \succ 10$, the pressure gradient is influenced by both the flow speed and its square. This is true even if the flow within the pores does not turn turbulent, as the resistance to flow caused by friction is similar to the resistance due to the shape of the pores (which causes changes in flow direction). The Darcy equation (10) must then be revised by incorporating a factor that depends on the velocity squared; this results in the Darcy-Forchheimer equation [26].

$$gradP = -\frac{\mu}{K}u - \frac{c_F}{\sqrt{K}}\rho u U\,, \tag{12}$$

where ρ is the fluid's density and c_F is a dimensionless factor that depends on the characteristics of the porous medium, referred to as the inertial factor or nonlinear pressure drop coefficient. Initially considered c_F was a universal constant of the order of 0.55; however, it was later found to vary between 0.1 and 0.61, depending on the porous medium's composition [26].

In greenhouse conditions where the crop's permeability is substantial (the order of magnitude of dynamic viscosity μ is 10^{-5} for air), the pressure gradient is only influenced by the quadratic term as the viscous term is negligible [26].

$$gradP \approx -\frac{c_F}{\sqrt{K}}\rho u U\,, \tag{13}$$

where u – the velocity vector; U – the wind speed.

6. FLOW INTERACTION WITH VEGETATION COVER

The interaction between a plant canopy and air flow causes a decrease in momentum and increased absorption of solar energy by the leaves. This includes heat, water vapour release through transpiration, and exchanges in photosynthesis. These factors must be taken into account when using computational fluid dynamics (CFDs). The loss of momentum is due to the impact of the pressure gradient (*gradP*), as represented by a commonly used formula in [26].

$$gradP = L_l C_v \rho u U\,, \tag{14}$$

where L_l is the leaf area, u is the air velocity, and C_v is the friction coefficient.

Studies [26], [27] combined this technology with a porous media approach. The inertial factor and permeability of the porous media are determined based on the plant's characteristics using the relationship.

$$\frac{C_F}{\sqrt{K}} = L_l C_v\,. \tag{15}$$

7. BOUNDARY CONDITIONS

Table 1 illustrates the physical model's boundary conditions. The roof of the collector is treated with a convection boundary condition, where the heat transfer coefficient from the collector roof to the environment is computed by Pretorius and Kröger [28]. The solar insolation that enters the computational domain through the semi-transparent collector cover is acquired from data sources [6], [29].

In a Solar Chimney Power Plant, a wind turbine that operates in stages of pressure is positioned at the base of the chimney. This design keeps the air velocity unchanged both before and after the turbine. To determine the pressure differential across the turbine during simulations, an iterative process was employed [9].

Table 1. Boundary Conditions

Place	Type	Value
Sides of the heat storage layer	Wall	Adiabatic
Bottom	Wall	T=330K
Cover of the collector	Wall (semi-transparent)	Mixed, h=9.5$W.m^{-2}.K^{-1}$, T_a = *Tambiante* solar irradiation
Surface of the chimney and junction	Wall	Adiabatic
Axe	Axis	Symmetry
Collector inlet	Pressure inlet	$P_{gage} = 0Pa$
Chimney outlet	Pressure outlet	$P_{gage} = 0Pa$
Pressure drop across the turbine	Reverse fan	Calculated by the iterative approach

8. BOUNDARY CONDITIONS AND PHYSICAL PROPERTIES OF THE SYSTEM

The main settings of the CFD simulation are outlined in Table 2a, and the construction materials and their physical properties are presented in Table 2b. Furthermore, a portion of the ground surface area is covered with vegetation under the collector roof (as seen in Fig. 2) with dimensions specified in Table 3.

Table 2a. Boundary Conditions

Classification	Setting	Classification	Setting
Solver	-Pressure-based coupled algorithm. -2D axisymmetric simulation. -Steady state (second-order upwind discretization).	Viscous model	- RNG $k-\varepsilon$ model. - Full buoyancy effects.
Energy equation	-Activated.	Radiation model	- DO (discrete ordinates). - Theta divisions: 3. - Phi divisions: 5. - Theta pixels: 3. - Phi pixels: 5.

Table 2b. Physical Properties of Materials [28]

Physical property (unit)	Glass (collector roof)		Ground (soil)	Chimney (concrete)
Wavelength band	Visible (0.1 – 3) μm	Infrared (3 – 100) μm	-	-
Absorption coefficient	0.04	0.95	0.90	0.60
Transmission coefficient	0.92	0.05	0	0
Absorption coefficient (m^{-1})	30	104	-	-
Emissivity	0.9		0.9	0.71
Refractive index	1.526		-	-
Extinction coefficient (m^{-1})	4		-	-
Density (kg/m^3)	2700		2160	2100
Specific heat ($J/Kg.K$)	840		710	880
Thermal Conductivity ($W/m.K$)	0.78		1.83	1.40
Thickness (m)	0.004		-	-
Surface roughness (m)	0		0.05	0.002

Table 3. Physical Properties of Vegetation [30]–[34]

Physical properties of vegetation	
Density (kg/m^3)	800
Specific heat capacity ($J/Kg.K$)	3224.7
Thermal conductivity ($W/m.K$)	0.213
Emissivity	0.98
Absorptivity	0.77
Surface roughness (m)	0.1
The height of vegetation hveg (m)	0.3
Radial distance from perimeter (m)	106.5

9. PARAMETERS EMPLOYED IN THE POROUS MEDIA MODEL

The vegetation cover is modelled as a porous medium using the Fluent 17.1 program for solving fluid dynamics equations, which combines the traditional porous medium approach with the discretization of Darcy and Forchheimer equations. The vegetation cover in this study consists of a row of young cowpea plants surrounding the collector in a 360° orientation, extending to a specified radius, Rveg, with a height of 0.3 m. The intrinsic permeability of the porous medium is defined as K = 0.884 and the non-linear pressure drop coefficient as = 1 [26].

10. SIMULATION AND RESULTS

Four numerical simulations are conducted: (1) solar chimney power plant without radiation and vegetation, (2) solar chimney power plant with radiation and no vegetation, (3) solar chimney power plant without radiation but with vegetation, and

(4) solar chimney power plant with radiation and vegetation. These simulations are based on the previously described plant specifications, the properties of the vegetation, and an assumed maximum temperature of 39 °C at which the vegetation can operate without disrupting photosynthesis (lower than the values determined in [34]). The study examines the inclusion of vegetation under the collector roof, extending from the collector perimeter to radii of Rveg = 106.5m.

The temperature and velocity profiles of the fluid in the collector with and without vegetation are shown in Figs. 3 and 4, respectively, for a specific solar radiation level (Q = 1000 W/m^2). The temperature and velocity of the fluid increase as the radius decreases and approaches the base of the chimney. Figure 3 displays the air velocity profiles through the collector, and it can be seen that in the vegetation zone, the speed decreases slightly before gradually increasing closer to the base of the chimney. The highest temperature and velocity of the fluid are recorded in the solar chimney power plant without vegetation and with radiation, as seen in Figs. 3 and 4. This indicates that both the presence of vegetation and radiation play a role in the performance of the solar chimney power plant.

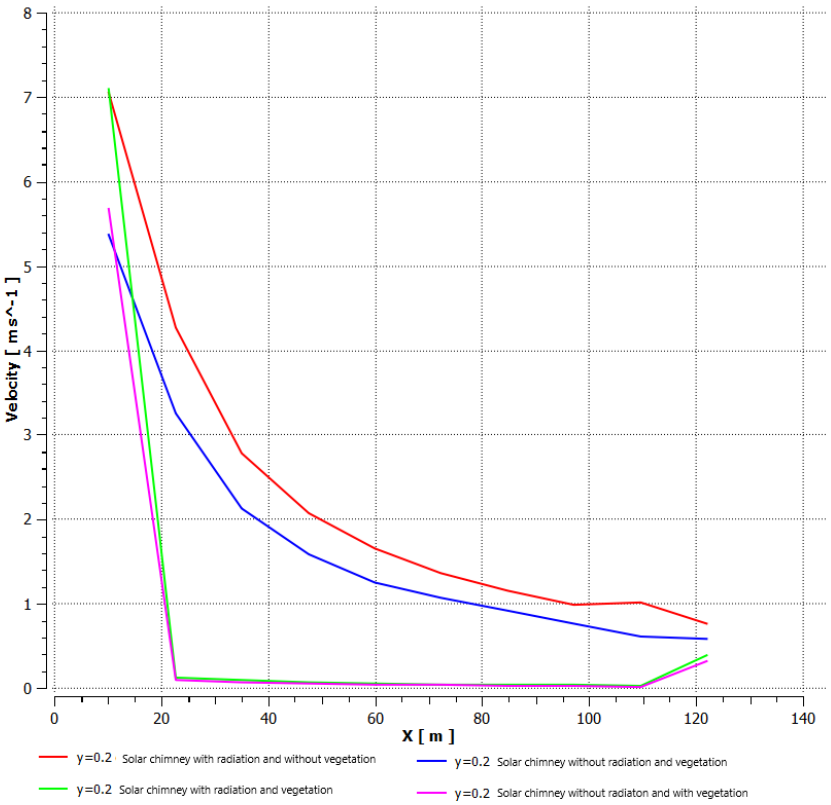

Fig. 3. Velocity profile of the different SCPP systems in the collector at (R_{veg} = 106.5 m), Y = 0.2 and $T_{sol-air}$ = 324K and solar insolation of 1000 W / m^2.

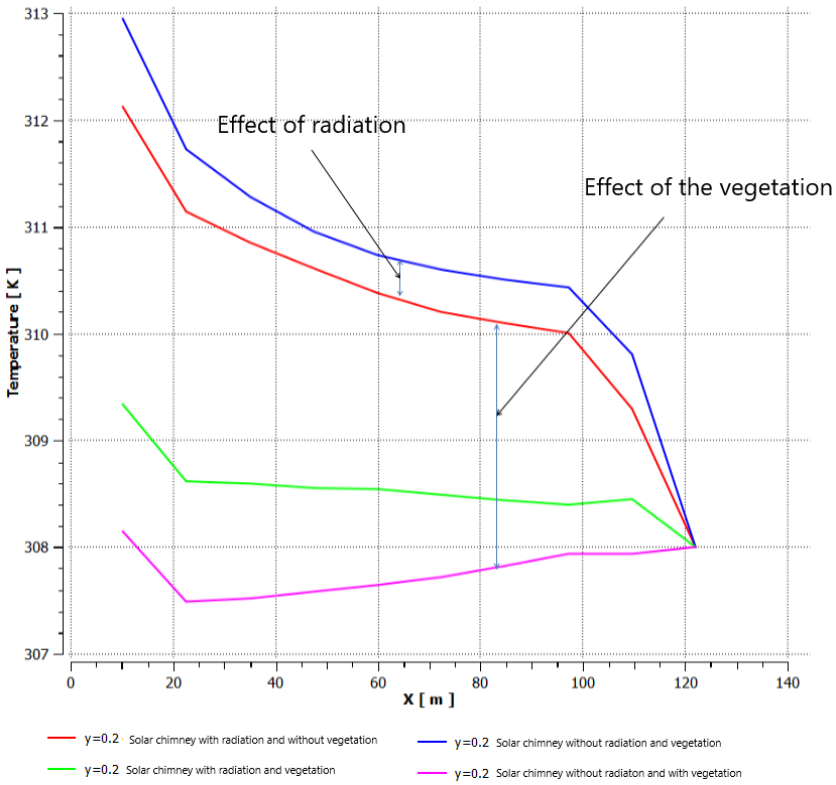

Fig. 4. Temperature profile of the different SCPP systems in the collector at (R_{veg} = 106.5 m), Y = 0.2 and $T_{sol-air}$ = 324K and solar insolation of 1000 W / m^2.

The simulations of the reference plant, secondary collector roof, and secondary and tertiary collector roof systems have been carried out as outlined in [11]. The results, shown in Table 4, demonstrate that the secondary and tertiary collector roof systems generate the most electricity compared to the other systems. However, incorporating vegetation into a solar chimney power plant reduces the electricity production as compared to solar chimney systems without vegetation. Adding vegetation may be a possibility, but it leads to a significant decrease in the power output of the plant.

Table 4. The Comparison of Power Output at a Solar Irradiation of 1000 W/m2 and a Ground Temperature of 324 K

Systems	Power output (Kw)	
	With vegetation	Without vegetation
Reference plant	31.2	50.01
Plant with secondary collector roof	39.6	59.7
Plant with secondary and tertiary collector roof	60.04	80.2

11. A CASE STUDY

The functioning of solar systems is strongly tied to the amount of solar radiation received. Our initial focus was on this key factor. The German Special Agency states that Algeria has a higher solar potential compared to other countries in the Mediterranean region [35].

This study focuses on Tamanrasset, a city in southern Algeria with an ideal location for utilising solar energy and its associated technologies. The city's geographical coordinates are listed in Table 5. We obtained the average monthly daily solar radiation data, measured in MJ/m2/day, from various national and international databases, including the Solar Atlas of Algeria [29], [6], the Photovoltaic Geographical Information System, and Metronome, which is a commercial data source.

The Tamanrasset region is in the southern part of Algeria and boasts a dry Saharan climate with abundant sunshine and flat, unused areas, making it an ideal location for solar energy utilisation and the adoption of SCPP technology. This will provide electric power to remote villages in southern Algeria. Additionally, harnessing thermal energy in the collector zone through greenhouse farming practices will significantly reduce the cost of energy production.

Table 5. Geographical Coordinates of Tamanrasset Region

Sites	Lat. °N	Long. °E	Alt. (m)	Climate
Tamanrasset	22.8	5.5	1381	Arid

Figure 5 displays the monthly variations in solar radiation in the Tamanrasset region. It can be seen that Tamanrasset experiences high levels of solar radiation (28.8 MJ/m2/day), and the highest levels occur in June.

Figure 6 illustrates the variations in the average ambient temperature of the Tamanrasset region throughout the year. The average ambient temperature in Tamanrasset can reach 29 °C.

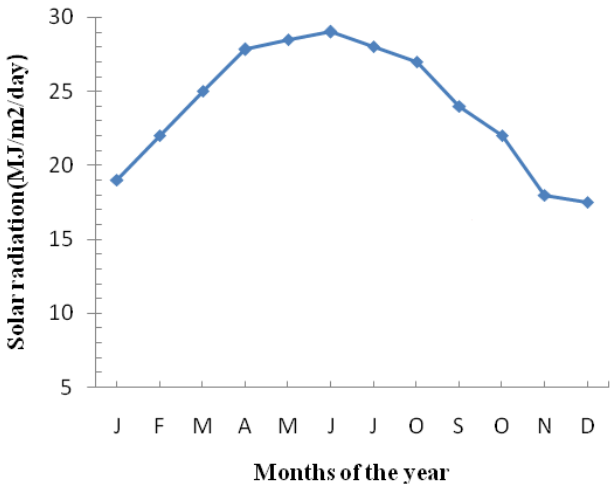

Fig. 5. Monthly solar radiation in the Tamanrasset region.

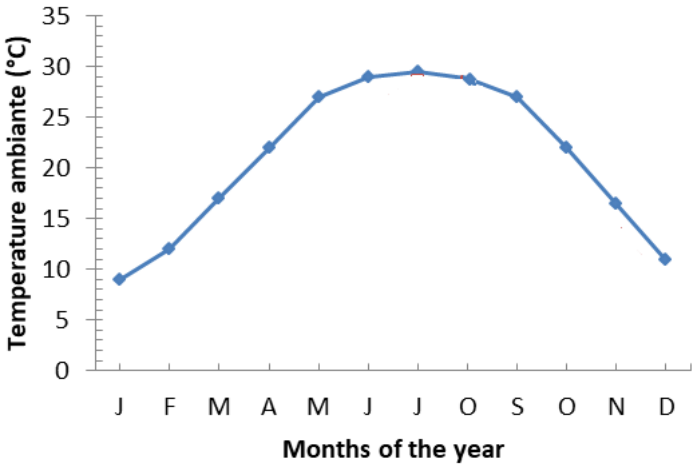

Fig. 6. Monthly ambient temperature in the Tamanrasset region.

Three numerical simulations were conducted based on the plant specifications, vegetation properties, and maximum temperature for vegetation survival, as described in [11]. The simulations involved the reference plant, a secondary collector roof, and systems with secondary and tertiary collector roofs. This section covers the integration of vegetation under the collector roof, from the collector's edge to the Rveg rays of the collector.

By comparing the three systems at Tamanrasset, the reference plant, secondary collector roof, and secondary and tertiary collector roof systems (detailed in [11]), we found that the secondary and tertiary collector roof systems generated the most electricity, as shown in Figs. 7– 9. They display the monthly electricity generated by SCPP located in the Tamanrasset region. The figures indicate that the reference solar chimney with vegetation (without a secondary collector roof) produces less electricity than the reference solar chimney without vegetation.

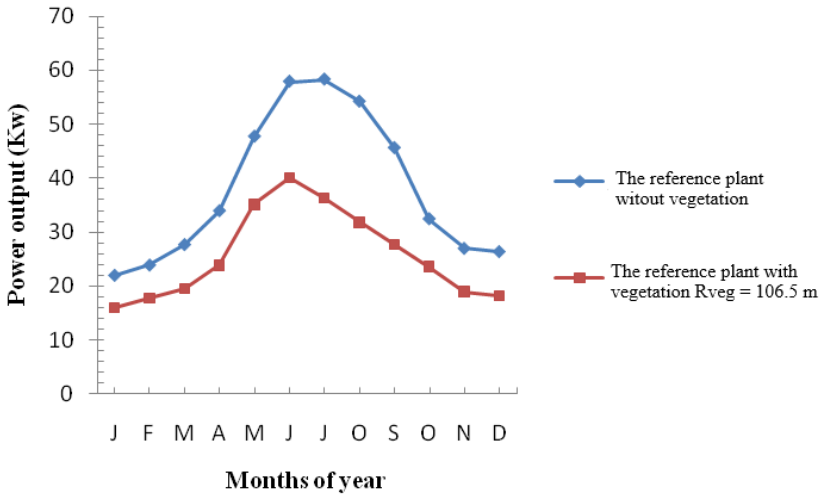

Fig. 7. Monthly average productivity of the power of the solar chimney at Tamanrasset.

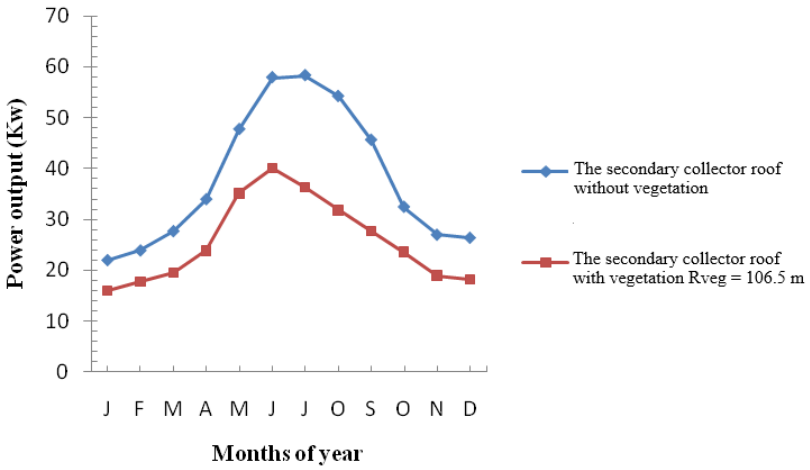

Fig. 8. Monthly average productivity of the power of the solar chimney at Tamanrasset.

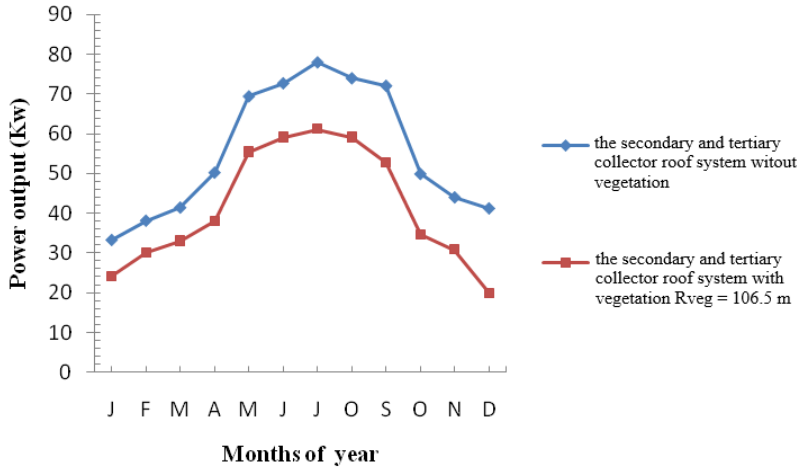

Fig. 9. Monthly average productivity of the power of the solar chimney at Tamanrasset.

12. CONCLUSIONS

This paper presents a numerical study of solar chimney power plants with and without the presence of vegetation. The main aim is to evaluate the impact of vegetation on the plant's power output when placed under the collector roof. We analysed the performance of different solar chimney power plant configurations with and without vegetation under the collectors.

We included the reference plant, a secondary collector roof, and systems with secondary and tertiary collector roofs. According to the findings, the secondary and tertiary collector roof system had the greatest electricity production, generating an annual output of 34 to 80 kW. The results indicate that incorporating vegetation into a solar chimney power plant may be possible, but it will result in significant reductions in the plant's power output.

ACKNOWLEDGEMENTS

This research has been supported by the Ministry of Higher Education and Scientific Research, Algeria (Grant Reference Number A10N01UN110120230001). We are very grateful to our Research Laboratory for their great help in making part of this work to be done.

REFERENCES

1. Dhahri, A., & Omri, A. (2013). A Review of Solar Chimney Power Generation Technology. *International Journal of Engineering and Advanced Technology, 2* (3), 1–17.
2. Heisler, E. M. (2014). *Exploring Alternative Designs for Solar Chimneys Using Computational Fluid Dynamics*. Thesis.
3. Humphries, M. (2001). *Solar Tower in Arizona to Power 150,000 Homes for 80 years*. GEEK. [Online]. Available: http://www.geek.com/geek-pick/solar-tower-in-arizona-to-power-150000-homes-for-80-years-1406459/
4. Tahar, T., & Djezzar, M. (2021). Numerical Simulation of Natural Convection in a Solar Chimney. *International Journal of Renewable Energy Research, 2* (4), 712–717.
5. Haaf, W., Friedrich, K., Mayer, G., & Schlaich, J. (1983). Solar Chimneys. *Int J Sol Energy*, *2*, 3–20.
6. Rabehi, R., Chaker, A., Aouachria, Z., & Tingzhen, M. (2017). CFD Analysis on the Performance of a Solar Chimney Power Plant System: Case Studying Algeria. *International Journal of Green Energy*, *14* (12), 971–982.
7. Hu, S., Leung, D. Y., Chen, M. Z., & Chan, J. C. (2016). Effect of Guide Wall on the Potential of a Solar Chimney Power Plant. *Renewable Energy, 96*, 209–219.
8. Hafizh, H. (2015). *Theoretical Analysis and Experimental Optimization of Solar Updraft Power Generator.* PhD Thesis.
9. Gholamalizadeh, E., & Kim, M.-H. (2014). Three-Dimensional CFD Analysis for Simulating the Greenhouse Effect in Solar Chimney Power Plants Using a Two-Band Radiation Model. *Renewable Energy*, *63*, 498–506.
10. Cao, F., Li, H., Zhao, L., Bao, T., & Guo, L. (2013). Design and Simulation of the Solar Chimney Power Plants with TRNSYS. *Solar Energy, 98,* 23–33.
11. Djaouida, B., Aouachria, Z., Benmachiche, A. H., & Ali, S. (2020). Controlling Power Output of Solar Chimney Power Plant according to Demand. *International Journal of Ambient Energy, 41* (13), 1467–1481.
12. Ali, S., Djaouida, B., Benmachiche, A. H., & Aouachria, Z. (2021). Performance Analysis of a Solar Chimney Power Plant System in Two Algeria Regions. *International Journal of Ambient Energy, 43* (6), 1–26.
13. Ming, T., Wang, X., De Richter, R. K., Liu, W., Wu, T., & Pan, Y. (2012). Numerical Analysis on the Influence of Ambient Crosswind on the Performance of Solar Updraft Power Plant System. *Renewable and Sustainable Energy Reviews, 16* (8), 5567–5583.
14. Huang, H., Zhang, H., Huang, Y., & Lu, F. (2007). Simulation Calculation on Solar Chimney Power Plant System. *Challenges of Power Engineering and Environment*: Springer, 1158–1161.
15. Guo, P., Li, J., Wang, Y., & Wang, Y. (2015). Numerical Study on the Performance of a Solar Chimney Power Plant. *Energy Conversion and Management, 105,* 197–205.

16. Nasirivatan, S., Kasaeian, A., Ghalamchi, M., & Ghalamchi, M. (2015). Performance Optimization of Solar Chimney Power Plant Using Electric/Corona Wind. *Journal of Electrostatics, 78,* 22–30.
17. Ghalamchi, M., Kasaeian, A., Ghalamchi, M., & Mirzahosseini, A. H. (2016). An Experimental Study on the Thermal Performance of a Solar Chimney with Different Dimensional Parameters. *Renewable Energy, 91,* 477–483.
18. Liu, S., & Li, Y. (2015). Heating Performance of a Solar Chimney Combined PCM: A Numerical Case Study. *Energy and Buildings, 99*, 117–130.
19. Li, Y., & Liu, S. (2014). Numerical Study on Thermal Behaviors of a Solar Chimney Incorporated with PCM. *Energy and Buildings, 80*, 406–414.
20. Attig, B.F., Guellouz, M.S., Sahraoui, M., & Kaddeche, S. (2015). A Numerical Study of Solar Chimney Power Plants in Tunisia. *Journal of Physics: Conference Series, 596* (1), 012006.
21. Akhtar, Z., & Rao, K.V.S. (2014). Study of economic viability of 200 MW solar chimney power plant in Rajasthan, India. *1st International Conference on Non-conventional Energy (ICONCE 2014),* (pp. 84–88). Kalyani, India.
22. Schlaich, J. (1995). *The Solar Chimney: Electricity from the Sun*. Germany: Geislingen.
23. Ould Khaoua, S.A. (2006). *Modélisation de l'aération naturelle et du microclimat des serres en verre de grande portée sous climat tempéré océanique.* Thèse de Doctorat, Ecole Doctorale d'Angers.
24. Boulard, T., Kittas, C., Roy, J. C., & Wang, S. (2002). Convective and Ventilation Transfers in Greenhouses, Part 2: Determination of the Distributed Greenhouse Climate. *Biosystèms Engineering, 83* (2), 129–147.
25. Majdoubi, H., Boulard, T., Fatnassi, H., & Bouirden, L. (2009). Airflow and Microclimate Patterns in a One-Hectare Canary Type Greenhouse: An Experimental and CFD Assisted Study. *Agricultural and Forest Meteorology, 149,* 6–7.
26. Haxaire, R. (1999). *Caractérisation et modélisation des écoulements d'air dans une serre*. Thèse de Doctorat, Université de Nice Sophia Antipolis.
27. Boulard, T., & Wang, S. (2002). Experimental and Numerical Studies on the Heterogeneity of Crop Transpiration in a Plastic Tunnel. *Computers and Electronics in Agriculture, 34*, 173–190.
28. Pretorius, J. P., & Kröger, D. G. (2006). Solar Chimney Power Plant Performance. *J Sol Energy Eng., 128,* 302–311.
29. Yaiche, M. R., Bouhanik, A., Bekkouche, S.M.A., Malek, A., & Benouaz, T. (2014). Revised Solar Maps of Algeria Based on Sunshine Duration. *Energy Conversion and Management, 82,* 114–23.
30. Mahapatra, A. K., Melton, S. L., & Isang, E. M. (2013). Effect of Moisture Content on Thermal Properties of Cowpea Flours. *Agric Eng Int: CIGR Journal, 15* (2).
31. Arku, A.Y., Aviara, N.A., & Ahamefula, S.C. (2012). Specific Heat of Selected Legumes and Cereal Grains Grown in North Eastern Nigeria. *Arid Zone Journal of Engineering, Technology and Environment, 8*, 105–114.
32. Appiah, F., Asibuo, J. Y., & Kumah, P. (2011). Physicochemical and Functional Properties of Bean Flours of Three Cowpea (Vigna unguiculata L. Walp) Varieties in Ghana. *African Journal of Food Science, 5* (2), 100–104.
33. Pretorius, J. P., & Kroger, D. G. (2008). Incorporating Vegetation under the Collector Roof of a Solar Chimney Power Plant. *R & D Journal, 24* (l), 3–11.
34. Wahid, A., Gelani, S., Ashraf, M., & Foolad, M. R. (2007). Heat Tolerance in Plants: An Overview. *Environmental and Experimental Botany, 61,* 199–223.
35. Mefti, A., Bouroubi, M. Y., & Mimouni, H. (2002). Evaluation du potentiel énergétique solaire. *Bulletin des Energies Renouvelables, 2*.